博士論文

Characteristics of Combustion and Lean Blowout Limit in a Double Swirl Burner for a Bio-Jet Fuel

(ダブルスワールバーナーにおけるバイオジェット燃料の
燃焼および希薄吹き消え限界特性)

Salman Patrick

(サルマン　パトリック)

東京大学大学院工学系研究科航空宇宙工学専攻

2020年6月

Characteristics of Combustion and Lean Blowout Limit in a Double Swirl Burner for a Bio-Jet Fuel

by

Patrick Salman

A dissertation submitted in partial fulfillment

of the requirements for the degree of Doctor of Philosophy

Department of Aeronautics and Astronautics

School of Engineering

The University of Tokyo

December

2020

Advisor: Professor Mitsuhiro Tsue

Für meinen Opa, weil Taten mehr aussagen als Worte.

(†Friedrich Kastner 25.Juni 1930 -19.November 2008)

Acknowledgment

Many people contributed to the creation of this work, which I would like to thank for. First of all, Professor Mitsuhiro Tsue, who often took the time for late-night discussions, in helping me forming the “story” of the thesis and giving valuable advice regarding the scientific background if I ended up at a dead end. Second, I would like to thank Professor Shinji Nakaya, for always pushing me to go beyond my limits. The frequent night runs together across Tokyo often cleared my mind and let me think about other approaches and ideas. I also would like to thank the committee members, Professor Toru Shimada, Professor Kojiro Suzuki, both from the University of Tokyo, and Dr. Keiichi Okai from JAXA, for giving me crucial input for this thesis. Strong acknowledgment also goes to the technical staff Mr. Masafumi Utsumi, Mr. Takeo Okunuki, and new technical staff Mr. Kengo Takizawa, who operated and maintained the high enthalpy windtunnel at Kashiwa campus of the University of Tokyo. I want to give a very big thanks to technical staff Mr. Yoichi Sugita, Department of Materials Engineering, the University of Tokyo, and his team for always finding the time to discuss design limitations and manufacturing the rather complicated combustion chamber for droplet measurements.

I also want to thank all members of JET-Team, who joined me on my journey of becoming a Ph.D.: Mr. Hiroaki Iida and Mr. Hiromu Ishikawa, who guided me in my first year; Mr. Gen Naka, Mr. Isami Sudo, and Mr. Issei Okamura, Bachelor and Master students, who supported me in conducting necessary experiments through the last three years.

Big thanks goes to my previous colleague and now Assistant Professor Shion Ando, who conducted the single droplet experiments as support for this thesis. I am also very thankful for Ph.D. candidate Fangsi Ren for always being helpful, regardless of the time or day of the week, and graduate Dr. Pravendra Kumar, for our countless talks, philosophizing about the world and education.

My deep gratitude goes towards my parents, Nabeel Salman and Hannelore Hauer, and my mother’s husband Alois Hauer, without their lifelong guidance and support I probably would not be able to have conducted a Ph.D. in the first place. From the bottom of my heart, I thank Surnaa Borjigin, my love; a girl, who truly taught me the meaning of focus, sacrifice, and hard work.

Content

Abstract

High demand for air transportation leads to future usage of new ultra-lean technologies paired with alternative fuels, which often show differences in properties compared to conventional jet fuels. These variations can lead to differences in combustion limits and combustion behavior, causing inappropriate influence onto stable operation of a jet engine, ending in malfunction or even damage of the system. Therefore, this research aims to explore experimentally differences in atomization and combustion behavior between conventional petroleum-derived Jet-A1 fuel and bioderived "Hydrotreated Esters and Fatty Acids" fuel (HEFA) in a non-premixed configuration of a dual swirl prefilm airblast injector, with the emphasis on physical properties.

Although, there exists several experimental data of different jet fuels used with different injector designs, Jet-A1 and Hydrotreated Ester and Fatty Acids were not compared in a dual swirl prefilm airblast injector yet, therefore it is one of this work's original contribution to knowledge. The used analyzing methods in this study are well known, but the combination of the gathered experimental data and their analysis of characteristic combustion time in a jet engine model combustor has not been conducted, yet. Additionally, difference in lean blowout of the two liquid fuels has not been addressed in a dual swirl prefilm airblast injector, especially not in regards to the fuels' characteristic combustion time, hence it is another original contribution to knowledge.

To analyze if the difference in physical properties between Jet-A1 and HEFA influence atomization, droplet size measurement via Interferometric Laser Imaging for Droplet Sizing (ILIDS) system were conducted. For the comparison of evaporation rate, both fuels were tested via single droplet experiments in a microgravity drop tower facility. The results showed no measurable difference in initial droplet size between Jet-A1 and HEFA in the used airblast injector. Evaporation rate showed significantly higher values for the tested biofuel of about 10%. Droplet size measurement at elevated heights from the injector during combustion showed slightly smaller droplets for HEFA compared to Jet-A1, confirming a better evaporation process.

Experiments at ambient condition and near jet engine condition with 630 K inlet temperature paired with 0.5 MPa pressure were conducted to test the stability limits of both fuels. HEFA showed in both

cases strong advantages over Jet-A1 in Lean Blowout Limit. Several airflow rates were tested at ambient condition and the differences between the two fuels correlated well with the difference in evaporation rate. Optical observation with a high-speed camera and a CH* chemiluminescence filter showed nearly constant lift-off height over the whole tested condition in the ambient case. Detections of droplets close to initial droplet size near the flame leading edge indicated strong non-premixing conditions, which stabilized the flame at the same position for all tested cases. Jet engine condition showed on the contrary a remarkable difference, with Jet-A1 staying nearly constant at a specific lift-off height and HEFA moving further downstream when changing the condition close to LBO. Reason was given to the stronger evaporation rate of HEFA, which transformed the flame from non-premixed to premixed flame, lifting further off, due to possible lower laminar flame speed of the global condition, where the Jet-A1 flame was still stabilized by droplets like in the ambient condition cases. Pressure signal analysis of near jet condition experiments revealed a periodic fluctuation of both fuels near LBO at a frequency of approximately 120 Hz, which was identified as Helmholtz mode. Simultaneous observation of spray via Mie Scattering showed HEFA with a substantial longer characteristic combustion time of 1.55 ms than Jet-A1. This increased time delay correlated well with an additional convection time due to the increased lift-off height in HEFA and was therefore indirectly linked to the faster evaporation. Timescale analysis let to the assumption, that evaporation rate is the dominant factor for the lean blowout in ambient and near jet engine condition, which was shown by the LBO results. In both conditions, the difference in LBO limit between the two fuels exceeded the difference in evaporation rate, indicating an additional contributor, assumed to be the difference in calorific heat value.

The results of this research imply, that utmost care needs to be taken when developing new ultra-lean combustion technologies for multi-fuel usage. Well established fuels were used in this work to indicate, that known fuels with a small difference in evaporation rate can lead to a shift in flame position, with an accompanying increase in characteristic combustion time. Although not observable in this work, such an additional delay can lead to different periodic fluctuation or other combustion instability phenomena.

List of Figures

List of Tables

Chapter 1. Introduction

An increase in population and demand for fast and easy transportation all around the globe are just two main reasons for growth in energy consumption, especially fossil fuel conversations like in stationary gas turbines and in aviation. Although, the current coronavirus crisis have reduced the demand for fossil fuels overall, most drastically in the aeronautic sector, but this trend is only temporarily and as soon as the global pandemic is under control, the fuel consumption will increase again, probably even more than before the crisis, to compensate for the lost time or rather for the economic stagnation due to the virus.

Before the outbreak, climate activists, such as Fridays for future, have indicated, that little to nothing has been done, to reduce impacts on climate change. Everyone is screaming for the need for alternative energies, change in combustion society, demanding new technologies for a cleaner environment. Although new propulsion systems seem to be emerging within the automobile industry, it is inconceivable for the airborne transportation sector, to propel an airplane without combustion, especially when it comes to long-distance transportation like transatlantic flights, or rocket launches.

The mentioned increase in energy demand, coupled with the depletion of fossil fuel sources and the awareness of their impact on the environment have scientists and researchers motivated to focus on alternative and efficient ways to compensate for those human needs with keeping the influence of pollution to a minimum.

Improvement in aviation technology focused on reduction of friction and drag of the whole airplane, more efficient compressor and turbine stages by optimizing the fluid flow around their blades due to experimental and numerical analysis and the development of new combustion technologies, which should burn fuel in a more efficient and environmentally friendly way compared to the current systems. Especially combustion has still a big potential regarding improvement. Additionally, the idea of changing the combustion system is the use of alternative fuels, which have a better overall carbon dioxide footprint or just producing less pollution than their conventional counterpart.

In the following subchapters, three main points, the environmental impact of aviation, combustion technologies for jet engines and alternative jet fuels are briefly introduced, which lead to this work's objective.

1.1. Impact of aviation on environment

As mentioned before, with an increase in globalization, the personal and professional need to go anywhere at any time and the availability of simple and cheap transportation via airplane, the increase in air traffic in the past and several forecast scenarios for the future can be seen in Figure 1. While land and sea transportation offer market mature alternatives, such as electromobility based on electricity from renewable sources, e.g. hydrogen-powered fuel cell, this is not the case for aviation yet. Especially not on a large scale, e.g. transatlantic flight. Each passenger-kilometer spent in air produces a certain amount of air pollution, such as nitrogen oxides (NOx), carbon dioxide (CO_2), carbon monoxide (CO), soot (particles) to name only a few.

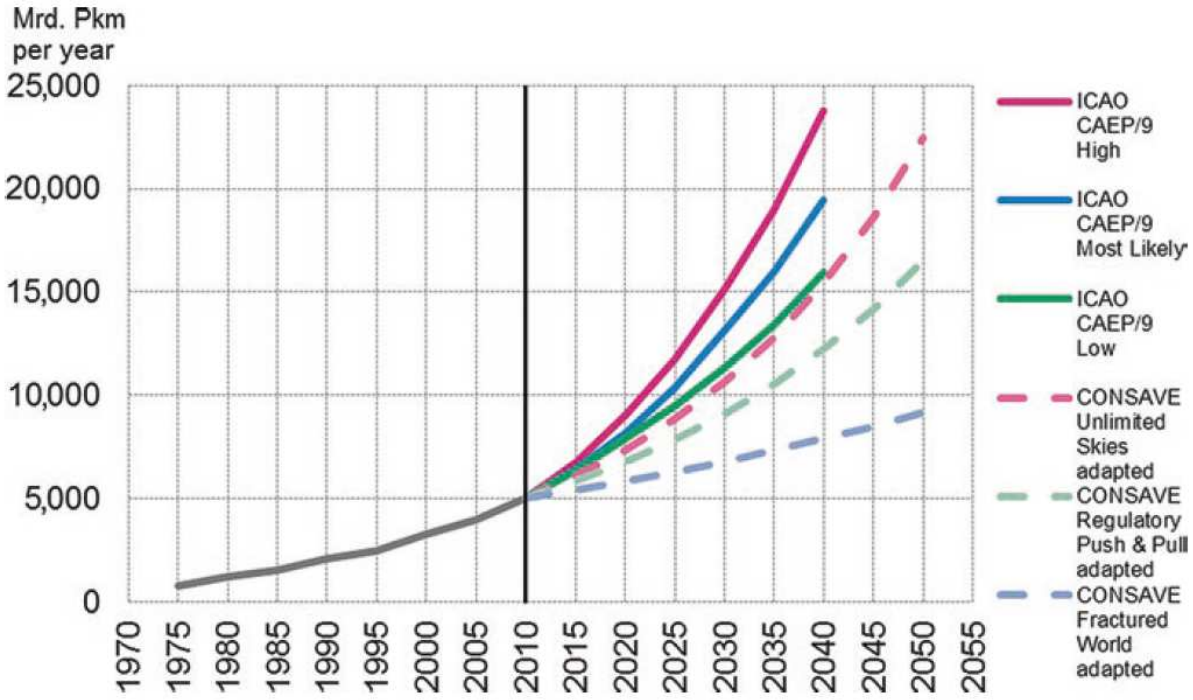

Figure 1: Examples of scenarios and forecasts for the global air transport performance (measured in passenger-km's (PKM) transported per year) [1] *(permission from publisher for reuse)*

Figure 2 shows the time history of CO_2 increase in the past, and several scenarios, how much the carbon dioxide impact increase if nothing will be done, compared to different steps against the increase in pollution. To reach the goals, the United Nations (UN) set at their annual climate change conferences, an immense reduction of pollutants needs to be realized, to not further increase e.g. CO_2 impact, and in the best case even reduce the current output. As can be seen in Figure 2, this can be only accomplished with the development and usage of alternative technologies and biofuels.

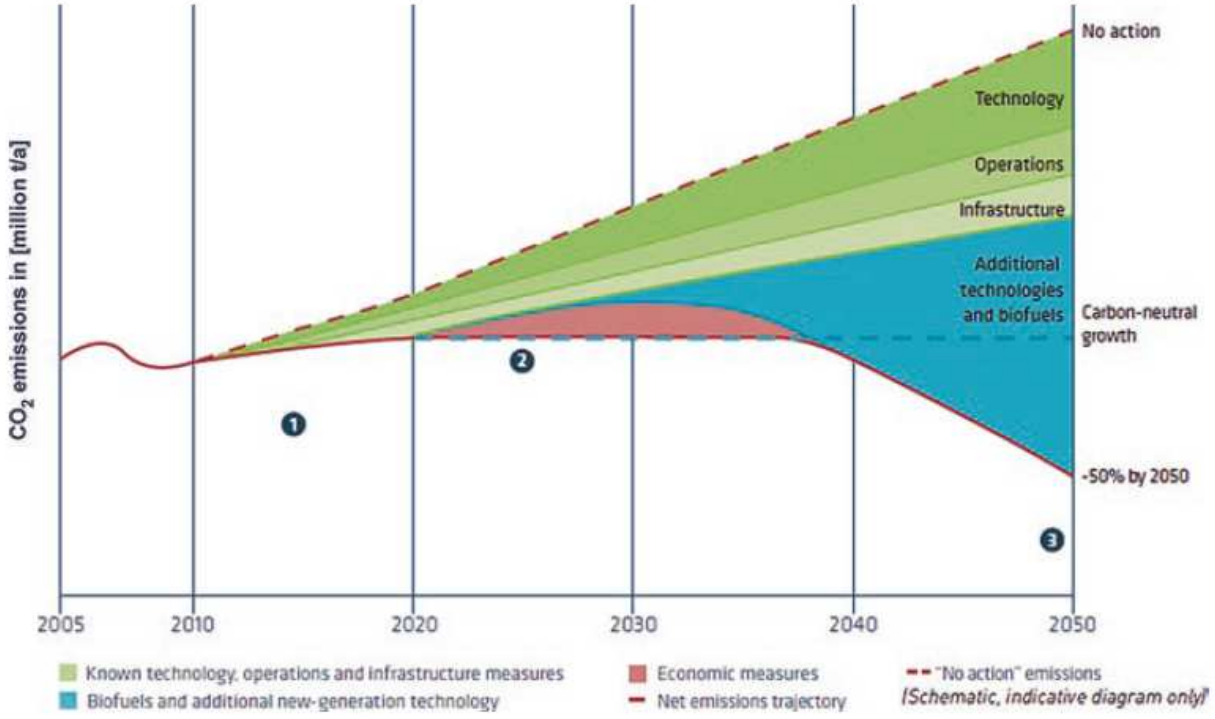

Figure 2: Development of CO_2 emissions depending on technologies and legislation [1] *(permission to ruse from publisher)*

The International Civil Aviation Organization (ICAO) constantly works on reducing emissions caused by air traffic. Over the last two decades, stricter regulations ensured a reduction of nitrogen oxides by roughly more than 40% in the aviation sector, which is predicted to be continued within the next couple of years [2]. Further development of combustion technologies is one possible way to accomplish the predicted standards, usually published by the Committee on Aviation Environmental Protection (CAEP). Those new developments include e.g. a Twin Annular Premixed System, such as shown in Figure 3b. In general, a conventional propulsion system for aircrafts changes the amount of injected

fuel (equivalence ratio) depending on the necessary power output, where for low power (idle) less fuel is needed, and for high power (full throttle) a lot of fuel is combusted. Such conventional systems typically produce a lot of soot and other emissions at high fuel consumption. They also reach a high temperature in the combustion chamber, leading to a higher amount of nitrogen oxides. A staged combustor on the other hand remains in a rather low-temperature region, and therefore result in fewer nitrogen oxides, because of the combustion of lesser fuel [3].

1.2. Combustion Technologies for Jet Engines

As mentioned, the demand for lower environmental impact from the aviation industry motivated the development of new technologies for the reduction of emissions. A reduction of pollution is one of the most important key factors for new technologies, but there are several other design elements, which must be considered when developing low emission propulsion systems. The most obvious ones are: altitude relight capability, combustion stability, pressure loss, autoignition/flashback risk, combustion efficiency, size/weight, overall and radial temperature distribution factor, and liner durability [4]. Lean combustion technologies are one of the most promising new technologies for emission reduction, which explains their intense research in recent years. Reason for combusting lean has the benefit of producing lower emissions compared to richer more common technologies. This results from lower temperature inside the combustor, which leads to lower NOx production (thermal NOx), but also due to higher possibility to reach complete combustion because of excessive air amount, which additionally leads to a reduction of unburned products such as CO and HC. Disadvantages when combusting at such low air-fuel-ratios are lean blowouts, flashback and a higher chance for combustion instabilities, which in the worst case could damage the combustor interior [3]. Therefore, limits and more knowledge of those technologies are necessary, to create enough safety margin, for a safe transportation of pilots and passengers. The goal of modern research in the field of jet engines is the increasing of combustion efficiency, with simultaneously lowering the fuel consumption and therefore the environmental impact, without compromising safety.

Depending on the amount of fuel compared to the amount of oxidizer (usually air), the combustion condition is either called rich or lean, where an excess fuel amount is described by the former and a deficiency of fuel amount is described by the latter. At stoichiometry, the reagent and agent exist in an optimized amount, which allows theoretically a complete combustion according to the chemical reacting equation, based on the conservation of mass. In other words, all fuel is used with no deficiency nor excess. Therefore, each fuel has a specific amount of oxygen or air, to reach complete combustion. This fuel-oxidizer ratio is described with the equivalence ratio φ (equation (1), where $\varphi = 1$ represents the stoichiometric condition.

$$\varphi = \frac{\left({}^{m_{fuel}}/_{m_{air}}\right)_{actual}}{\left({}^{m_{fuel}}/_{m_{air}}\right)_{stoichiometric}} \quad \text{or} \quad \varphi = \frac{\left({}^{m_{air}}/_{m_{fuel}}\right)_{stoichiometric}}{\left({}^{m_{air}}/_{m_{fuel}}\right)_{actual}} \qquad (1)$$

With an increase in equivalence ratio, the flame temperature increases, reaching maximum at equilibrium or rather slightly rich condition, leading to an unwanted chemical reaction, such as the creation of nitrogen oxides (thermal NOx) [5]. Additionally, in the case of highly excess fuel, a strong amount of soot and incomplete combustion products are produced as well [6]. Therefore, as mentioned above, new developments in combustion technologies shift towards lean combustion, which is also the combustion field, this work will deal with.

Combustion and combustion technologies can, additionally to their conditions (rich, lean), also be categorized into non-premixed and premixed combustion. For a reaction to take place, fuel and oxidizer need to be mixed sufficiently on a molecular level. Therefore, the mixing process is of crucial importance and can strongly influence the behavior of combustion systems. In a premixed system, the reactants are well mixed before the reaction occurs. However, in a non-premixed design, fuel and oxidizer are initially separated and brought together through transportation and diffusion to react in a common area [5]. This can prevent harmful combustion behavior, such as flashbacks, and is therefore, a more protective method for injectors and other upstream parts. A non-premixed lean combustion injector for example is an airblast injector or a Lean Direct Injection (LDI), where fuel is directly injected within two swirling air flows and transported into the combustion chamber (Figure 3a and Figure 3b). LDI is recently of high interest due to its low emission characteristics at high temperature and high-pressure operation. Airflow is used for both, atomization and transport of the fuel into the combustion chamber. This minimizes autoignition and/or flashbacks. Though, as mentioned, such technology has a higher possibility for a blowout and lean combustion instability.

A premixed injector mixes fuel and air long before the combustion chamber to ensure homogeneity of the mixture. In the case of liquid fuels, this often involves a sufficient long mixing length to guarantee sufficient evaporation. Such a premixed process is typically used in new injector developments such as Twin Annular Premixing Swirler (TAPS) and is schematically shown in Figure

3c. In such a design, the fuel injection is staged, which separates the inlet into a pilot and a main injection. Figure 3c shows, the pilot injector (center axis) has a long mixing length towards the combustion chamber, compared to the airblast injector and LDI in Figure 3a) and Figure 3b), respectively. In the case of the main injector, which is concentrically ordered around the pilot injector, the fuel is injected into the swirling main airflow before entering the combustion chamber. Therefore, both stages can be considered premixed for the shown example. If the operating condition is lean and the fuel is heated up to start evaporating within the fuel pipeline or can be ensured to be fully evaporated before entering the combustion chamber, the system is called a Lean Premixed Prevaporized (LPP) injector [4]. Often mistakenly confused as LPP, the TAPS (Twin Annular Premixing Swirler) as in Figure 3c) is often used in academic research, to analyze the interaction between main and pilot burner. A TAPS injects the fuel into the airstream further upstream, to reach a burnable mixture when entering the combustion chamber. Prevaporization is often reached simultaneously, due to the hot incoming air, produced by the compressor stages before the combustor in a jet engine. The prevaporization and premixing also ensure a complete mixture of fuel and air, which reduces possibly hotspots in the combustion chamber. As mentioned before, with an operation on the leaner side, instabilities or even blowout can occur, which in the case of an LPP might lead to flashbacks and causing damage to the injector or other sensitive parts. Although its name implies premixed and prevaporization, the center injector of an LPP, the pilot injector, exhibits often non-premixed operation. It has often two operator modi: 1) stabilize the typically much leaner main burner, and 2) provide combustion as a single injector during low power operation (idle mode, sub-idle mode). In total, the equivalence ratio will be lean, but since most of the air will go through the main burner (outer part or 2nd stage), local rich or "richer" conditions can be reached at the exit of the pilot burner which may lead to non-premixed or at least partially premixed combustion, since not all fuel can be evaporated, due to the sheer amount.

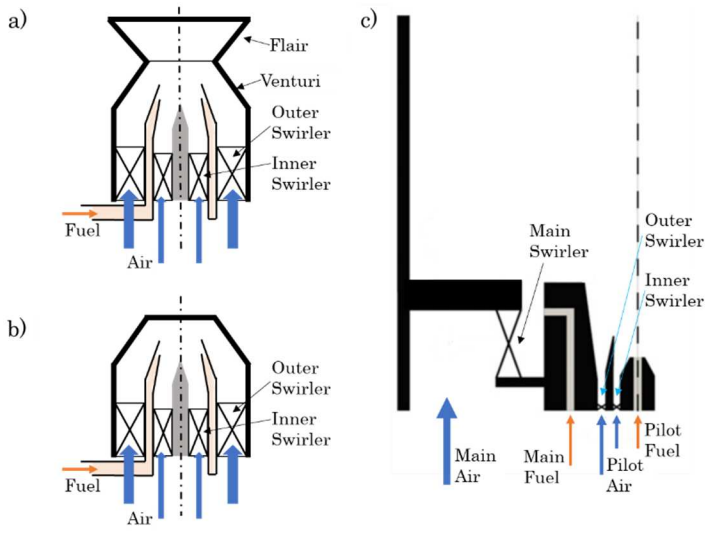

Figure 3: a) Schematics of an LDI injector (based on [7]*); b) Schematics of an airblast injector; c) Schematics of a Twin Annular Premixed Injector (based on* [8]*)*

1.2.1. Injection technology

In the field of combustion, atomization is an important process to disintegrate liquid fuel into small droplets in form of a spray, which is typically used in various combustion processes, such as rocket engines, internal combustion engines, gas turbines. Within the combustion field, atomization has the main effect to create a big surface, therefore the more the liquid is separated into small droplets, the better it is for the combustion since the droplets can evaporate quicker and the evaporated gas mixes faster with the surrounding air or oxidizer. A simple analogy would be to compare a bucket full of water, and the same amount of water spread over a wide surface such as a kitchen floor. The water on the floor will vaporize much quicker than the water in the bucket, due to the wide-spreading over a big surface. Furthermore, in gas turbines or internal combustion engines, atomization plays a major role when it comes to emission control of NO_x, CO_2, and unburnt hydrocarbons. This comes from the relation, that droplet size and later on the air-fuel mixing process can influence ignitability and flame stability. E.g. it is much easier to burn diesel fuel, jet fuel or cooking oil when atomized, rather than in their "calm" or "collected" state. The mixing process inside a combustion chamber consists of the dissipation of the liquid, forming a homogeneous mixture and create an optimum spatial distribution

inside the chamber. For combustion efficiency in terms of combustion, performance and emissions, the introduction of liquid fuel into the combustor plays a key role. Therefore, it is of crucial importance, to know what kind of spray and atomization quality an injector delivers [9].

Atomization process, in general, is caused, when a strong relative velocity between atomizing liquid and surrounding gas exists to either disrupt the liquid into little pieces which later form droplets or to cause an instability onto the surface which also result in a breakup of the liquid to droplets. Several atomization technologies were developed over the course of the last decades, depending on the application they are used for. A few examples are pressure atomizer, where a liquid is pressurized and ejected through a small orifice into a relatively slow or even quiet gas like a volume filled with air; rotary atomizer, where a high-speed disk atomizes liquid, which enters the disk at the center and leaves the disk at the edge; air-assist atomizers, where a liquid is exposed to high velocity streaming air flow, atomizes and mixes with air within the injector before being discharged; and airblast atomizers, which function similar to air-assist atomizers, though atomization and mixing happen at the edge and outside of the atomizer, respectively. Both air-assist and airblast atomizer, belong to the group of twin-fluid atomizers [10]. Especially the airblast atomizer is of importance for this study, therefore it will be discussed in more detail from here on.

Compared to air-assist atomizer, the airblast injector uses a much higher quantity of streaming air at a much lower velocity. Airblast injectors are therefore well suited to be used in continuous-flow combustion systems, such as jet engine combustors. Usually, the liquid is spread over a thin conical sheet and exposed to a high-velocity airstream on both sides of the sheet. This kind of liquid spreading is also called prefilming [10] and can be seen in Figure 4a.

The breakup of liquids can be described with the Weber number We, which is a dimensionless parameter and represents the ratio of inertia force (aerodynamic force) to surface tension force. It can be calculated with

$$We = \frac{\rho v^2 l}{\sigma} \qquad (2)$$

where ρv^2 accounts for the aerodynamic forces and σ/l indicates the surface tension forces. The higher the Weber number, the higher are the deforming compared to reforming forces and therefore the stronger or rather earlier the atomization/breakup starts. Generally, a disruption in the flow causes a disturbance that propagates as a wave along the surface, which then causes the liquid film to "oscillate" and result in a flapping of the film which leads to the production of filaments. The filaments then separate further into droplets.

Typically, atomization is influenced not only by the design of the atomizer itself, e.g. in the case of prefilmed atomization the prefilming sheet thickness but also by liquid properties of the atomizing medium and the ambient condition of the gaseous medium. Those liquid properties are density, viscosity, and surface tension. Lefebvre et al. [10] stated that the influence of the density of liquid diminishes because most liquids exhibit only a minor change in that property. Surface tension represents the force that resists the formation of new surface area, in the case of atomization the formation of ligaments and droplets. This relation can be described with the Weber number, which was already mentioned above. Surface tension usually changes with relative density (when comparing different liquids), as researched by Christensen et al. [11], and reduces with an increase in temperature. The effect of viscosity onto atomization is of similar importance than the effect of surface tension, but viscosity also affects the fuel flow rate inside the injector as well as the spray pattern. An increased viscosity additionally reduces Reynold's number, which hinders natural instabilities to develop in the liquid sheet. In general, due to the delayed disintegration of the liquid sheet, it results in a bigger droplet size. In the case of airblast atomizers though, since liquid velocities are much lower, e.g. in comparison with pressure atomizer, the drop size tends to be less sensitive to variations in liquid viscosity. Like surface tension, viscosity decreases with an increase in temperature, therefore, heavy oils are often heated up in real applications to improve atomization but also to reduce pumping power. As mentioned, the ambient condition might also influence the atomization, especially for fuel fired combustion system such as jet engine combustors. In that case, the ambient gas density can affect the mean drop size. Spray pattern though, at least in case of airblast atomizers tend to be insensitive

by the variation of ambient gas density. All but the largest droplets will follow the streamlines of the airflow pattern.

In Figure 4, several versions of airblast injectors can be seen. Figure 4a shows a prefilming version of an airblast atomizer. Such a type first spreads out the liquid mostly on a cylindrical inner wall and atomizes at the edge, where the two air streams are meeting, as indicated in the image. The disadvantage of such an atomizer is often the bad atomizing quality at low airflow rates. For that reason, a hybrid airblast injector was developed. Such a hybrid system has instead of the center body in Figure 4a often a pressure swirl atomizer or a simplex nozzle as the primary atomizer [10]. It basically "pre-atomizes" the liquid, before being exposed to the airblast injector part. A third option can be seen in Figure 4b, where a liquid is directly injected after a swirling airflow. This design is called a plain-jet atomizer in which several holes circumferentially distributed are responsible for an equal spread of the liquid in a typical cylindrical ring. This design is often used for simple solutions of a 2nd stage injector (pilot-main injector system, e.g. like Lean Premixed Prevaporized Burner).

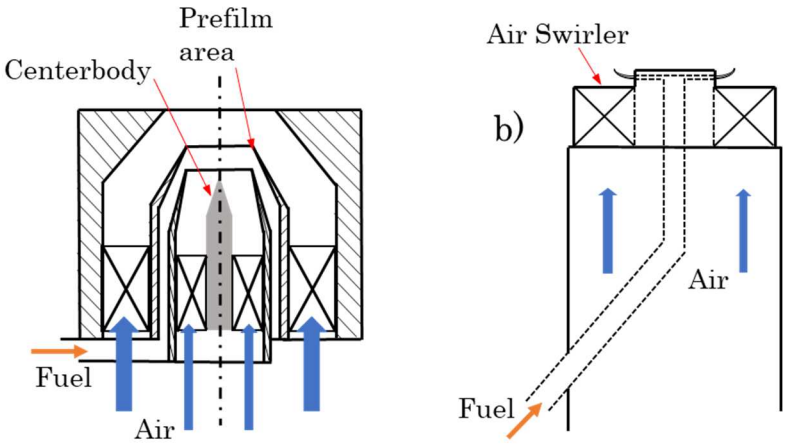

Figure 4: Different examples of airblast injectors (based on airblast injectors in [10]*)*

1.2.2. Swirl stabilized flame

Typical jet engine combustors are operating on a wide range of combustion pressure and incoming air flow rate. The compressor stages before the combustion chamber create an incoming air flow speed into the combustion chamber of up to 100 m/s, which expands due to the geometry of the combustion

chamber to 10-35 m/s [9]. Nevertheless, these velocities are too high for stable combustion, since conventional jet fuels, after complete evaporation and mixture, have flame speed values of 10-300 cm/s (depending on fuel, equivalence ratio, inlet temperature and pressure), which is way less than the average flow speed inside the combustion chamber [5]. This means, the flame would not be able to propagate properly, which would induce blowouts, flashbacks, and other unwanted behaviors. Therefore, it is of importance to create at least one point inside the combustor's flow field, which offers a reduced flow velocity, where the flame can anchor and propagate from. For high velocity flows, such as inside a jet engine combustion chamber, a recirculation zone is employed to stabilize the flame. Such a recirculation zone does not only reduce flow velocity in a certain region, but also recirculates hot products and radicals, and promotes mixing, which also supports flame stabilization. There are three ways to create recirculation zones inside a combustion chamber: 1) sudden expansion e.g. by a step or dump combustor, 2) swirling flow expanding, which leads to a vortex breakdown or 3) at the wake of a bluff body. All three options can be seen in schematic form in Figure 5. In case of a "simple" sudden expansion, a corner recirculation zone (CoRZ), or also called an outer recirculation zone (ORZ) is created, which is a little bit geometrically shaped like a donut within the corner of the combustor wall and face plate of the combustion chamber. The bluff body and the swirl flow create an additional central recirculation zone (CRZ) or also called inner recirculation zone (IRZ), shaped like a bubble around the centerline of the combustor. A bluff body has the disadvantages to be very close to the flame and therefore might exhibit heat damage to the material, additionally, in the case of non-premixed liquid-fueled combustion, droplets might accumulate on the surface of the bluff body and disturb stable spray formation.

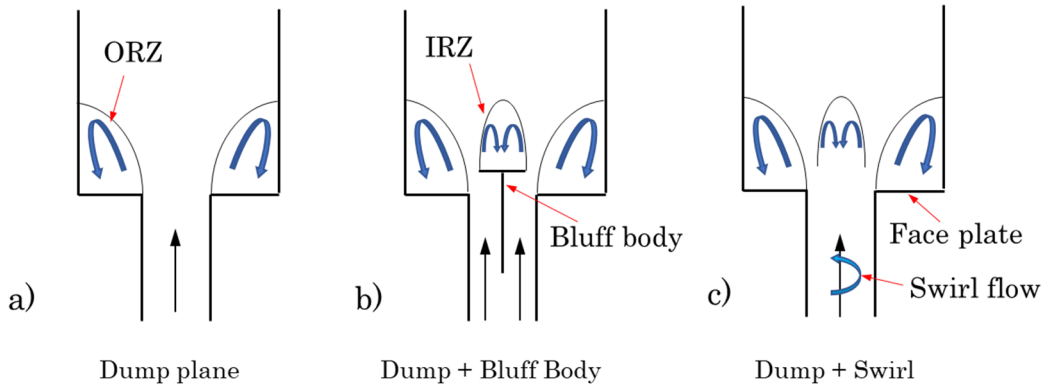

Figure 5: Examples to create recirculation zones

Swirl stabilized flames can differ greatly, depending on the intensity of the swirl. Typically, a swirler (e.g. a cylinder with helically shaped blades), such as in Figure 6, causes the incoming air to change its trajectory from straight to rotating, which adds radial and azimuthal components to the flow direction. Depending on the blade angle, but also on the size of the used swirler, the intensity of the swirling flow changes. When such a swirling flow then expands suddenly, a vortex bubble around the centerline forms, which breaks down at the downstream end and greats a recirculation zone. This is known as vortex breakdown (VBD). Simplified speaking, when a swirling flow suddenly expands, due to centrifugal forces, a pressure gradient in a radial direction is created, with the lowest pressure region near the injection point. With increasing distance from the injection, swirl flow diminishes, and so also the swirl created pressure gradient. This means, the pressure downstream is higher than the pressure near the injector, which results in a reversed flow, known as the central recirculation zone [12].

Figure 6: swirler for an airblast injector configuration a) example for an outer swirler; b) example of an inner swirler

The intensity of the swirl additionally can change the flow behavior drastically. In fact, it has been shown by several researchers, that with an increase in swirl (swirl number), the recirculation zone increase and can also move further upstream [13][14]. A low swirl intensity has no particular strong influence on the flow field and is similar to a dump plane inflow (Figure 5a), an intermediate swirl causes a central recirculation zone as explained above, and a high swirl causes a central recirculation zone or a vortex breakdown bubble with the diameter similar to the combustion chamber diameter. In this case, the flow field will attach to the wall. The high swirl flow field is often called a Coanda-effected flame, flat flame, or sunflower flame. Due to the strong swirl, the flow will be brought close to the wall, and because of the higher flow speed, locally low-pressure zones are caused near the wall, which causes the flow to attach. Consequently, the flow is forced to move along the wall and is redirected in the corner area towards the downstream direction.

1.2.3. Combustion Issues

Lean Blowout (LBO)

As mentioned in the above sub-sections, the focus of new combustion technologies in jet engines is on the lean operation. The leaner the condition, the more unstable the combustion can become, where blowout at the lean limit occurs. Therefore, the most straightforward explanation for lean blowout is a too strong dilution of the fuel by air (too lean mix), and the resulting flame cannot stabilize or rather anchor itself anymore in the current condition. Sometimes, it is also referred as “static stability” [15]. Flow speed in realistic combustion systems typically exceeds propagation flame speed by far, therefore stabilization is necessary, which reduces flow speed or creates an area within the combustion chamber with lower flow velocity, as mentioned in the previous sub-section. Independent of the stabilization method, the flame can only be stabilized in a certain range of conditions. E.g. the flame is stable at a specific equivalence ratio, but with increasing air flow rate, the flame will eventually blowout. Similar behavior will happen, when keeping the air flow speed fixed and decrease the fuel flow rate. This behavior is often explained with the ratio between two-time scalar, the chemical kinetic time and the residence time, which describes the Damköhler number Da. The chemical timescale describes how

much time is necessary for the mixture to react. The residence timescale indicates how long the reactants stay within the flow field where a reaction can occur. Researchers arguing about the origin especially for chemical timescale. Damköhler number is more or less simply used in case of premixed and/or prevaporized combustion, but in case of non-premixed and additionally liquid fuel injection, utmost care needs to be taken, to evaluate appropriate parameters for Da.

Figure 7 shows, that atomization, evaporation, fuel-air-mixture quality, chemical kinetics, and ignition can all influence the blowout limit. Despite all those influential characteristics, typically a smaller number are the dominant factors. This is strongly dependent on system design and condition [16]. Each of the influential parameters can be expressed with a timescale τ, representing the duration of those processes, but as schematically shown in Figure 7, the timescales are partly dependent on each other, which makes it difficult, to detect the responsible factor for the Lean Blowout.

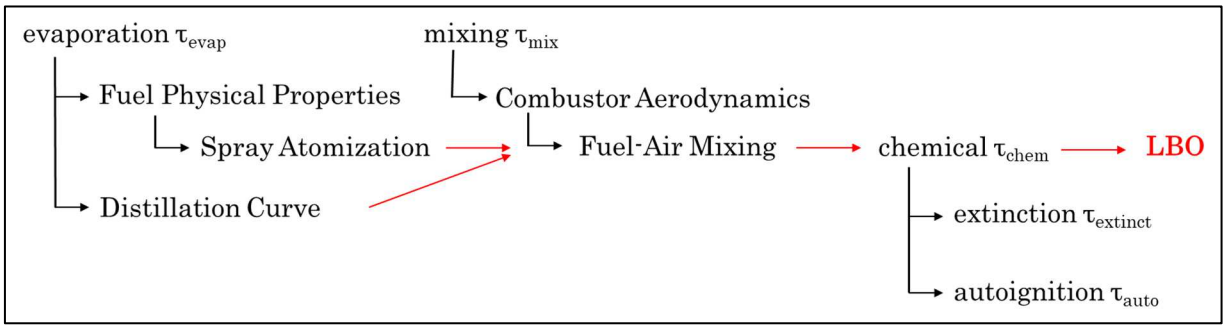

Figure 7: Possibly time scale influences on LBO (based on [17]*)*

Combustion instabilities

Combustion typically produces noise. When such combustion is confined, as in a jet engine, the produced noise can be either reflected or travel through acoustics and/or convection, e.g. due to recirculation zone, often created in a jet engine combustion. The resulting pressure amplitudes from such instabilities can lead to major damages to the combustor interior or the upstream injector systems. Such devastating forces occur, when a positive feedback between the acoustic field of the system and the unsteady heat release rate occurs, which means the system is fed with energy from the combustion. The large growth of pressure and velocity amplitude lead to performance loss, increase pollution,

thermal stress, vibration influencing control-systems and unstable flame behavior which leads to blowout and flashback [18].

Combustion instabilities can have their origin in different modes, such as longitudinal, transversal, azimuthal, hydrodynamic, and bulk (or Helmholtz), to name a few. A real jet engine can exhibit several of each group, which makes it difficult to find out which frequency belongs to which mode. Compared to laboratory model combustor, where only single to a handful of instability modes usually occur. This makes it simpler for analysis but can also lead to an oversimplification of the combustion system. Nevertheless, by reducing the possibilities of modes, the chance increases to better specify each mode and draw a conclusion for real jet engine modes as well. The most prominent hydrodynamic mode is the precessing vortex core mode (PVC), which is a helical "worm" moving along the shear layer of the swirl induced flow. PVCs can trigger certain combustion instability modes, disappear when the flame is ignited, or appear only for certain flame positions [19]. A PVC can often simply be identified by changing the inlet velocity because the PVC frequency changes linearly with air velocity, which means an increase in airflow rate by two would also double the PVC frequency. It was also shown, that an increase in swirl (higher swirl number) would increase the PVC frequency as well [20][21].

A longitudinal mode is related to the combustor's design and the sonic speed, which depends on the gas temperature inside the combustor. The longitudinal mode is related to the standing waves in a pipe, which is based on the same principle of how the tone of a flute is physically created. Depending on the boundary conditions at the entrance and end of the pipe (open or closed), a half or quarter-wave is created inside the combustion chamber. A Helmholtz mode can be easiest created by blowing over the edge of an open bottle. The air stream over the edge creates fluctuations, which then propagates through the neck of the bottle and reflect in the main volume of the bottle, which creates the sound. This often happens in a jet engine, where the swirler path and the combustor volume create the necessary geometric combination, responsible for this mode. A complicated design such as a real jet engine can have several Helmholtz frequency modes. There are several other modes possible inside the combustor, but the presented ones are the most prominent.

Each mode corresponds to a specific frequency, and to the reciprocal of the frequency, its time period. If this time period corresponds well to a timescale within the combustor, for example, convection time from inlet to the exit, convection time from the injector to the flame front, or combustion time from injection till the maximum heat release rate, it is often stated in the literature, that corresponding eigenfrequencies can be triggered, leading to combustion instabilities with that specific frequency.

1.3. Alternative Fuels

As mentioned at the beginning of this chapter, one way for reducing the environmental impact of air traffic vehicles is to replace conventional jet engine fuels with alternative biofuels. Research on alternative biojet fuel exists already for two decades, with the first flight with a blended biofuel being conducted in 2008 [1]. Several different production paths for alternative jet fuels have been established in the past, showing the most prominent ones in Figure 8. Generally, they are divided into, Oil-to-Fuel (OTF), Gas-to-Fuel (GTO), Alcohol-to-Fuel (ATO), and Sugar-to-Fuel (STO) alternative fuels.

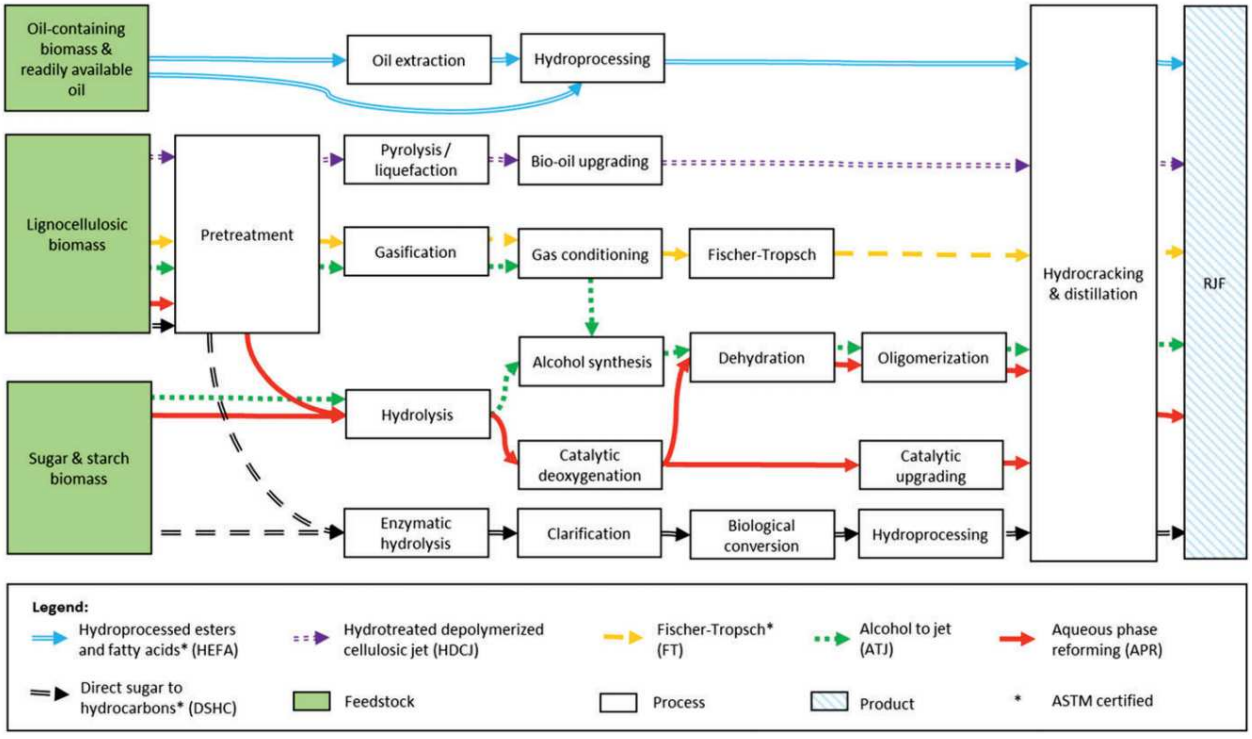

Figure 8: RJF conversion pathways: feedstocks and processes [22] *(permission from publisher for reuse)*

Figure 9 gives an overview of six different renewable jet fuels (RJF) and their development levels. Hydroprocessed Esters and Fatty Acids (HEFA, old name hydrotreated renewable jet fuel HRJ) and Fischer-Tropsch (FT) jet fuels are the furthest developed RJFs so far. Both have reached commercialization, though HEFA is with its Fuel readiness level of 9 the most developed one. It is ASTM certified, has been used for the majority of RJF flights to date, and is produced at three commercial-scale facilities [22]. HEFA is derived from renewable fuel sources, e.g. vegetable oil, but it requires hydrotreatment to condition the oil to jet-fuel quality. This fuel is also called bio-synthetic paraffine kerosene (bio-SPK) and has the potential, to be carbon neutral, since the carbon, emitted during combustion, can be offset by the carbon absorbed during the growing process of its feedstock. Thus, it is a valuable fuel to greatly reduce carbon emissions [23].

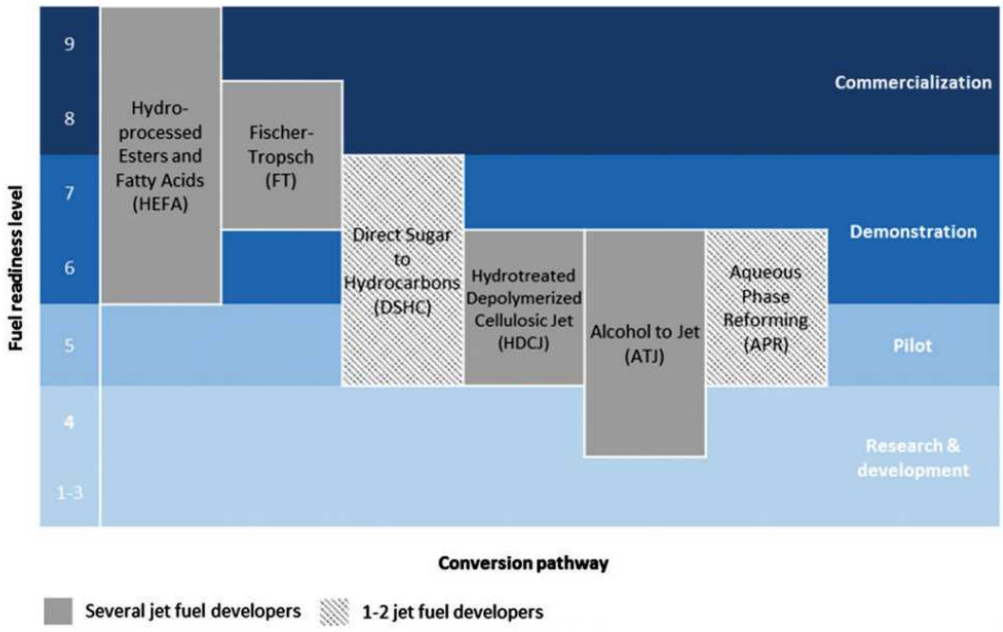

Figure 9: fuel readiness levels 2016 of RJF conversion technologies [22] *(permission from publisher for reuse)*

HEFA was certified with the ASTM D7566 standard (specifically with ASTM D7566-11) in 2011 to be used as a blend-in with conventional jet fuel at a ratio of 50:50. This limitation in blending of HEFA with conventional jet fuel (e.g. Jet-A1) to 50% results from compliance with specific fuel property limits. Typical examples are freezing point, volatility, density, viscosity, smoke point, etc. The minimum limitation for aromatics e.g. is 8 vol%, HEFA, on the other hand, has <0.1 vol% [24]. Aromatics play a

key role in aviation fuels as they enhance the density and elastomer swelling properties of these fuels, which influence sealing properties of o-rings and the likes. However, most bioderived fuels have little to no aromatic amount in their compositions. Therefore, it is one of the main reasons, why HEFA and FT fuels can only be blended with a maximum amount of 50 vol% to conventional fuel such as Jet-A1 [25].

Typically, physical and chemical properties of alternative jet fuels are tested, to make sure they are within certain boundaries. After mixing, their properties are tested again. Tests also include ground and flight tests, as well as thermal stability. Those tests usually focus on the fuels result in currently commercialized jet engine technologies. Regarding the mentioned newer technologies in the previous sub-chapter, which focus on lean combustion, the behavior has not been completely understood yet. One aspect of new drop-in or alternative fuels is, that due to the different physical and chemical properties, those fuels might have different combustion behavior at lean conditions, which might lead to combustion instabilities when using the same combustor design.

1.4. Literature study

There exists a multitude of research regarding timescale analysis and lean blowout property correlation when it comes to gaseous fuel combustion, but a more limiting number of publications when it comes to liquid fuel combustion. Comparing to gaseous fuels, liquid fuels also have to deal with atomization and evaporation as well, which makes the process more difficult to describe. On the other hand, gaseous fuels most likely to mix faster and can cause other combustion phenomena, interfering with stability.

Combustion performance is often described or related to physical processes like heat transfer, fluid dynamics, or thermodynamics. Fuel property effects on gas turbine combustion is a rather important topic, especially because several fuel properties interact with each other, and therefore can cause confusion which property is responsible for which behavior. Typically, researcher tries to find connections between several properties, physical and chemical, such as density, surface tension, and

viscosity, which strongly affects the atomization process in liquid-fueled jet engines, and distillation temperatures, which are related to evaporation or derived cetane number, which gives assumption over ignitability and chemical stability.

Different combustor or injector designs have shown different responses when operated with the same fuels, which might be related to the difference in response time, like convection, comparable to the delay times caused by the combustion process of each fuel [17]. Researchers, therefore, try to isolate certain effects by specifically design their apparatus, so only a particular fuel property affects the combustion. This is without a doubt not an easy task. Venkataramani et.al [26] isolated fuel volatility effects from atomization effects. His study focused on physical fuel properties, and the injector was operated to always provide a Sauter Mean Droplet Diameter of 50 μm for all test fuels, while the volatility of the fuels spread over a wide range. They found that an airblast atomizer exhibit poorer ignition performance and a stronger dependence on volatility than a pressure atomizer.

Lefebvre et.al [27] tested a wide range of fuels, at several gas turbine designs, to find out their lean limit performance, ignitability, emissions lean light-off limits, etc. depending on the fuel properties. The results showed that atomization quality and evaporation rate are mostly affecting lean blowout. Additionally, fuel chemistry had only a minor influence on lean blowout.

Ballal and Lefebvre [28] derived a theoretical model to determine the minimum quench distance in liquid fuel sprays. In their model, the thermal diffusivity divided by the laminar flame speed formed a strong influence on the quenching distance and therefore is acknowledged as an influential parameter for LBO limit.

With all these indications of fuel influencing LBO and other combustion parameters, interest grows to stronger analyze the combustion performance of bioderived alternative aviation fuels. Since the influence on combustion can not only cause a positive but of course also a negative effect compared to conventional petroleum-derived jet fuels. Several studies reported that ignition and extinction behavior being influenced by fuel composition. However, results are quite diffusive, ranging from appreciable to relative neglectable influence ([29][30][31][32]).

Fyffe et al. [30] tested several alternative jet fuels on the basis of GTL (gas-to-liquid) to investigate altitude ignition and evaluation of extinction at two test conditions (simulation of altitude). The report concluded that a lower iso/normal paraffin ratio improves ignition behavior.

Burger et al. [33] tested 16 different fuels in an in-house combustor at an air inlet temperature of 310 K. Their injector was based on a simplex pressure atomizer and the results showed a strong correlation of the blowout limits towards volatility (those with the lowest T_{10} values where most blowout resistant) and a weak negative correlation towards Derived Cetane Number (DCN).

Rock et al. [31] examined experimentally the lean blowout in a swirl-stabilized combustor and compared pressure with airblast injector. The research included three petroleum-based fuels and five renewable jet fuels to cover a wide range of physical and chemical properties. The goal was to elucidate the influence of physical properties and chemical kinetics on lean blowout behavior. The lean blowout limit in the case of pressure atomizer showed strong correlation to the physical properties of the fuels, especially to boiling point temperature. Interestingly, fuels with disadvantages in atomization and evaporation reached lower LBO limits. This statement is in accordance with Lefebvre's theory [27], that delayed or extended atomization/evaporation can be beneficial for lean limit combustion. The reason for that are localized richer spots, which can globally stabilize the combustion better compared to well premixed lean condition. It was further detailed, that this behavior happens if the air inlet temperature were above the fuel flash point and the opposite behavior would happen if the air temperature is below the fuel flash point temperature. They concluded that lean blowout is in good agreement with C/H ratio, iso-to-normal paraffin ratio, and fuel smoke point of the tested fuels, but the strongest relationship of LBO was found to be with the T_{90} values. Though, the same paper stated no clear correlation between fuel physical properties and atomization quality in an airblast injector. Rock states the best correlation found, was the iso-to-normal paraffin ratio to describe LBO stability, which could be related to the chemistry sensitivity of the fuel. However, under further inspection, a negative correlation between LBO and the DCN could be found, which is confirmed in more recent publications of Rock et al. [34]. Nevertheless, Rock et al. [31] mentioned the efficient atomization of the airblast injector as the reason for the non-existing correlation of LBO to the physical properties of

the fuels. Small droplets were likely less physical property sensitive and give an opportunity to chemical kinetics to take the lead in LBO correlation. Although these comparison methods of Burger [33] and Rock [31][34][35][36] give a well-fitting explanation over a wide range of fuels, they do not clearly show the combustion behavior, nor the effect of mentioned physical property. In fact, those results can often be diffusive or deceiving, because the geometry of the combustor and especially the fuel injector can have a strong impact on the combustion, by amplifying or neglecting certain fuel properties.

The mentioned theory from Lefebvre [27] was supported by Mellor [37], and was argued to be related to fuel penetration. The bigger the droplets, the further they penetrate the flame and stabilize the flame. He additionally correlated the scaling of the blowout towards Damköhler number, similar to premixed combustion. For the chemical timescale, he used ignition delay time with a correction factor for droplet evaporation to better predict experimental data of blowout.

Grohmann et al. [32] compared Jet-A1 to single-component fuels and investigated their behavior near lean blowout in a prefilmed atomizer. They found e.g. that n-hexane and iso-octane have similar atomization and vaporization behavior, but LBO limit of normal alkanes reached lower levels than their branched counterparts. This correlates well with other researchers' explanation, that the iso-to-normal-paraffin ratio influences the LBO limit, as well as the H/C ratio. They further compared different normal alkanes and found that n-hexane and n-dodecane have similar LBO limits at high air inlet temperatures but differ at low pre-heating temperatures. The origin of this behavior came from the production of bigger droplets in the case of n-dodecane and a lower evaporation rate, which led to an improvement of LBO (similar to Lefebvre's theory).

In general, the Lean Blowout can be connected to several timescales, which were shown by Lefebvre [27], Plee and Mellor [38] and more recently Bell et al. [39] and Heyne et al. [17]. Those can be separated into two groups: physical and chemical timescales. Physical are timescales for evaporation, atomization, and mixing, where chemical timescales are ignition delay time, extinction delay time, and reaction time. Peiffer et al. [16] compared several fuels in several combustor designs to find a correlation of property timescales towards LBO behavior by using random forest regression properties.

Their results show that the main influential fuel property on LBO can be strongly affected by the combustor. The test rigs with a pressure atomizer showed strong dependence in LBO over atomization and evaporation timescale. The Well-Stirred Reactor, which had a prevaporized injector, but also the reference rig, which had a pressure atomizer with a strong swirler, and another rig with an airblast injector, showed all a strong dependence in DCN over LBO. Test rig with prevaporized condition had also a strong dependence on extinction timescale. Peiffer additionally stated that a combustion test rig with minimal fuel atomization spray difference will be minimally sensitive to evaporation timescale.

Won et al. [40] focused on the extinction of conventional and alternative jet fuels. They derived a "combustion property target (CPT) index", which included the DCN number, hydrogen-to-carbon ratio, and the molecular mass to describe the extinction behavior of the tested fuels. The CPT was mentioned to be a potential screening tool for future alternative jet fuels, to simply determine better or worse combustion behavior compared to conventional jet fuels.

Fujiwara et al. [41] showed, that conventional Jet fuel and bioderived HEFA fuel do differ in case of combustion instability. A lean premixed prevaporized (LPP) burner was used at a pilot-main fuel ratio of 15% with an air-fuel-ratio of roughly 40. Jet-A1 combustion exhibited a combustion oscillation with a frequency of 550 Hz ($p_{peak} > 11$ kPa), where at similar condition HEFA combustion had only a minimal peak, when looking at the pressure amplitude ($p_{peak} < 1$ kPa). The reason for this difference was not explained but could originate from physical or chemical properties of tested fuels, respectively. On the contrary, Wijesinghe et al. [42] published, that HEFA fuel caused a much stronger combustion instability than Jet-A1. The published frequency was 1100 Hz, and instability could be observed in pure fuel cases as well as fuel mixtures of HEFA and Jet-A1. Again, an explanation for the difference in such an instability behavior was not given. Nevertheless, this gave amongst other things the motivation of the current study.

Chen et al. [43] researched the combustion stability of three single-component fuels compared to the reference fuel RP-3. Noticeable difference was found regarding combustion instability. For low inlet air temperatures, RP-3 and n-dodecane flame was stable and anchored at the injector. With an increase in inlet temperature, the condition for both fuels shifted towards an unstable thermo-acoustic

fluctuation. Iso-octane and methylcyclohexane always exhibit combustion oscillation, though above 403 K a mode shift in combustion fluctuation was observed. Chen explained these differences in combustion behavior might stem from a difference in global delay time. Additionally, iso-octane exhibit the lowest combustion instability amplitude, which may come from its long ignition delay time, indicating that different fuels produce different timescales, affecting the combustion instability behavior.

The impact of fuel towards combustion instability was extensively researched by Lieuwen et al. [44]. They reviewed the impact of fuel mixtures on flashback, blowout, and stability. Lieuwen published in another paper the impact of different fuels on delay time and how it influences the thermoacoustic instabilities. Different fuels can exhibit different delay times between the perturbation at the injector and the perturbation at the flame base, considering the convection time to be the most important part. Ni et al. [45] derived a mechanism for combustion instabilities via a simple numerical model for combustion instability. They concluded, that any measures, which spread out the distribution of convective or chemical-kinetic time lags in the axial direction should have a positive impact onto the combustion stability, but further said that not enough data are available in the literature to fully confirm their model. Bae et al. [46] researched the influence of total delay time of a non-premixed methane-oxygen flame in a single-element combustor. They varied the equivalence ratio as well as the combustor length and found, that by increasing the total delay time, the combustion instability mode shifted from fundamental longitudinal to third harmonic mode. They concluded that the total delay time is a good parameter to describe different combustion instabilities.

Regarding liquid fuel, analyses concerning the fuel property impact on combustion instability and delay times are rather sparse. Ruan et al. [47] showed, that the tested branched, linear and cyclic alkane behave differently compared to RP-3, regarding the instability frequency and amplitude. The unsteady flame behavior was similar, although a stronger time-lag of heat release fluctuation towards pressure fluctuation for iso-octane compared to methylcyclohexane was found when encountering similar acoustic pressure oscillation in the combustor. They speculated this behavior stems from the fuels' distinct ignition delay times.

1.5. Objective

For the use of new alternative fuels, it is of crucial importance, to understand the difference of those new fuels compared to conventional jet fuels, to avoid performance reduction or in the worst case safety issues. Only after making sure the alternative fuel's combustion performance is similar or even better, it can be a viable alternative and should be called drop-in fuel. The aim of this study therefore is, to distinguish the differences of bioderived HEFA and petroleum-based Jet-A1 fuel regarding spray and combustion performance and behavior of a dual swirl prefilm airblast injector in a non-premixed configuration at different operating conditions. The focus will be taken on the influence of physical properties of those fuels on static and dynamic combustion stability.

The objective of this work is separated into the following points:

1) Measuring the evaporation rate of HEFA and Jet-A1, provided by the JAXA Research Laboratory Chofu by single droplet measurements in a drop tower facility to verify a difference in evaporation timescale between the two fuels
2) Measuring the initial droplet size produced by the dual swirl prefilm airblast injector for HEFA and Jet-A1, to analyze the impact of both fuels' physical properties onto the atomization process. According to literature, this has not been done in this kind of configuration for those fuels yet. Therefore, an appropriate combustion chamber needs to be designed and manufactured, as well as a suitable droplet size measurement system needs to be set up.
3) Determine the difference in lean limit for HEFA and Jet-A1 at ambient condition as well as high temperature and high-pressure condition, to elucidate the difference in LBO quantitatively for the used configuration and to see if a difference in condition influences the LBO limit
4) Analyze flame positioning and flame moving near the lean limit combustion of each condition, to determine a difference or possible influence of chemical and/or physical property difference between the two fuels
5) Analyze pressure data near lean blowout, to identify possible combustion instability. Conduct simultaneous measurement of spray by Mie scattering and heat release rate by

CH*chemiluminescence, to determine the relationship between the collected signals, as well as describe the possible difference between HEFA and Jet-A1 in fluctuation behavior

6) Correlate the above measurements with each other for describing the lean limit by timescales derived from the fuels' physical or chemical properties

Objective 1) and 2) will be focused on in Chapter 2, which also describes the fuel properties and the setup of the used experiments to fulfill those objectives. Chapter 3 pays attention to objectives 3) to 6). Chapter 3 also includes the main experimental setups used at ambient condition as well as high temperature and high-pressure condition. Both chapters discuss their handled objectives and Chapter 4 sums all results conclusively.

Chapter 2. Droplet measurement of HEFA and Jet-A1 in a double-swirl airblast injector

2.1. Introduction

2.1.1. Spray quality measurement

As stated in Chapter 1, the main function of an injector is to transform the incoming liquid into droplets. The goal of most injection systems is not only to produce a controllable or at least predictable droplet size but also to discharge those droplets into the surrounding atmosphere as a symmetrical spray. This is of utmost importance, otherwise the produced droplets may negatively influence the system. There are several values to be calculated to describe the quality of a spray, e.g. Sauter Mean Diameter (SMD), Volume Median Diameter (VMD), and Mass Median Diameter (MMD), when it comes to the droplet size distribution, but also values like spray cone angle, penetration and patternation are important to describe the spray formation and area where the spray is acting. Regarding this work's analysis, the focus will be taken onto SMD. It can be calculated with

$$D_{SMD} = d_{32} = \frac{\sum_{i=1}^{N} h_i \, d_i^3}{\sum_{i=1}^{N} h_i \, d_i^2} \qquad (3)$$

where h_i and d_i are the number of the same droplet size and the droplet size, respectively. SMD represents the volume to surface ratio and is a good indicator of the droplet size distribution of a spray, especially in fields like combustion, where the active surface is important.

As mentioned earlier, the atomization process can be strongly influenced by the physical properties of the liquid, although airblast injectors are typically influenced by those properties only to a certain limit. Nevertheless, Grohmann et al. [32] used a hybrid pressure swirl airblast injector and showed similarities in their SMD measurements between Jet-A1 and n-dodecane and differences towards iso-octane and n-heptane. Shin et al. [48] tested in a similar injector as Grohmann Jet-A1 and four different alternative jet fuels. No clear characteristics could be concluded from their results. Burger [49] also used a pressure swirl airblast injector in hybrid form and found a difference in SMD between the 16 tested fuels in his study. Tareq et al. [50] used a dual swirl airblast injector with prefilmer

similar as in the present study and found a strong difference between Jet-A1 and water. Sivakumar et al. [51] tested Jet-A1 and several Camelina HEFA/Jet-A1 blends and concluded that those fuels have an insignificant difference in SMD.

Due to the somehow contradicting results of the mentioned publications, a lack of comparison between Jet-A1 and a tallow HEFA fuel exist and because the atomizer used in this study is self-made, it is necessary to investigate its spray producing characteristics, and also to identify the possible difference between the two tested fuels. Reason for the importance to find out rather or not there is a difference in droplet size between the two tested fuels lies in a resulting difference in evaporation time, which will be discussed in the next section.

2.1.2. Droplet evaporation

After a cloud of droplets (spray) is produced, the next step in liquid combustion is the vaporization or evaporation of the fuel droplets. Evaporation is described as the evaporation or burning rate of a fuel droplet. Generally, it is assumed, that the evaporation rate depends only on fuel properties, but Nakaya et al. [52] described, that the rate can be influenced by the initial droplet diameter, too. A similar explanation was given by Liu et al. [53], where he showed that the evaporation rate dependency can be separated into three regimes regarding droplet sizes. The first regime was stated to have an evaporation rate independent of droplet size, which is valid for droplet sizes usually produced by jet engine injectors. Therefore, it is assumed, that the influence of droplet size on the evaporation rate is neglectable small and omitted in this chapter's calculation.

An injector creates, depending on its atomizing quality, a monodisperse spray (wide or narrow range also depends on its quality or rather the purpose of its existence). The produced spray, or droplet size spectrum, is usually described with a mean diameter, which is in technical terms often the Sauter mean diameter (SMD), as described in the previous section.

When droplets pass through a hot environment, but also at room temperature, heat exchange between the liquid surface of the droplet and the surrounding happens, causing the droplet to slowly

vaporize and turning part of its liquid into vapor which mixes with the surrounding gas after a certain heat up time. This reduces the droplet sizes until the droplet is fully evaporated. The time from starting this process to finishing is called the evaporation time. In combustion, but also in droplet drying and other fields, it is important to know or at least be able to accurately assume this time to optimize systems. Especially in combustion systems, engineers want to keep the evaporation time as short as possible, so the vaporized fuel mixes fast with the injected or surrounding air and create a burnable mixture.

Wood et al. [54] was one of the first researcher, who gave an experimental proof for the evaporation behavior of a single droplet. For better visualization, results of one conducted evaporation experiment of this study are presented in advance in Figure 10. Clearly visible is the unsteady change in the early stages of the droplet, which then moves on to a steady or quasi-steady change of the square of the droplet size over time. It is assumed, that at the beginning, the droplet goes through a heat-up process, where most of the incoming heat from the surrounding atmosphere is used to bring the droplet up to its boiling temperature and when reached, the droplet transits into the visible steady state condition and evaporates. As mentioned before, the early part is known as heat-up time. At the beginning of the heat-up time, the droplet core is much cooler than the surface temperature, but literature [55][56][57] showed theoretically and experimentally, that the droplet exhibits an internal recirculation, which basically supports heat and mass transfer and accelerates temperature adaption. As mentioned, when the droplet then reaches nearly equal temperature or rather a certain threshold, most of the incoming heat is used to evaporate the liquid, which happens in a steady/equilibrium state.

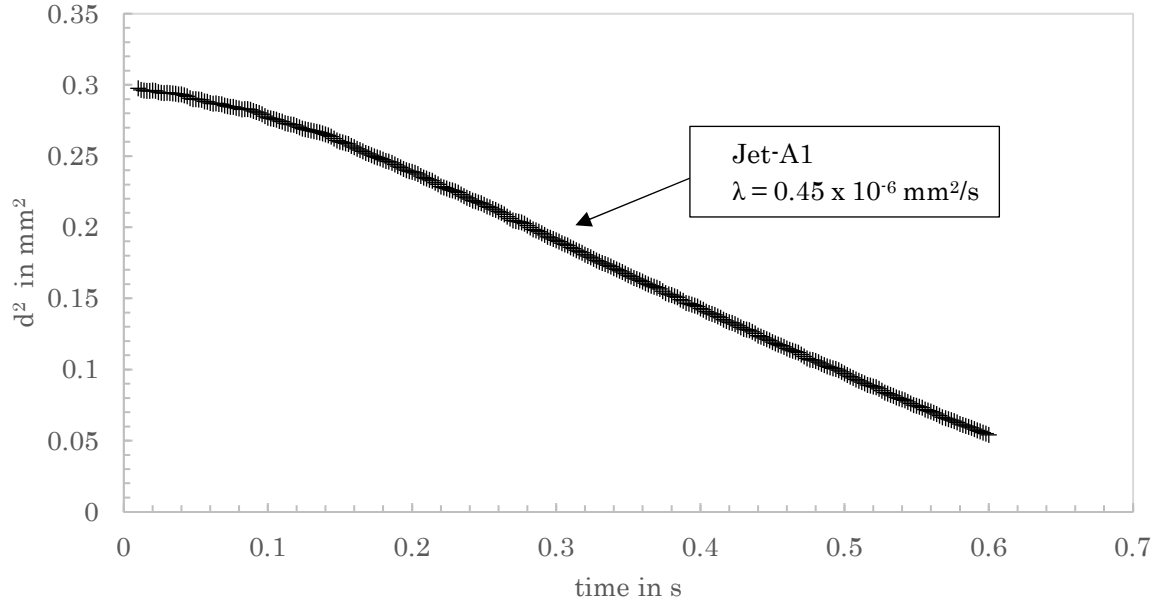

Figure 10: example of single droplet evaporation

Godsave [58] derived the well-known D2 – law, shown in equation (4), which describes the mentioned quasi-steady change of droplet diameter squared over time.

$$D_0{}^2 - D^2 = \lambda t \qquad (4)$$

In the equation, λ describes the evaporation rate, D the droplet diameter changing over time and D_0 the initial droplet diameter. In that law, the heat-up period is not included, therefore D_0 is actually the droplet diameter at the end of the heat-up time. Followed by Spalding [59], a simple droplet evaporation model was derived, which includes the heat and mass transfer between droplet and surrounding atmosphere. Detailed definition can be found in literature [10][6][5]. For this study, most important are equations (5) and (6)

$$\lambda = \frac{8\frac{k_g}{c_p}}{\rho_l} ln(1+B) \qquad (5)$$

$$B = \frac{c_p(T_\infty - T_B)}{h_{fg}} \qquad (6)$$

where k_g, c_p, ρ_l are the heat conductivity, specific heat capacity and liquid density, respectively. B is the transfer number (or sometimes called Spalding number) and can be calculate with specific heat capacity, the temperature difference between atmospheric temperature and the droplet boiling point temperature and the latent heat of vaporization h_{fg}.

As mentioned, the unsteady area of the droplet evaporation is the heat-up period. Chin and Lefebvre [60] did a wide range of droplet analysis, showing that the heat-up period can in certain conditions make the majority of the total evaporation time. Lefebvre [10] empirically described the heat-up time with the following equation.

$$\Delta t_{hu} = \frac{c_{pF}\rho_F c_{pg} {D_{hu}}^2 (T_{Sst} - T_{S0})}{12\, k_g ln(1 + B_M) L \left(\frac{B_T}{B_M} - 1\right)} \qquad (7)$$

Where c_{pF}, T_{Sst}, T_{S0}, D_{hu} are the specific heat capacity of the fuel, the surface temperature at steady state, the initial surface temperature, and the heat-up diameter, respectively. B_M and B_L are the mass and heat transfer numbers, respectively. The heat-up droplet can be calculated with

$$D_{hu} = D_0 \left(1 + \frac{c_{pF}\,(T_{Sst} - T_{S0})}{2L\left(\frac{B_T}{B_M} - 1\right)}\right)^{-0.5} \qquad (8)$$

which is the droplet diameter, after the heat-up period finished. With this the total evaporation time can be written as

$$t_{evaporation} = \Delta t_{hu} + \Delta t_{st} \qquad (9)$$

Δt_{st} represents the time passed during the quasi-steady state condition and can be calculated with equation (4). By dividing the square of the initial droplet with the evaporation time, the effective evaporation rate of a droplet can be assumed. The above equations show that different chemical and physical properties can lead to different evaporation rates and therefore evaporation times. This can lead to unwanted delays within the combustion process, affecting or even inducing combustion

instabilities. Therefore, it is of importance to measure the evaporation rate of Jet-A1 and HEFA of this study.

2.2. Material and Methodology

2.2.1. Fuel Properties

The current study compares two important fuels used in avionics, a conventional petroleum-derived fuel: Jet-A1, and an alternative bioderived fuel: HEFA. As mentioned in the introduction, HEFA (Hydroprocessed Esters and Fatty Acids) are the most established biofuels in aeronautics and are allowed to be used in a 50:50 blend with conventional jet fuels. The fuels were supplied by JAXA (Japanese Aerospace Exploration Agency) and Table 1 gives an overview of both fuels, which were used in several previous publications already ([41][61][62][63]). The two fuels show several differences in their properties. Differences in viscosity, surface tension and density might be affecting the atomization process. Distillation curve shows, that HEFA has a slightly lower boiling point at the start, but a bit higher final boiling point temperature than Jet-A1, which might induce a difference in evaporation rate. A difference of hydrogen to carbon ratio can be seen, which is an indication for higher combustibility/reactivity of HEFA. Nevertheless, the strongest difference shows the aromatic content, where HEFA has basically no aromatics and Jet-A1 consists of almost 20 vol%. This comes most likely from additives for freezing point reduction, for reduced aging and because of swelling performance towards sealing materials.

Table 1: Fuel properties of used jet fuels [61]

Properties	**HEFA**	**D7566**	**Jet-A1**	**D7566**	**Test method**
Freezing point [°C]	-58.5	< -40	-48.0	<-47	JIS K 2276
Kinematic viscosity [mm²/s] @15°C	1.963	N/A	1.655	<8 (-20deg C)	JIS K2283
Surface tension [mN/m]	22.5	N/A	23.6	N/A	JIS K 2241
Density [g/cm³] @15°C	0.7554	0.73-0.77	0.7886	0.775-0.840	JIS K 2249-1
Net heat of combustion [MJ/kg]	44.14	N/A	43.38	>42.8	JIS K 2279
Physical Distillation					
Initial boiling point [°C]	146.5	N/A	148.5	N/A	
10% recovered temp. [°C]	165.0	<205	164.5	<205	JIS K 2254
50% recovered temp. [°C]	208.0	Report	193.5	Report	
90% recovered temp. [°C]	253.5	Report	237.5	Report	
Final boiling point [°C]	269.0	<300	259.0	<300	
Lubricity [mm]	1.04	N/A	0.83	<0.85	ASTM D5001
Carbon [mass %]	84.7	N/A	86.1	N/A	JPI-5S-65
Hydrogen [mass %]	15.2	N/A	13.8	N/A	
Sulfur [mass %]	<0.0001	<0.0015	0.0006	<0.3	JIS K 2541-6
Composition					
Paraffin [vol. %]	98.4	Report	79.1	N/A	ASTM D1319
Olefin [vol. %]	0.9	N/A	3.0	N/A	
Total aromatics [vol. %]	0.7	N/A	17.9	8-25	
Aromatics					
Benzenes [vol. %]	<0.1	N/A	19.1	N/A	
[mass. %]	<0.1	N/A	21.3	N/A	
Naphthalene [vol. %]	<0.1	N/A	0.1	N/A	ASTM D6379
[mass. %]	<0.1	N/A	0.2	N/A	
Total aromatics [vol. %]	<0.1	N/A	19.2	8.4-26.5	
[mass. %]	0.1	N/A	21.5	N/A	

2.2.1. Injector

The injector used for this study was an in-house injector, based on a Parker Hannifin design, developed in a previous study [64]. Developed was a double swirl prefilming airblast injector as described in Chapter 1 and shown in Figure 11.

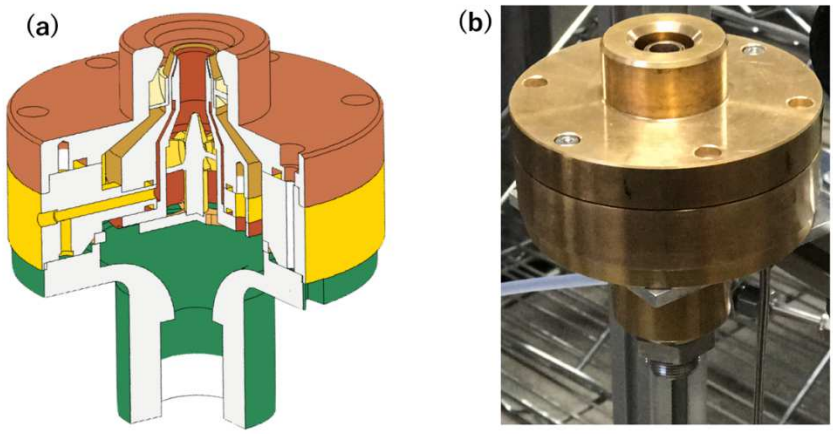

Figure 11: double swirl prefilming airblast injector; a) cut 3D-design, b) photography

An outer swirl (OSW) and an inner swirl (ISW) creating counter flowing airstreams, which disrupts the liquid fuel entering between the two airstreams. A schematic of this is visible in Figure 12. Also shown is a small swirl in the fuel path. This creates a swirling movement onto the fuel which has the effect to push the liquid outward, towards the outer wall and emphasis the following atomization process at the edge of the outer wall. The schematics do not show the reduction in the outer diameter of the inner swirl, which shrinks to a diameter of 9 mm. Therefore, it is possible to have an outer diameter of the inner swirl and an inner diameter of the outer swirl with the same diameter. Different swirlers were designed at first, to change the flow field inside the combustor and see the influence onto lean blowout. Nevertheless, the focus of this study was on one pair of inner and outer swirl. For the manufacturing of these swirlers, a 4-axis processing machine (MODELA MDX – 540) was used.

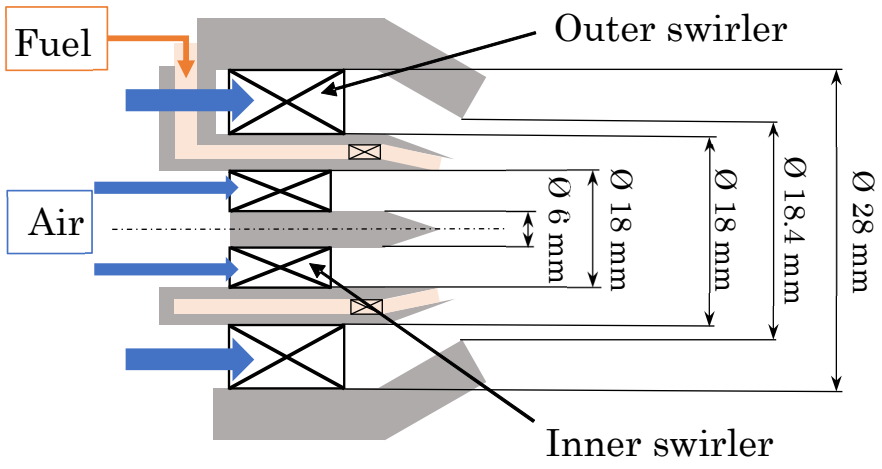

Figure 12: schematics of the dual swirl prefilming airblast injector

Calculation of Swirl Number:

The swirl number S, a dimensionless number based on geometrical parameters, was used for the valuation of the different swirlers. It was defined by Beer and Chigier [65] with the following equation:

$$S = \frac{G_\varphi}{G_x R} \qquad (10)$$

Where G_φ and G_x are the axial flux of swirl momentum and the axial flux of axial momentum, respectively. R represents the exit radius of the injector nozzle.

$$G_\varphi = \int_0^R (Wr)\rho U 2\pi r \, \mathrm{d}r = \text{const} \qquad (11)$$

$$G_x = \int_0^R U\rho U 2\pi r \, \mathrm{d}r + \int_0^R p 2\pi r \, \mathrm{d}r = \text{const} \qquad (12)$$

W and U are the velocity component in the azimuthal and axial direction, respectively and p is the pressure in the radial direction. Beer and Chigier assumed, that the pressure does not change in radial direction within the radius of the nozzle exit, therefore the second part of the right-hand side of

equation (12) can be omitted. Considering thin enough blades for the swirler in Figure 11b, constant axial velocity along the blades, and a constant blade angle, equation (11) and (12) become:

$$G_\varphi = 2\pi\rho U_0^2 \tan\alpha \frac{Ro^3 - R_i^3}{3} \quad (13)$$

$$G_x = \pi\rho U_0^2 (R_o^2 - R_i^2) \quad (14)$$

Putting the newly derived versions of axial fluxes into equation (10), the geometric dependence of swirl number is

$$S = \frac{2}{3}\left[\frac{1-(R_i/R_o)^3}{1-(R_i/R_o)^2}\right]\tan\alpha \quad (15)$$

with R_i and R_o denoting the inner and outer radius of the swirl blades.

Beer and Chigier did not consider the operation of dual swirl, as well as the cross-section reduction (venturi design) near the exit visible in Figure 12. In fact, several studies imply, that the assumed swirl number is often much higher than the measured one, derived from velocity measurements [66]. For that reason, we follow a slightly different path, proposed by Sivaseagaram [67].

$$S_{total} = (\dot{m}_o S_o \frac{D_{e\_o}}{D_{o\_o}} + \dot{m}_i S_i \frac{D_{e\_i}}{D_{o\_i}}) \frac{1}{(\dot{m}_o + \dot{m}_i)} \quad (16)$$

With D_{e_o} and D_{o_o} being the smallest diameter on the outer swirler path and the outer diameter of the outer swirler, respectively, and D_{e_i} and D_{o_i} being the smallest diameter on the inner swirler path and the outer diameter of the inner swirler, respectively. S_o and S_i are the swirl number of outer and inner swirler by using equation (15). Mass flow rates with the subscript o and i, denote the outer and inner mass flow rate, respectively. Table 2 shows the calculated swirl numbers for the manufactured inner and outer swirler and their resulting swirl number when used in the in-house injector.

Table 2: Overview of swirl number

Blade angle outer swirler	S_o	S_i	S_{total}
45°	0.83	-1.27	0.13
60°	1.44	-1.27	0.39
64°	1.70	-1.27	0.51

2.2.2. Interferometric Laser Imaging of Droplet Size (ILIDS)

To evaluate a spray, the droplet size and droplet distribution of the produced particle is necessary to be measured. Particle Doppler Anemometry (PDA) is one of several techniques to realize that. This system though is cost intense, needs a rather "unusual" setup, which demands visualization from three directions (often separated in 120° rotational angle). A "typical" setup to observe spray or CH*chemiluminescence is usually designed with a slit for a laser sheet and a window for the observation, which are arranged at a 90° angle. Interferometric Laser Imaging of Droplet Sizing (ILIDS) or also called Interference Pattern Interferometry (IPI) is able to work under such an arranged angle. The system itself was developed by König et al. [68]. They found, that when laser light passes through a liquid droplet, this droplet creates a diffraction pattern that changes depending on the rotational angle towards the laser light. This technique was further developed by Glover et al. [69] and Maeda et al. [70]. Previously it was believed, that ILIDS works only correctly at a scattering angle of $20° < \theta < 70°$, but Ragucci et al. [71] and Pu [72] established a usage of the ILIDS with a 90° scattering angle. As shown in Figure 13, when laser light passes through a droplet, the reflected and first refracted laser beam create an interference pattern, which can be collected with a lens to project it on a camera sensor, if the sensor is out of focus towards the collecting lens. If the camera is moved to the focal point, the interference pattern gets reduced to glare points, where the distance between the two points correlate with the droplet size. The interference pattern or also interferometric fringe has a geometric correlation to the droplet size, where an increase number of stripes mean a bigger droplet. The correlation is represented with the following equation:

$$d_p = \frac{2\lambda N}{\alpha}\left(\cos\left(\frac{\theta}{2}\right) + \frac{m\sin\left(\frac{\theta}{2}\right)}{\sqrt{m^2 - 2m\cos\left(\frac{\theta}{2}\right) + 1}}\right)^{-1} \qquad (17)$$

where d_p is the droplet diameter, λ, N, α, m and θ are the wavelength of the laser light, the number of stripes, collecting angle, relative refracting index between droplet and surrounding gas, and the refracting angle, respectively.

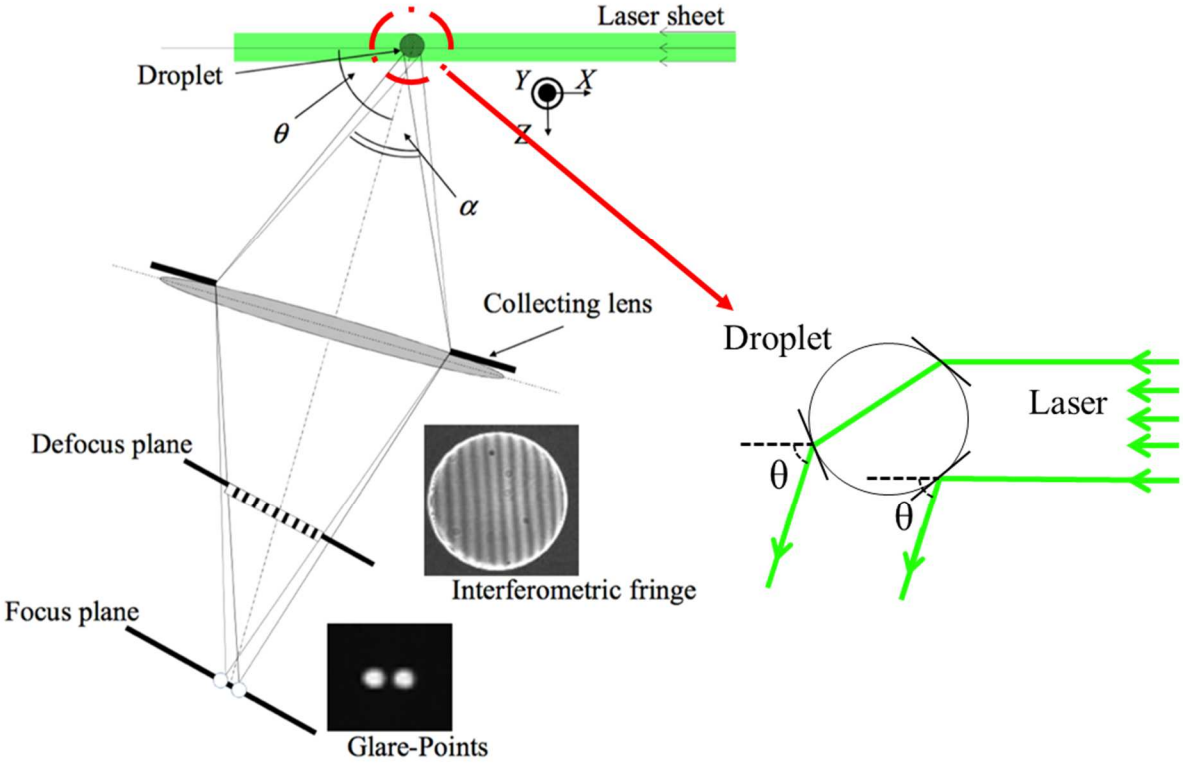

Figure 13: functional principle of ILIDS (image based on [143][70]*)*

One important advantage of ILIDS is its independence of droplet size measurement over light intensity, therefore it does not need to be calibrated and absolute measurement of the droplet size is possible by only knowing the number of stripes N. For validation, Pu [72] experimentally showed with the droplet size parameter (18), derived by Van de Hulst [73]

$$\chi_p = \frac{\pi d_p}{\lambda} > 10 \qquad (18)$$

, that the geometric approximation is in good agreement with the exact Lorentz-Mie solution down to a droplet size of 2 µm. The 2 µm for droplet size corresponds roughly to laser light with a wavelength of 532 nm (green light laser).

Maeda's improvement for the ILIDS system was important concerning dense sprays. Figure 14B shows, as soon as several droplets are in a limited area, the fringe pattern of each droplet would overlap, causing non-recognizable fringes and therefore no droplet measurement anymore. To counteract such overlapping, Maeda added cylindrical lenses, which reduced the vertical dimension, shrinking the droplet to a rectangular or even as thin as a line. Figure 14 shows the difference with and without

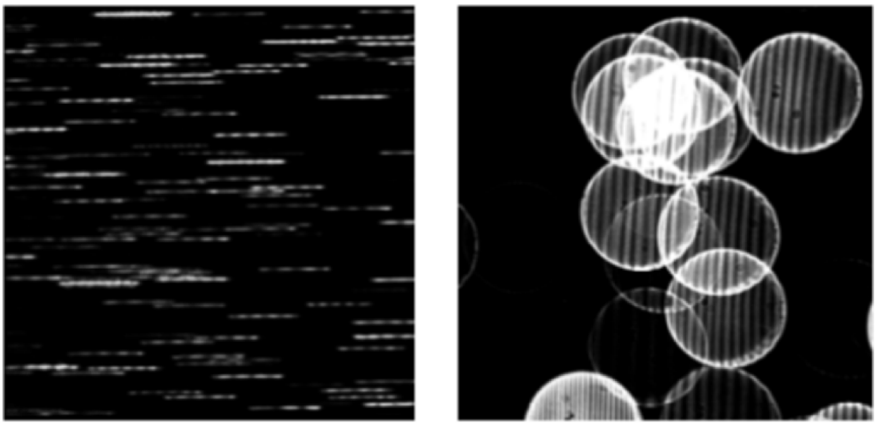

Figure 14: a) with cylindrical lenses; b) without cylindrical lenses [91] *(permission from publisher to reuse)*

cylindrical lenses. Those lenses do not only reduce the fringe pattern of each droplet to avoid overlapping, but also merge the intensity along the stripes to increase the signal-to-noise ratio. Figure 15 shows the schematic setup of ILIDS analysis at ambient condition. A Nd:YAG Laser (Changchun New Industries) with 532 nm green laser light and two cylindrical lenses (CLB-3030-300NM and CLB-3-3—1000PM) were used to create an approximately 1 mm thick laser sheet. The laser sheet passed through a slit in a newly designed combustion chamber (Figure 17) to illuminate the droplets and ultimately create the fringe pattern to measure the produced droplets of the injector. For collecting the ILIDS projections, a Nikon lens (Nikkor, f85) was used, as well as two cylindrical lenses (CLB-3030-80N and CLB-3030-70P) were employed to reduce the circle fringe pattern into slits as described by Maeda et al. [70]. A high-speed camera (Phantom V2511) recorded the fringe slits with a framerate of 10000 fps and an exposure time of 5 μs, to have clear images of the droplet fringe pattern for processing and calculating the droplet size. To avoid interference from the surrounding, especially

random reflections of the laser light, the ILIDS system was enveloped with a black cover. In a previous study (Salman et al. [74]), this system was used to confirm the evaporation rate during spray combustion, by tracking and tracing single droplets within the spray. Similar evaporation rates for n-Dodecane were reached compared to single droplet evaporation tests at lower ambient temperatures, but the lower evaporation rates of the researched jet fuels did not allow to have a similar result. Due to the swirling movement onto the droplets, tracing over the full height of the observation area was impossible, and the change in droplet size was not sufficient enough, to conclude a valid evaporation rate (more details in [75]).

Figure 16 shows the detailed schematics of the ILIDS with distances. The width of the collecting lens and the distance to the laser sheet determine the collecting angle α, which is in the shown formation 21°. Therefore, with the above-mentioned parameters, one stripe in the fringe pattern corresponds to

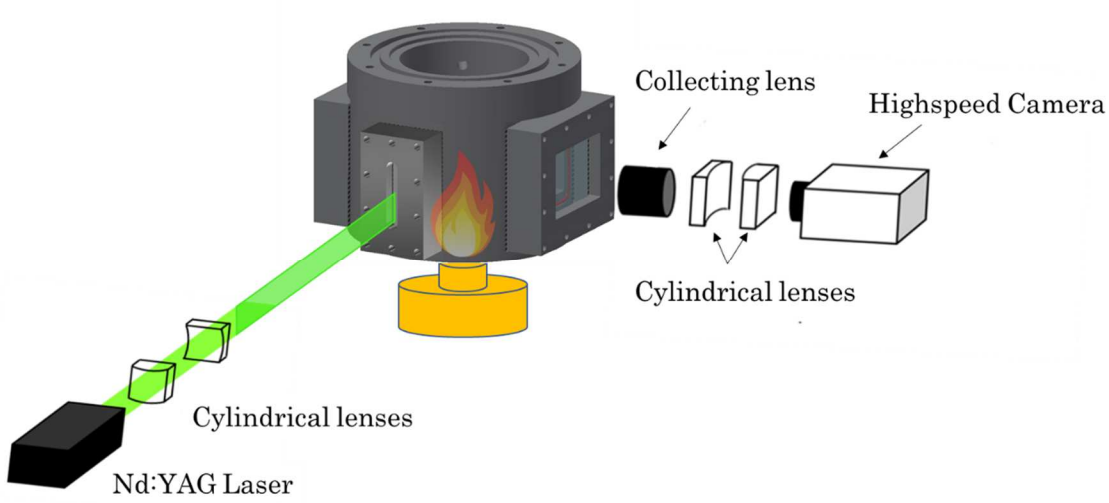

Figure 15: Schematics of ILIDS system used in this study

1.7 µm at a refractive index of n_{jet} = 1.45 (source [76]). Hydrocarbons like jet fuels only slightly vary in refractive index, and a theoretical change of ±0.05, would lead to a droplet size change of -0.015% and +0.078%, respectively, therefore a neglectable difference between Jet-A1 and HEFA can be assumed. According to Pu [72], the theoretical minimum and maximum droplet size measurable of this system would be 3.4 µm and 170.4 µm, respectively.

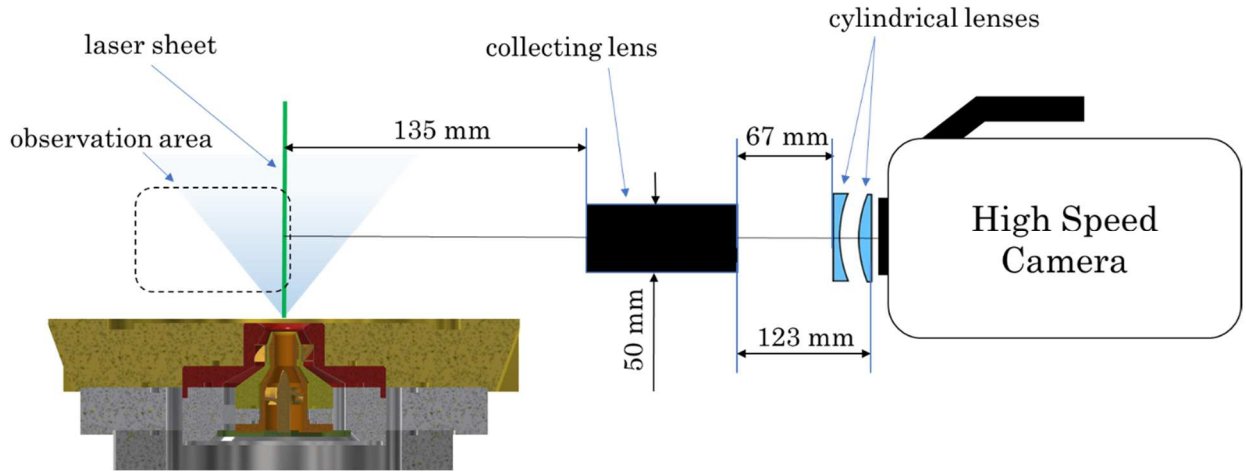

Figure 16: detailed arrangement of ILIDS setup towards laser sheet and injector

Droplet measurement of the injector will be conducted over a wide range of air flow rates, to determine an SMD quality curve, which describes the atomization performance of the injector. It will be analyzed if the resulting SMD can be predicted via existing empirical equations in the discussion section. Additionally, each air flow rate was tested with different outer swirler of the injector, to additionally show the influence of swirling flow onto the atomization result.

2.2.3. Development of a combustion chamber for droplet size measurement

To observe the droplets and measure droplet size by using the system described in the previous subsection, a new combustion chamber was necessary, which enables visual access to the inside of the combustion chamber and consequently to the spray. Additionally, since another combustion chamber already existed, the new chamber needed a flanch design, to synergize with old parts. Another important point that needed to be considered in the design was the handling of laser systems and the resulting light distortion. Therefore, the accessing windows to the inside of the combustion chamber needed to be flat. Round glass bends the light and would change the images of the fringe pattern to such an extent, that clear images of the fringes would not be guaranteed. The chamber was designed to withstand high experimental pressure of up to 1 MPa. Although for this thesis' experiments, the

maximum pressure was at about 0.5 MPa absolute pressure and temperatures reached up to 2000 K, the chamber was additionally planned to be used for rocket combustion tests as well, which can reach conditions of 1 MPa and 2400 K or more. Therefore, the heat transfer and force onto the chamber was simulated in Creo 7 (developed by PTC). Especially, the temperature near the sealing for the window fixation of the chamber was an issue, which needed special attention. For the sealing, o-rings were used, which could withstand typically 493 K, hence this needed to be considered around the o-ring grooves during the design stage, to not exceed this temperature limit. Moreover, the frame for the glass windows needed to be designed, so that the pressure onto the glass distributes equally to not cause any crack onto the glass, which may lead to safety issues or damage to expensive equipment, such as high-speed cameras. Quartz glass was chosen as material with a 20 mm thickness since this material is generally used in scientific experiments. It keeps the light spectra of the flames modulate free, but also its stronger thermal stability compared to normal glass is one of the reasons quartz glass is the right material. Figure 17 shows the newly designed combustion chamber with glass windows, window frames and necessary sealings. Additionally, to the o-rings, the window areas are equipped with high-temperature gaskets, made of carbon. All metal parts are made of stainless steel. The inner diameter of the chamber was 100 mm, to fit with already existing parts, and the length was chosen so that the complete assembly with nozzle does not change the longitudinal frequency of the combustion chamber. For supplementary pressure measurements, the combustion chamber was equipped with several threads to accommodate different high-frequency sampling pressure sensors (Kyowa, Kistler). Kistler pressure sensors are water-cooled, therefore the design needed to be adapted to have enough space for the cooling pipes. In this configuration, the hydrogen igniter for high temperature and high-pressure experiments was also supplied through the combustion chamber. The hole for that is not visible in the schematics. The construction plans of the chamber and other additional parts can be found in the appendix of this thesis.

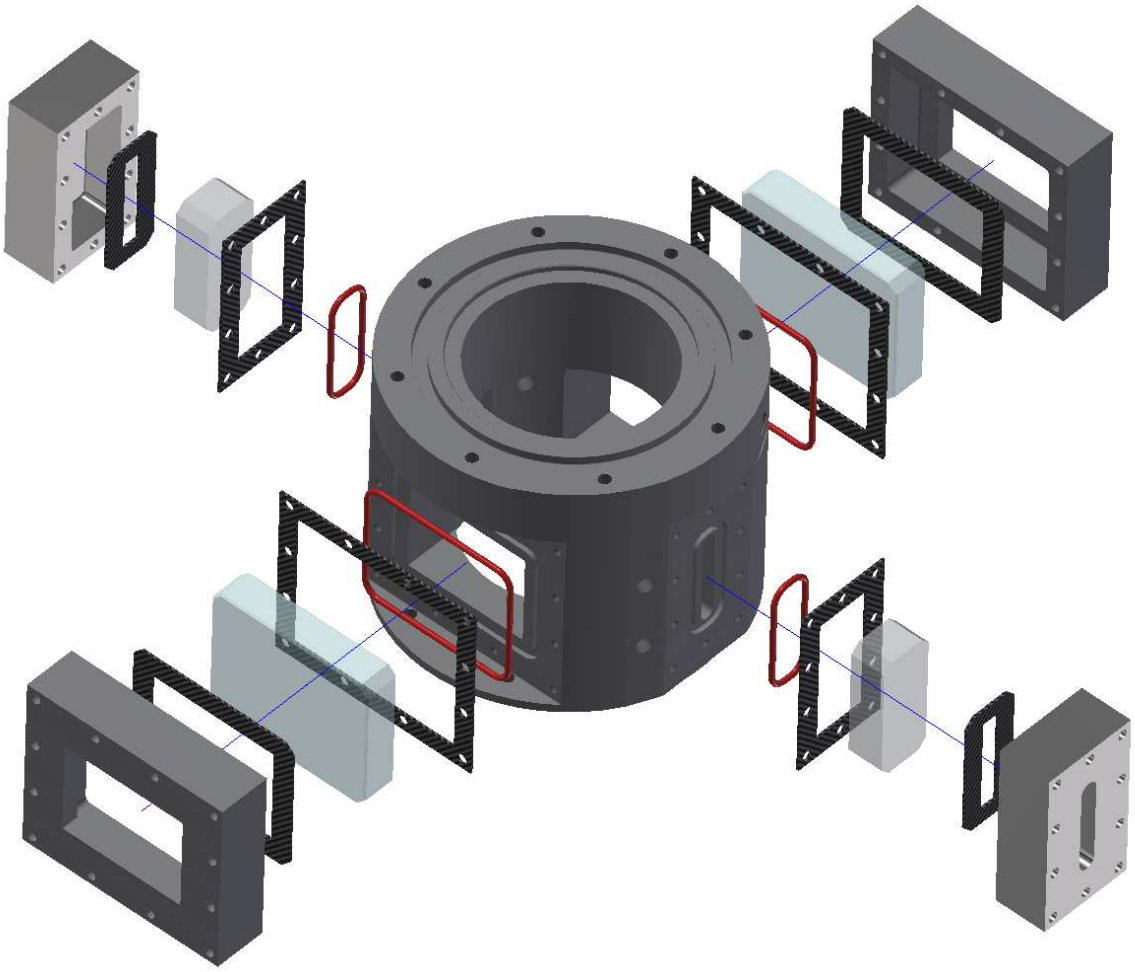

Figure 17: explosion drawing of the combustion chamber for ILIDS measurement

2.2.4. Single droplet measurement

Single droplet combustion was conducted at gravity and microgravity conditions. To realize those conditions, a drop package (Figure 18) was used, in which a droplet of researched fuel was suspended on a quartz fiber. The suspended droplet was then moved into the electrically heated chamber, which was regulated to 1023 K. The droplet self-ignited after a certain heat up time in the case of oxygen-mix as surrounding gas. From the moment of moving until finished burning, the change in droplet diameter was observed via backlight imaging with a high-speed camera (Photron, FASTCAM MH4-10 K) at 500 fps with a Nikkor lens (Nikon, Nikkor, 135 mm) and an extension tube (Nikon, PB-6); and a video camera (Sony, α-6500), for color observation at 120 fps. In the case of microgravity condition, the moving of the droplet into the furnace was synchronized with letting the whole package fall down a drop tower, which was 10 m in height.

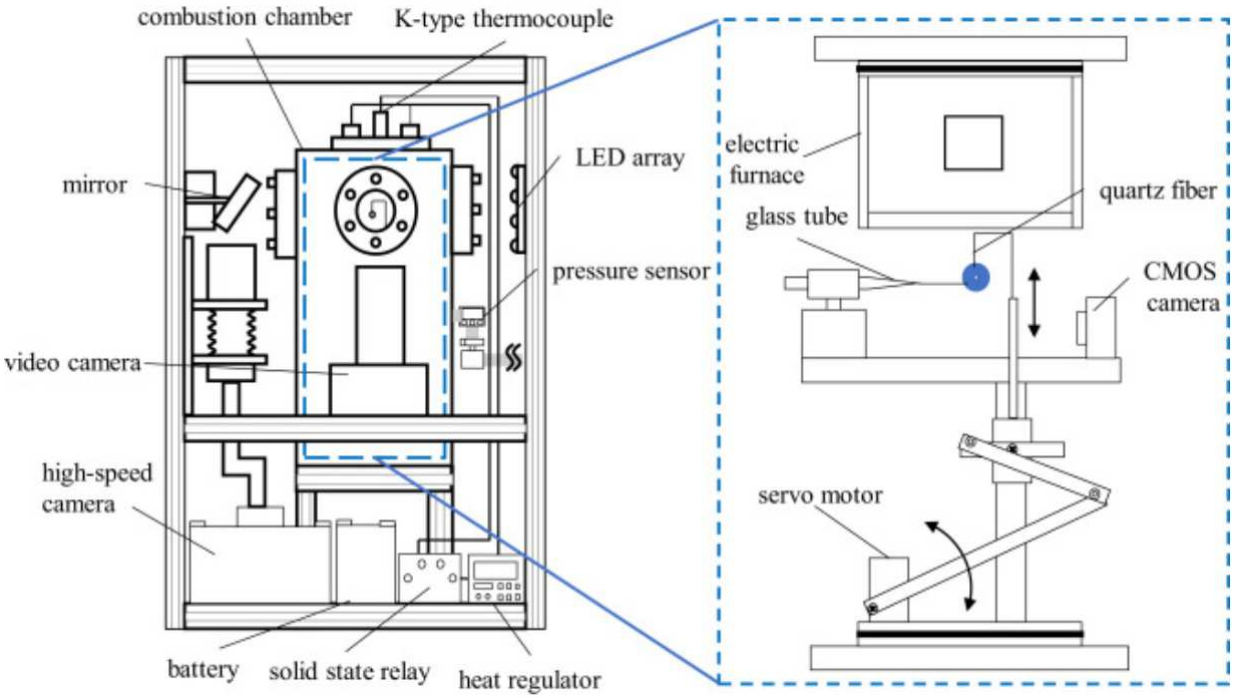

Figure 18: Schematic of the drop package with closed schematics of combustion chamber [77]

This height guarantees to maintain a microgravity condition of 10^{-4} G for 1.4 s. The pressure inside the furnace was measured with a pressure transducer (Keyence, AP-C33) and kept at atmospheric pressure of 0.1 MPa. The images of the droplets were processed to detect the droplet edge and remove

the suspender from the images. By collecting the droplet size of each image over time, process and extract the diameter of the droplets, the D2-law (equation (4)) and so the evaporation rate of the droplets could be derived. For more details about the measurement technique, it is here referred to the publication of Ando et al. [77]. Two atmospheric conditions were chosen to conduct the droplet evaporation experiments: 1) a mix of 21% O_2, 19% N_2, and 60% CO_2 for burning rate experiments during single droplet combustion and 2) 100% N_2 atmosphere, to remove soot production and focus on evaporation rate only. The CO_2 in the case of combustion was used, to reduce the generation of soot which interfered with the droplet size measurement.

2.3. Results

2.3.1. Droplet measurement of a double-swirl airblast injector

As described above, ILIDS was used to measure the droplet size at different air flow rates to calculate the Sauter Mean Diameter (SMD) from those experimental results to derive the atomization curve over the air flow rate of the used injector. First, the droplet size was measured for cold flow (no combustion) at air flow rates of 14.9, 18.6, 22.6, 29.7 g/s for the three outer swirler 45, 60, and 64°. Figure 19 shows an example of ILIDS fringes and their transformation to droplet size distribution. Each condition was repeated at least three times, to have sufficient repeatability of the measured result. With equation (3), the SMD of the observed droplet sizes for each case can be calculated. The

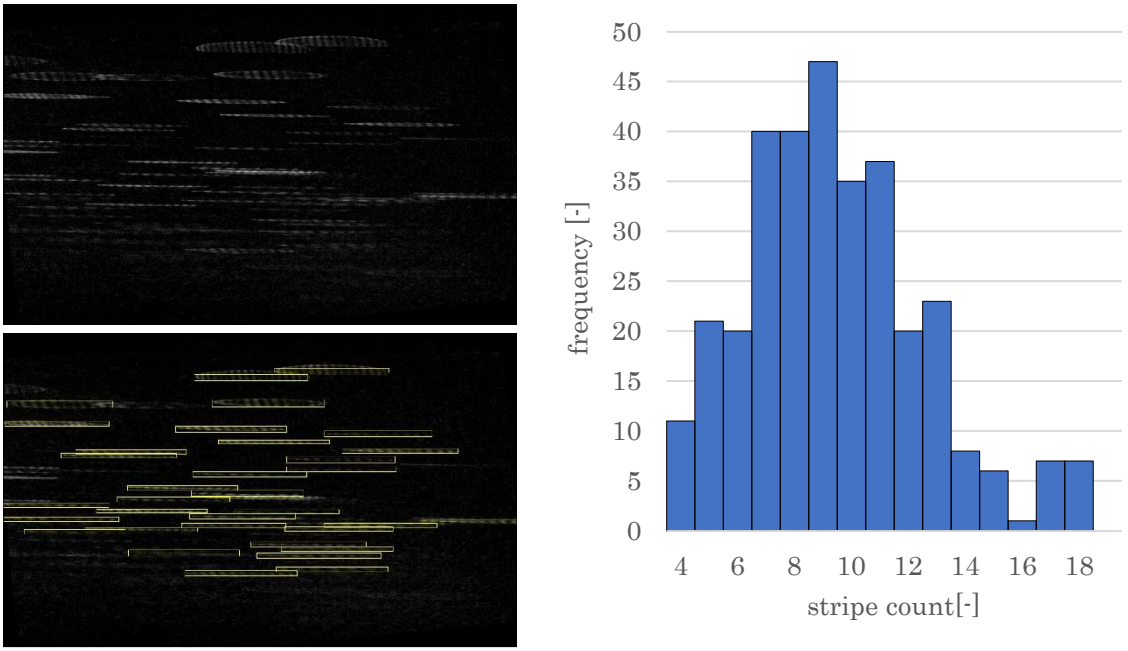

Figure 19: a) example of ILIDS fringe b) selection of fringes; c) distribution of observed droplet sizes

mean value and weighted standard deviation (which represents the error bars) of those calculated SMD are then derived by equations (19) and (20). The weight was chosen to be the number of measured droplets in each experiment. The derived mean values and error bars are collected in Figure 20.

$$\bar{d}^* = \frac{\sum_{i=1}^{N} w_i D_{SMDi}}{\sum_{i=1}^{N} w_i} \qquad (19)$$

$$\sigma^* = \sqrt{\frac{\sum_{i=1}^{N} w_i \left(D_{SMDi} - \bar{d}^*\right)^2}{\frac{(N-1)}{N} \sum_{i=1}^{N} w_i}} \qquad (20)$$

N, w_i, D_{SMDi} are the number of experiments, the weight (number of measured droplets at specific experiment), and the SMD at i^{th} experiment, respectively. $\bar{d}^*$ and σ^* are the weighted average SMD and the weighted standard derivation, respectively.

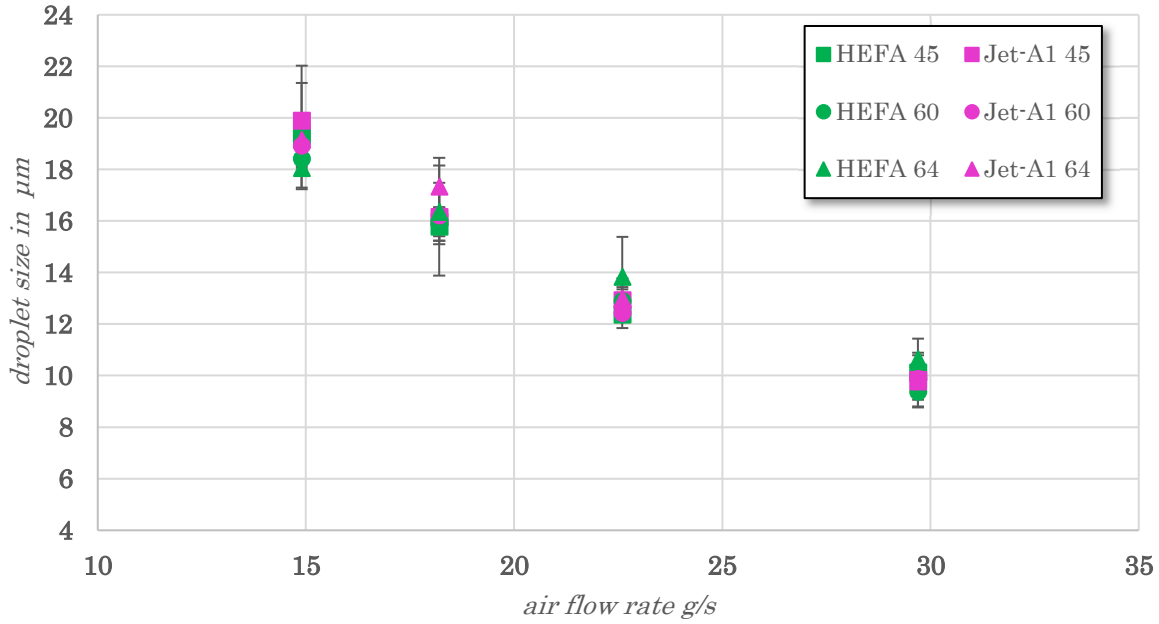

Figure 20: SMD over air flow rate for Jet-A1 and HEFA at different OSW

The results reveal, that the SMD does not show a clear tendency with the swirl number nor with the fuel type. To further elucidate that, air flow conditions of 14.9 and 29.7 g/s are enlarged and shown in Figure 21. To see a clear contrast, the results are put next to each other for different swirler and fuels. Although HEFA cases show a bit lower mean value at low air flow rates, this is reversed at high air flow rates. Though, a higher swirl number causes a stronger shear force to disrupt the liquid filament, but eventually, the absolute droplet size seems not to be influenced by it. It may influence the disintegration length of the liquid film, though according to the results, it does not influence the droplet size, which indicates an already short liquid ligament length. The droplet distribution over the

combustor diameter, on the other hand, will definitely be influenced by the swirl value due to a change in the flow field, but this was not topic of this work.

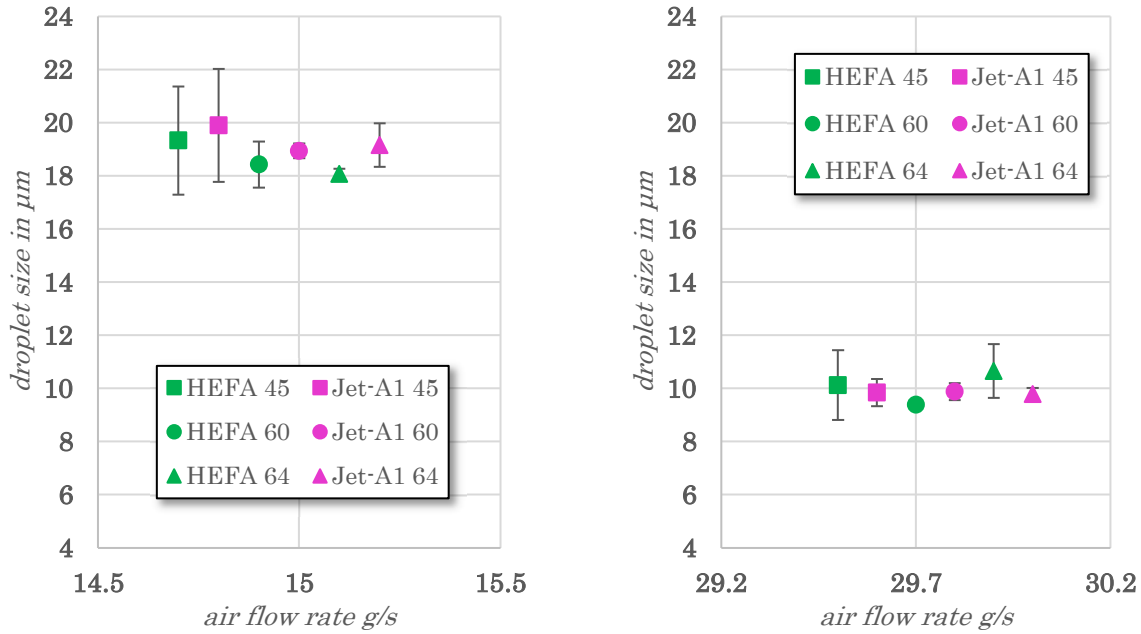

Figure 21: detailed look at SMD for 14.9 (left) and 29.7 g/s (right) for different OSW and both fuels

The case of droplet size during combustion (hot flow) is presented in Figure 22. The observation area was kept the same, which is near and below the leading edge of the flame. Again, for better comparison, the results for the different air flow rates (14.9, 20.4, and 29.7 g/s) were put next to each other for different swirl numbers and fuels. The grey line represents the mean values of Figure 20. Compared to Figure 20, the HEFA cases show a rather clear tendency of having a lower SMD than the Jet-A1 cases. With an increase in airflow rate, the difference towards to cold flow SMD values reduces. With an OSW of 64°, lowest SMD could be reached. This comes from the flame position near the wall, causing a much higher temperature near the injection compared to 45° and 60° OSW, which creates a lifted flame (Figure 46). SMD values of 45° and 60° OSW show similar values.

The Interferometric Laser Imaging for Droplet Sizing technique was also used for high temperature and high-pressure cases. However, those measurements were unsuccessful due to the limitation of the

measurement technique and reduced visibility, which may stem from too small observable droplets. Charalampous et al. [78] mentioned, that with a decrease in droplet size, the scattered light intensity is decreasing. Additionally, at high temperature and high-pressure condition, the droplet count can be expected to be more than an order higher than for ambient conditions. Although the Interferometric Laser Imaging for Droplet Sizing was improved by Maeda et al. [70] to be used in a relative dense spray, a highly dense spray seems not to be the case [10].

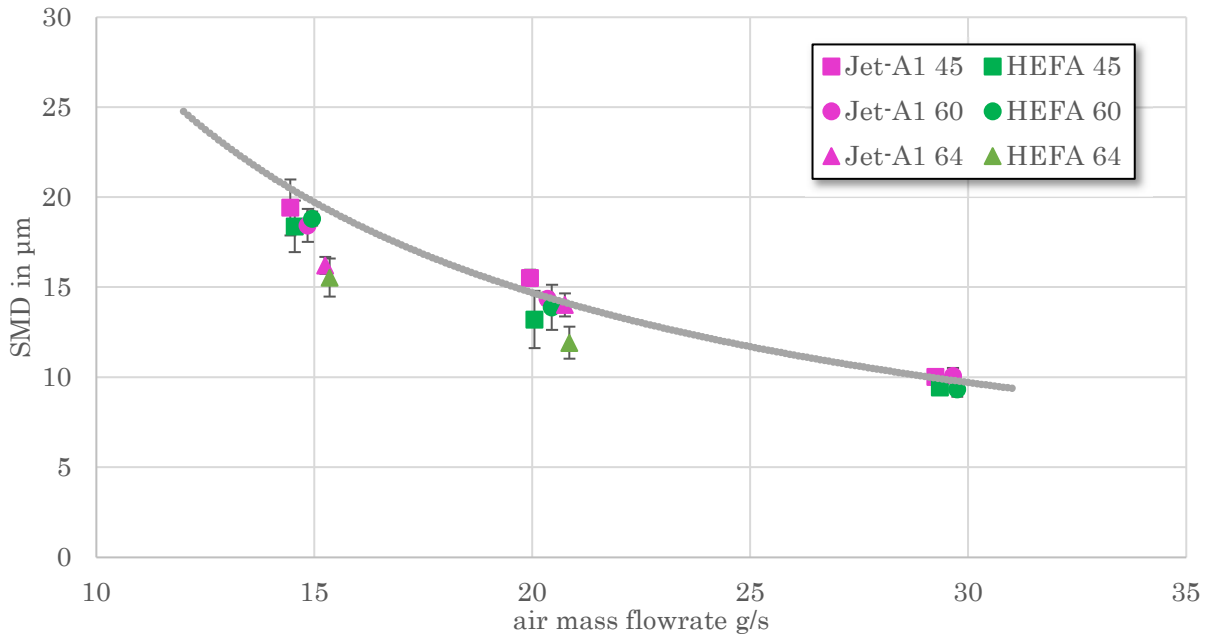

Figure 22: normalized SMD of different OSW for Jet-A1 and HEFA at combustion

2.3.2. Single droplet measurement of HEFA and Jet-A1

Single droplet evaporation experiments were conducted at several conditions and are shown in the following. Figure 23 shows the change in droplet size over time for both testing fuels. As mentioned in

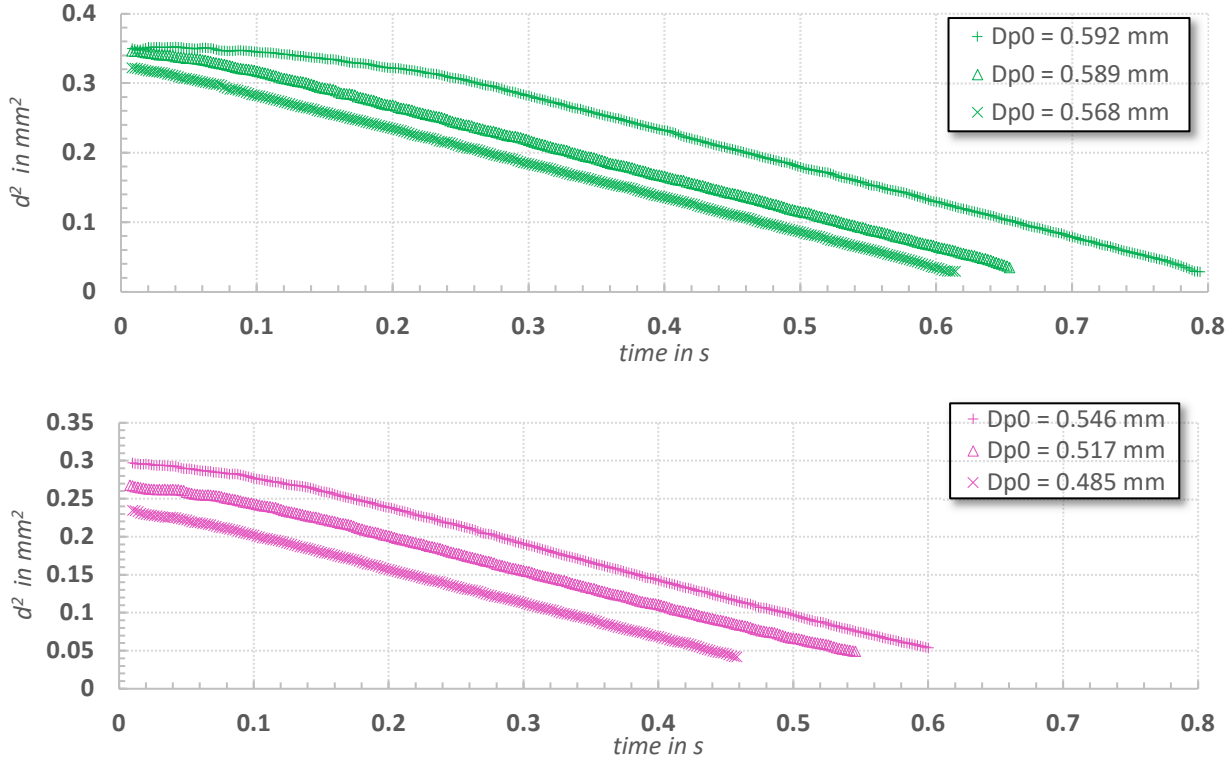

Figure 23: droplet size change over time at gravity condition in N_2 atmosphere; top: HEFA, bottom: Jet-A1

the previous subsection, the ambient temperature was 1023 K, the pressure was atmospheric, and the surrounding gas in this case was 100% nitrogen. The graphs do not indicate any remarkable differences at first glance, and Jet-A1 droplet seems to evaporate faster than HEFA, therefore results will be combined and normalized by each droplet's initial diameter (Figure 24), as suggested in [53]. The relative droplet changes show a distinguishable higher evaporation rate for HEFA compared to Jet-A1, according to the D2-law described in chapter 2.1.1. By forming the average of the droplet size change and derive the evaporation rate from it, which is the gradient of the droplet square change, another difference between the two fuels was revealed (Figure 25). When looking at the initial time, the bioderived jet fuel seems to have a longer heat-up time, which results in a lower evaporation rate

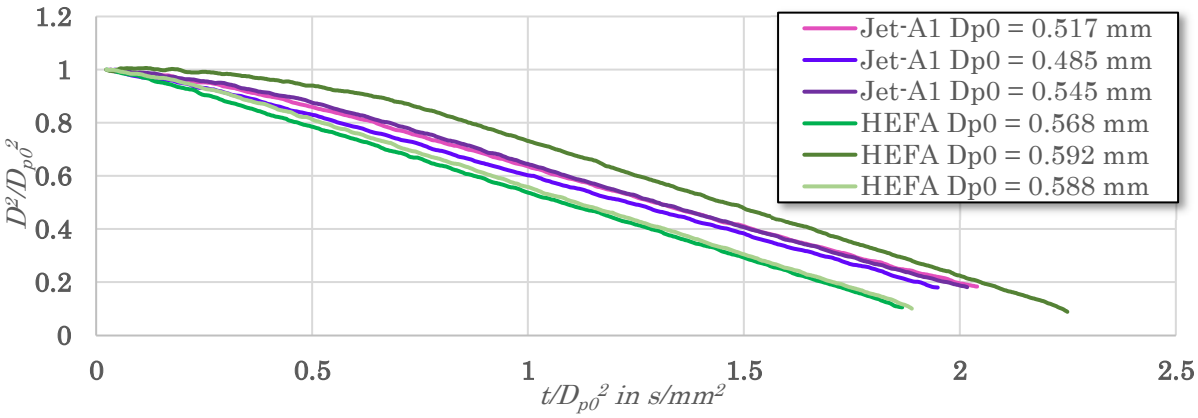

Figure 24: relative droplet changes over relative time interval

at the beginning of droplet evaporation. Soon after the initial phase, the superior evaporation rate of HEFA takes over and stays above Jet-A1 for the quasi-steady and end phase of evaporation. At the same atmospheric condition, but at microgravity, the identical difference in behavior could be observed (Figure 26). The stronger difference in the initial phase seems to stem from liquid expansion at the

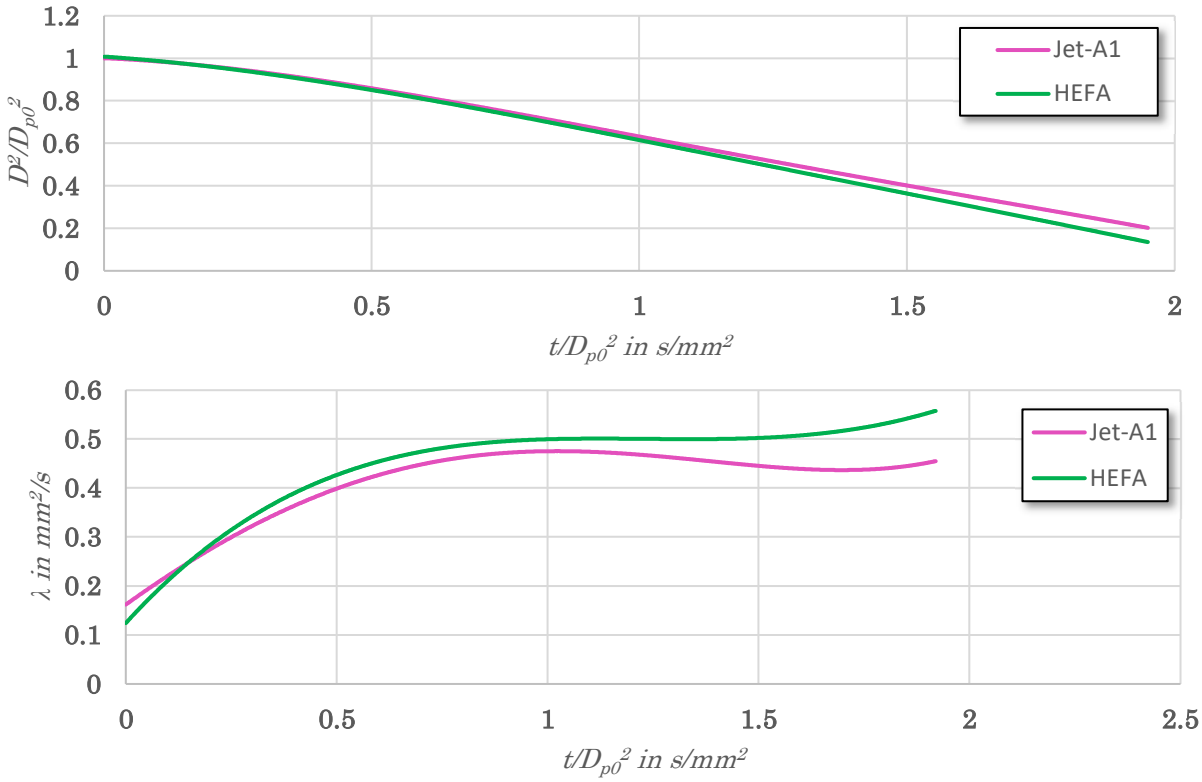

Figure 25: top: average of single droplet change over time; bottom: derived average evaporation rate

beginning of droplet evaporation in the case of HEFA, which would explain, why the evaporation rate starts from a negative value. Only one experiment was conducted, nevertheless, it shows similar behavior as in the case of gravity condition. Though, the total value of the evaporation rate is lower in the case of microgravity, the tendency between Jet-A1 and HEFA remains the same. The increased evaporation rate seems to stem from buoyancy-driven convection effects [79].

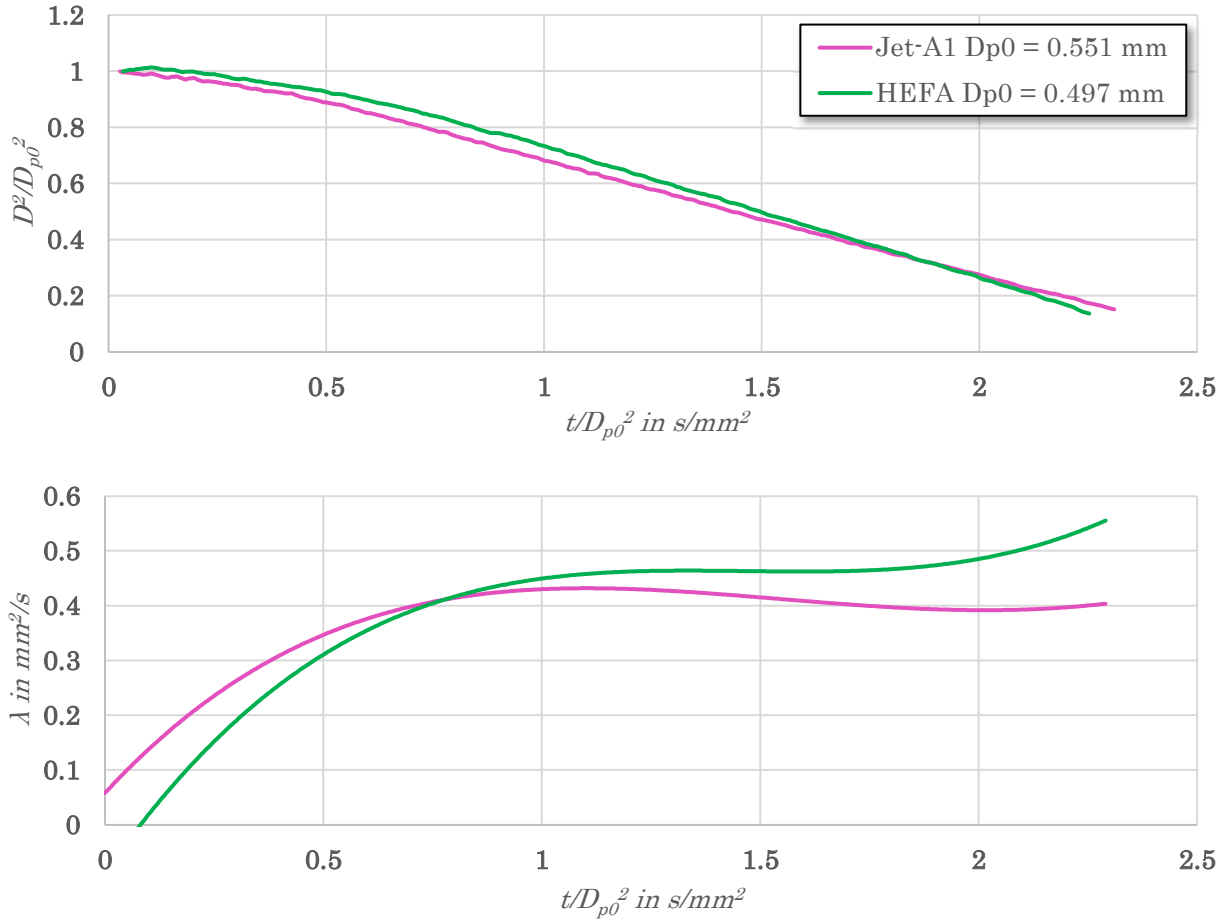

Figure 26: top: microgravity droplet size change over relative time; bottom: derived trend of evaporation rate

Lastly, droplets of HEFA and Jet-A1 were combusted at micro-gravity at a carbon dioxide enriched atmosphere, to reduce soot formation. These experiments also showed equal behavior as in the evaporation cases in a nitrogen atmosphere (Figure 24). The graphs show a slower heat-up period for HEFA, as described for the above images, but "catches up" with the Jet-A1 droplets. For both fuels, no

clear quasi-stationary burning rate was observable. The burning rate changed over time. This may come from the formation of soot (interaction with the soot bubble). Another influential factor is, that both, HEFA and Jet-A1 are multicomponent fuels, which may change their evaporation process over time due to different volatility of the components inside the fuel ([39]). This was not further investigated since the important information from here is the higher evaporation or burning rate of HEFA.

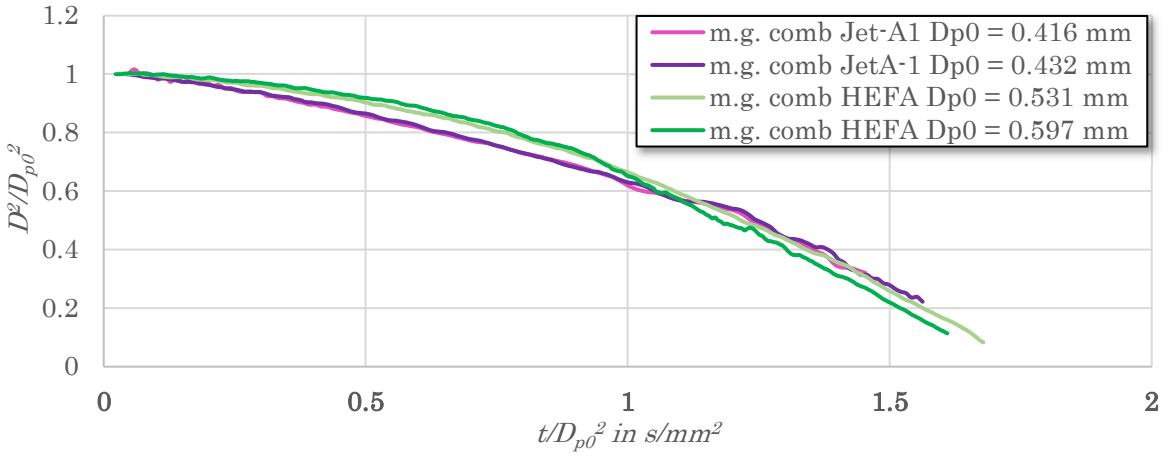

Figure 27: single droplet combustion at micro-gravity normalized

Analyzing the individual frames of the single droplet combustion experiments, it was found, that Jet-A1 does ignite earlier than HEFA. Although, from several literatures, it is known, that HEFA has a shorter ignition delay time. This might be an additional indication, that HEFA has a longer heat-up time. Looking at the above data, though, it can be seen that the initial droplet size of Jet-A1 droplets is smaller than those for HEFA which may be the reason for the later ignition of HEFA.

2.4. Discussion

2.4.1. Droplet measurement by ILIDS

Chapter 2.3.1 showed the results of cold flow and hot flow concerning droplet size for different outer swirler as well as HEFA and Jet-A1. Clearly recognizable is, that for a certain airflow rate, the droplet size does not change, rather it is because of the fuel or the OSW at cold flow. This means, that a dual swirl airblast prefilm injector is not influenced by the physical properties of the liquid fuel, at least within the values of Jet-A1 and HEFA. Compared with Sivakumar et al. [51], they showed similar results for Jet-A1 and camelina-based HEFA, but in a dual orifice atomizer. Additionally, they explained, that the cone angle of the spray does not experience any difference between the tested fuels. Shin et al. [48] published no difference in droplet size between Jet-A1 and several other biofuels, although the used biofuels showed all lower viscosities than Jet-A1. This is not the case for this work's fuels, where the biofuel has a higher viscosity than Jet-A1 (Table 1). Shin further stated that the atomization did not influence LBO limits, though their injector was a hybrid pressure swirl airblast atomizer.

The distribution of the droplet size along the air flowrate follows an obvious structure, known from several other atomizers [80]. To show this work's atomizing characteristic to be similar to other injectors of the literature, the characteristic curve was derived. Lefebvre created a detailed overview of several contributors to atomization in airblast atomizers. He concluded that viscosity forces tend to suppress the formation of waves on the liquid surface which normally leads to atomization. Further downstream, viscosity forces also resist the deformation of the produced ligaments into droplets. Surface tension forces tend to delay atomization by resisting any disturbances or distortions of the liquid surface, which usually leads to the creation of surface waves. An increase in density would more or less increase the distance of the liquid sheet to the produced filament, also causing delayed atomization. However, liquid density has a fairly small influence on the SMD. From Lefebvre's cumulation of empirical equations for prefilming airblast injectors, the most popular one is

$$D_{SMD} = A\left(\frac{\sigma}{\rho_A {U_A}^2 D_P}\right)^{0.5}\left(1+\frac{1}{ALR}\right) + B\left(\frac{{\mu_L}^2}{\sigma\rho_L D_P}\right)^{0.5}\left(1+\frac{1}{ALR}\right)^2 \qquad (21)$$

Shanmugadas et al. [81], although used on a hybrid simplex nozzle airblast injector, suggested several other empirical models for SMD prediction, which were developed over the decades, such as Hsiang and Faith [82] and Aigner and Wittig [83], presented as equation (22) and (23).

$$D_{SMD}\frac{\rho_A D_{SMD} {U_A}^2}{\sigma} = k\left(\frac{\rho_L}{\rho_A}\right)^{0.25}\left(\frac{\mu_L}{\rho_L U_A D_0}We\right)^{0.5} \qquad (22)$$

$$D_{SMD} \propto \sigma^{0.5}\ {\rho_A}^{-0.4}\ {U_A}^{-1.05}\ \delta^{0.3}\left(\frac{\dot{m}_L}{\rho_L}\right)^{0.15}\ {\mu_A}^{0.15} \qquad (23)$$

For the above equations, ρ_A, ρ_L are the density of air and density of the liquid, σ is the surface tension of the liquid, μ_A and μ_L are the dynamic viscosity for air and liquid, respectively, U_A is the inlet air flow velocity D_P is the prefilm diameter, δ is the prefilm layer thickness, ALR is the air-liquid-ratio, We is the Weber number and k is an empirical factor chosen to be 6.9 to fit the values of the measurement results.

Nevertheless, Figure 28 shows, that Lefebvre's suggestion fits the measured SMD values very well when choosing the values for constants A and B as 5.54×10^{-4} and -2.8×10^{-3}, respectively. A similar agreement found Burger et al. [49] and Tareq et al. [50], used on a hybrid pressure swirl airblast injector and a Parker-Hannifin-based injector, respectively. With having a fitted equation (21) for measured SMD, the SMD for other conditions can be well estimated, e.g. the droplet size for the high temperature and high-pressure condition. A simple sensitivity analysis of several parameters onto equation (21) shows in Figure 29, that SMD seems only sensitive to surface tension regarding fuel physical properties. In case of a heat-up of the fuel inside the pipeline during high temperature and high-pressure experiments, the atomization might be enhanced, because viscosity, surface tension, and density values reduce with an increase in temperature. Nevertheless, the exit temperature of the fuel was not measured, and can therefore be not further investigated. Figure 29 also shows that SMD might be strongly affected by the incoming air condition. Considering e.g. the air flow velocity, which

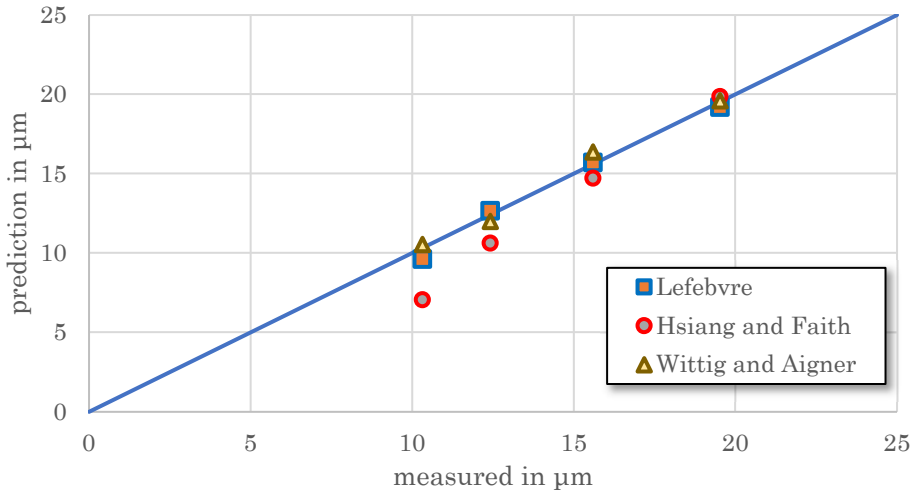

Figure 28: Comparison of different empirical equations for SMD prediction

is directly related to air mass flow rate and compare Figure 29 with results in Figure 20, it is clearly recognizable, that the reduction of SMD by nearly 50% when the air flow velocity is increased by 100% in the sensitivity analysis correlates very well with the resulting reduction in SMD when increasing air mass flow rate from 14.9 to 29.7 g/s in Figure 20. Therefore, considering high temperature and high-pressure condition as well, the incoming air will reach a density of approximately ρ_{air} =

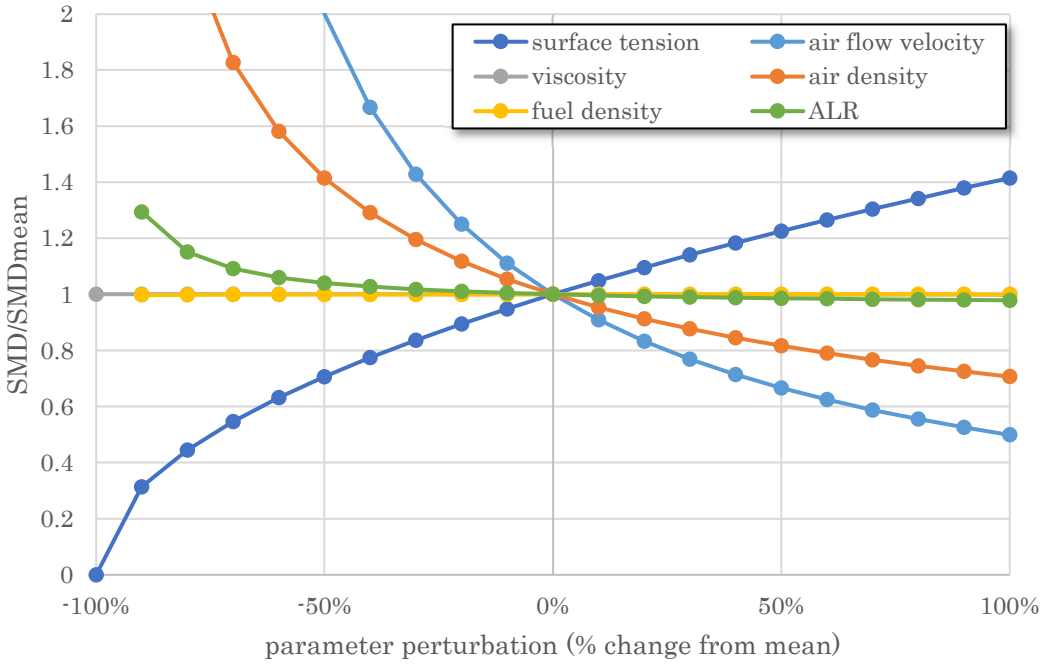

Figure 29: sensitivity of SMD using equation (21)

2.764 kg/m^3, when using 0.5 MPa as pressure and an inlet temperature of 630 K for calculation. This will lead to an additional reduction in the SMD size by 34% compared to ambient conditions.

For completion purposes regarding atomization, the Weber number was calculated, to show its neglecting value between HEFA and Jet-A1. Table 3 shows the values for We for both fuels, which concluded that the atomizing process over the range of tested airflow rates does not change.

Table 3: Weber number for HEFA and Jet-A1 (low load condition)

Air flow rate	We_{HEFA}	$We_{Jet\text{-}A1}$
g/s	-	-
14.9	23.1	22.0
18.2	34.4	32.9
20.4	43.3	41.3
22.6	53.1	50.7
25.7	68.7	65.6
29.7	91.8	87.6

2.4.2. Error analysis of HEFA and Jet-A1 similarities

ILIDS is a direct measurement method of droplet sizes, which makes it independent of light intensity and therefore creates a general error with neglectable value (below 1.5%) [72][84]. However, due to the discretization of the droplet size, which is in the current configuration 1.7 µm/Stripe, strong discrepancies can occur between true size and measured size. The influence of this quantization error increases with the decrease of absolute droplet size. On the other hand, such a quantization error can be reduced with a high enough sample rate. Since the Sauter Mean Diameter is used for describing different conditions of the atomizer and the influence of fuel property differences, the influence of quantization might reduce. Using Figure 20 and add the upper and lower maximum error of the quantification, which is half of the step size, it is recognizable, that the measured data cover the quantification error (Figure 30). Therefore, the deviation of the measured data is looked into in more detail.

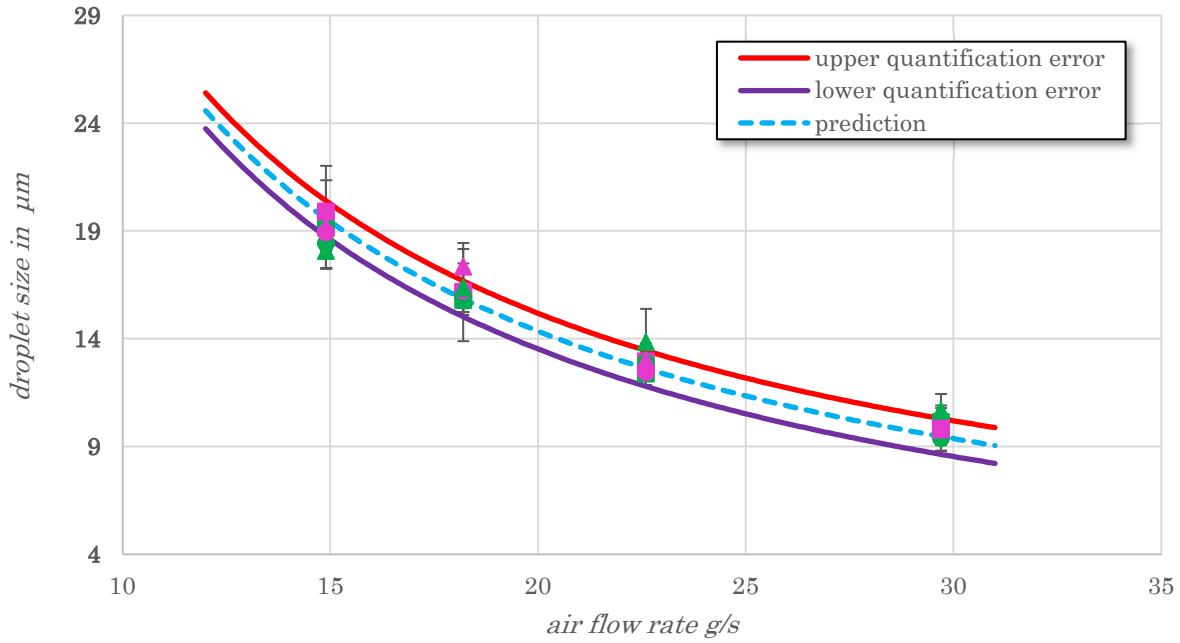

Figure 30: Quantification error of ILIDS measurement

Each case was at least tested three times, which is a rather small sample rate. Nevertheless, the resulting SMD gathers within a specific margin. The most important question to answer is if the similarities between the initial droplet size of HEFA and Jet-A1 are random or statistically sound. Therefore, the standard error of the mean value can be calculated with (24)

$$\sigma_{\bar{x}} = \frac{\sigma}{\sqrt{n}} \qquad (24)$$

which represents the standard error of the mean value for each case. Clearly, with a high number of cases "n", the variation of the error of the mean decreases. Nevertheless, the standard error for mean for each case did not exceed the relative quantifying error at tested air flow rates. To determine rather or not the true mean of HEFA droplet size and Jet-A1 droplet size are similar, a null hypothesis with a t-test distribution is used for approximating this probability (25).

$$Pr\left\{-\left|\frac{\bar{x}_{HEFA}-\bar{x}_{Jet-A1}}{\sigma_{(\bar{x}_{HEFA}-\bar{x}_{Jet-A1})}}\right| \le t_v \le \left|\frac{\bar{x}_{HEFA}-\bar{x}_{Jet-A1}}{\sigma_{(\bar{x}_{HEFA}-\bar{x}_{Jet-A1})}}\right|\right\} = 1-\varepsilon \qquad (25)$$

$\bar{x}_{HEFA}$ and $\bar{x}_{Jet-A1}$ represent the average mean value for each tested case of HEFA and Jet-A1, respectively, $\sigma_{(\bar{x}_{HEFA}-\bar{x}_{Jet-A1})}$ is the difference in the standard error of the two fuels' mean value and (1-

ε) is the indication for the probability. The t-test is a useful method for cases with a low sample rate [85]. With the testing hypothesis, that initial droplets in the case of HEFA and Jet-A1 are similar, the probability of that hypothesis is shown for each case in Table 4. For a confidence interval of 95% with a degree of freedom of 4 (n1+n2-2), the range of difference between the mean of the initial droplets of HEFA and Jet-A1 for the 45° OSW cases is ±2.26 µm for an air flow rate of 29.7 g/s. The difference in the mean between the two fuels is at the same condition 0.28 µm, which gives a statistical indication, that the two fuels do not differ from each other. This is also the case for all other tested cases.

Table 4: 95% confidence interval vs. mean value difference in µm

Outer Swirl Angle \ Air Flow Rate in g/s	14.9	20.4	22.6	29.7
45° - confidence interval	4.71	3.82	1.60	2.26
- mean value difference	- 0.57	- 0.37	- 0.56	- 0.28
60° - confidence interval	1.26	1.77	0.96	0.50
- mean value difference	- 0.51	- 0.32	0.46	- 0.49
64° - confidence interval	1.36	2.22	2.55	1.66
- mean value difference	- 1.09	- 0.98	0.83	0.88

Due to the small sample rate and the resulting big standard error, the range for a 95% confidence interval is relatively wide. For higher accuracy and more reliability in those data, more samples are needed in future analysis. Nevertheless, the null hypothesis shows no significant difference between the two fuels, and combined with the sensitivity analysis of the previous sub-section, it is concluded that the two fuels produce same initial droplet sizes.

2.4.3. Single droplet evaporation

The result section showed, that in all cases (gravity, micro-gravity, and combustion), that HEFA has always a higher evaporation rate at the quasi-stationary regime or in case of combustion, in the second half of the process. In detail, the evaporation rate at 1023 K for HEFA was 0.502 mm^2/s with a

standard deviation of 0.009 mm^2/s, and Jet-A1 reaching an evaporation rate at the same condition of 0.451 mm^2/s with a standard deviation of 0.013 mm^2/s. The deviation at steady-state condition is in both cases below 3% and therefore neglectable. After the steady-state evaporation, the droplet size accelerates its decrease in size. This might come from the influence of the suspender, which stabilizes the droplet as shown in Figure 18. In general, though, both fuels show strong similarity in the evaporation process. Liu et al. [86] e.g. did experiments with similar fuels and showed equal results regarding evaporation rates. In another publication, he showed the evaporation of n-decane/iso-octane/toluene surrogate and each single component fuel. It could be seen that toluene had the lowest evaporation rate, similar to Jet-A1, which indicates, that Jet-A1's lower evaporation rate might stem from the high aromatic content.

Since the single droplet experiments were conducted at 1023 K, but inside the combustor, we can easily reach temperatures of ~2000 K, the superior evaporation rate needs to be modeled, in order to see it as "universal" behavior. Equations, introduced at the beginning of Chapter 2 require liquid properties, which are often not available for multi-component fuels such as HEFA and Jet-A1. Nevertheless, they can be derived/assumed with appropriate empirical equations. Using equation (5), the effective evaporation rate can be assumed for HEFA and Jet-A1 as single droplet evaporation. Lefebvre [10], suggested using T_{50} for the boiling point temperature for the calculations of evaporation rate, which represents the mean boiling temperature of a multicomponent fuel. The explanation for such simplification is because the boiling point has a direct relation to vapor pressure and fuel volatility. Lefebvre suggested using Watson's [87] approximation for the latent heat of vaporization L to calculate the transfer number B by

$$L = L_{T_b}\left(\frac{T_{cr} - T_s}{T_{cr} - T_b}\right)^{0.38} \qquad (26)$$

with T_{cr}, T_s, T_b, and L_{Tb} being the critical temperature of the fuel, the surface temperature of the droplet, the boiling point temperature and the latent heat at boiling point temperature, respectively. Watson further gives an approximation on calculating the latent heat of vaporization at boiling point, as shown in equation (27).

$$L_{T_b} = \frac{4.23\left(-68 + 4.877T_b + 0.0005\,{T_b}^2\right)}{MW} \qquad (27)$$

Riazi [88] presents several empirical equations for different gaseous and liquid properties. The following equation shows the calculation for the critical temperature of the fuel.

$$T_{cr} = 35.9413e^{\left(-6.9*10^{-4}*T_b - 1.4442*SG + 4.91*10^{-4}*T_b*SG\right)}{T_b}^{0.7293} SG^{1.2771} \qquad (28)$$

SG represents the specific gravity of the fuel, which is also called relative density and is a ratio of the actual density to water density. Riazi explains, that the equation is appropriate for hydrocarbon fuels with > C_{20}, but is also valid for carbon amount of $C_5 - C_{20}$ with an accuracy of 0.4%.

It was found, that by using the suggested T_{50} temperature, the steady-state evaporation rate underperforms by roughly 10% for both fuels. By using instead the initial boiling point temperature (Table 1), the calculated steady-state evaporation rate correlates well with the measured evaporation rate in the single droplet experiments.

Additionally, worth to mention here is, that despite the fact, that HEFA has higher values than Jet-A1 in the distillation curve above approximately 10% recovery, its evaporation rate is higher than the one of Jet-A1. Considering the above-used equations, this may be resulting from lower latent heat for HEFA due to higher molecular weight, and because of the lower critical temperature for HEFA due to lower density. Rock et al. [31][35][36] as well as Burger et al. [33][49] used the temperatures of the distillation curve to correlate the lean blowout with evaporation rate. Their results could only partly be correlated, which might be due to the reason stated here, especially for multicomponent fuels.

Table 5 gives an overview of the calculated parameters of the steady-state evaporation rate and the comparison towards the measurements.

With equation (7)-(9) and the appropriate parameters could then the heat-up period be calculated. Figure 31 shows the average normalized D2 movement of HEFA and Jet-A1 experiments, as well as the empirical model for both fuels. The model could be fitted, by choosing the initial temperature of the droplets at 400 K. The temperature was not measured during the experiments, but considering the setup in Figure 18, there might be the possibility, that the volume where the droplet

is in standby position heats up before the experiment. Comparing the model's values with the results from Chin et al. [60], an appropriate correlation for effective evaporation rate can be found.

Table 5: calculated parameters for T = 1023 K in nitrogen atmosphere

Properties	HEFA	Jet-A1
SG [-]	0.758	0.799
T_{cr} [K]	590.5	620
T_s [K]	416.62	416.36
L_b [J/kg]	210211.9	239819.9
L [J/kg]	208812.3	237433.5
B [-]	5.89	5.09
λ_{St} [mm²/s]	0.499	0.443
$\lambda_{St\_measured}$ [mm²/s]	0.502	0.451

Additionally, the model reflects the difference between HEFA and Jet-A1 properly, regarding the single droplet measurements. Therefore, this model was finally used to calculate the effective evaporation rate for different temperatures, which can be seen in Figure 32. Additionally to the

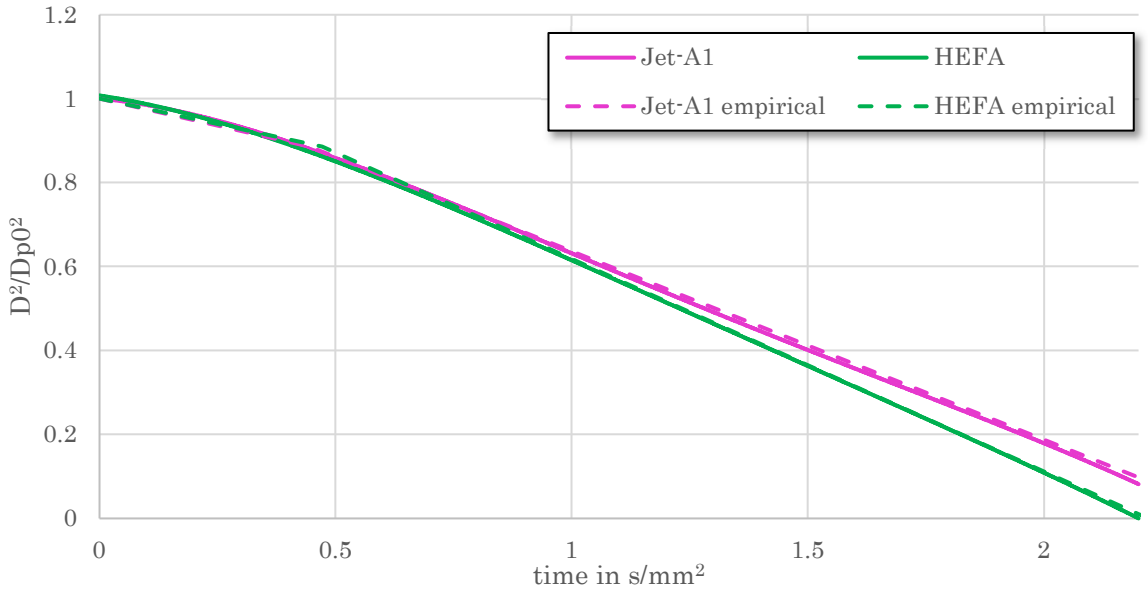

Figure 31: evaporation model compared to measurements

effective evaporation rate, the difference in evaporation rate between Jet-A1 and HEFA was also included. Visible is the almost constant superiority of HEFA towards Jet-A1, with a slight drop in the

high-temperature area. No significant difference between atmospheric and high-pressure condition can be seen. This comes from an increased heat-up time at high pressure as has been reported by [10]. The heat-up time makes almost 40% of the total evaporation time in the empirical model. Therefore, as stated by Lefebvre, neglecting the heat-up time can cause a significant error when calculating/assuming the droplet lifetime and should therefore be considered.

Comparing the single droplet results with the spray data from the previous subsection, it is clear, that the smaller SMD in the combustion case for HEFA comes from the higher evaporation rate. Equation (4) showed, that the evaporation rate is connected to the square of the droplets. Therefore, comparing the droplets of Figure 22 for each operational point, the following table can be derived:

Table 6: comparison of HEFA and Jet-A1 droplets from ILIDS measurement

Swirler	Air mass flowrate	D_{Jet}	D_{HEFA}	relative
[-]	[g/s]	[µm]	[µm]	[-]
45	14.9	19.43	18.385	11.7%
	20.4	15.51	13.21	37.8%
	29.7	10.02	9.45	12.42%
60	14.9	18.44	18.82	-3.76%
	20.4	14.37	13.89	7.03%
	29.7	10.08	9.33	16.72%
64	14.9	16.22	15.54	8.94%
	20.4	14.02	11.92	38.33%

Table 6 suggests a direct comparison between the droplets from the ILIDS measurement and the single droplet evaporation experiments does not give concrete accordance. However, except for one case, all the data show higher relative differences similar to the evaporation model in Figure 32. On the other hand, considering the droplet size measurement at combustion, values for the evaporation time can be derived. E.g. considering a mixed temperature of 650 K (average of 300 K inlet temperature and 1000 K from measured values near the wall), and an evaporating time of 0.54 ms (25 mm height as the center of observed droplet size measurement area, and 46 m/s injector exit velocity at 14.9 g/s), droplets should evaporate to 17.04 µm (considering an SMD of 19.55 µm at injector

exit). None of the cases in Table 6 could realize such evaporation. Several researchers (Zoby et al. [89], Imaoka et al. [90], Akamatsu et al. [91]) published and suggested a reduced evaporation rate due to small inter droplet spacings such as in a dense spray. It is acknowledged, that the evaporation might be influenced by the spray density, but without further analysis and temperature measurement inside the measured spray area, any assumptions would be arbitrary at this point.

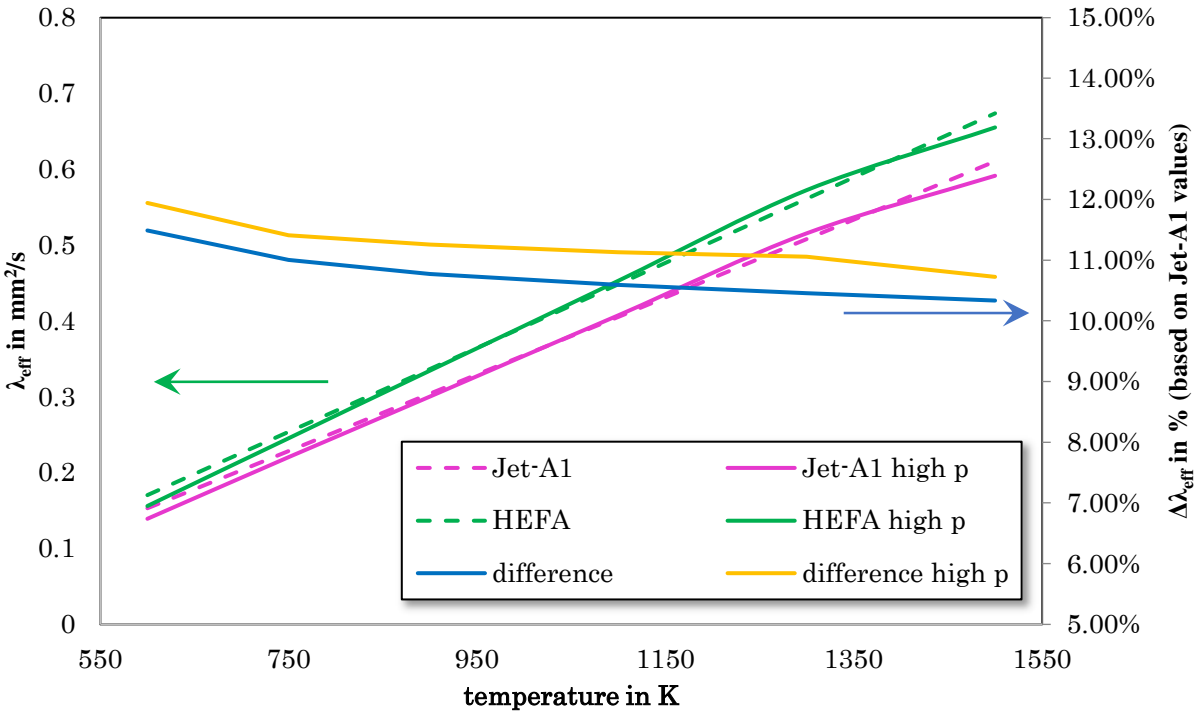

Figure 32: Effective evaporation rate of Jet-A1 and HEFA over temperature at ambient and high pressure

2.4.4. Influence of Droplet size and Evaporation rate onto Combustion

A difference in initial droplet size can lead to a difference in evaporation timescale, which further results in a different behavior in regards to not only static combustion stability (lean blowout) but also in regards to dynamic combustion stability, such as periodic oscillation [15][92]. The presented D2-law explains, that with an increase in droplet size, the lifetime of the droplets increases quadratically with the droplet diameter. The current chapter showed that the researched fuels do show similar initial droplets, despite their differences in physical properties. Due to the fuels' similarities in initial droplet size, the combustion is most likely not influenced by that, but it was also shown, that HEFA and Jet-A1 have a difference in evaporation rate, which can strongly influence characteristic timescales like evaporation time and lead to a difference in combustion behavior. A higher evaporation rate can for example lead to better mixing, which results in a better stabilization behavior. The measured and modeled differences in evaporation rate at a wide range of conditions showed a rather constant difference between the two fuels, with HEFA having a higher value compared to Jet-A1. The potentially higher stability of the biofuel HEFA, compared to the conventional fuel Jet-A1, can lead to reduced fuel consumption in future propulsion systems, such as presented in Chapter 1. Paired with the reduced environmental impact of HEFA, it can fulfill the goals of the aviation sector mentioned in Figure 2. Although the maximum mixing ratio of HEFA with Jet-A1 is regulated by the ASTM D7566 with a value of 50%, biofuel can still replace conventional jet fuels in other applications, such as stationary gas turbines. The mentioned aspects of HEFA's potential superiority demonstrates the necessity to be further looked into. Therefore, Chapter 3 focuses on the influence of evaporation rate on static and dynamic combustion stability.

Chapter 3. Stability and Optical measurement of HEFA and Jet-A1

3.1. Introduction

3.1.1. Combustion instability

A confined flame, e.g. inside a cylindrically shaped tube such as a combustion chamber, can exhibit oscillations due to sound waves emitted by the flame and reflected at the wall of the cylinder. Those waves can be periodic, chaotic, or fully random, which then would be considered as combustion noise. Especially periodic or quasi-periodic flame behavior can be dangerous, if those fluctuations couple or rather synchronize with pressure, causing periodic pressure oscillation. When synchronized, so that the Rayleigh criterion is fulfilled, high-pressure amplitudes can be the result, which may lead to damage of the combustor wall or injector, further causing blowout or even malfunction of the jet engine as described in Chapter 1. In the current chapter, the combustion fluctuation of Jet-A1 and HEFA flame near lean blowout limit is presented and discussed for high temperature and high-pressure condition. Optical measurement for ambient conditions is also presented, to further discuss the results of Chapter 2.

Most common instabilities in a combustor are acoustic instabilities like longitudinal oscillation or Helmholtz fluctuation, and swirl-based oscillations such as Precessing Vortex Core (PVC) or swirl number fluctuations. A rather new topic would be intrinsic thermoacoustic instabilities, where the flame itself causes a reflection and interaction with the combustor, creating a mode frequency unrelated to the mentioned instabilities. Oberleithner et al. [21] extensively discussed, that with an increase in airflow rate, the frequency of Precessing Vortex Core (PVC) also increases almost linearly, concluding that doubling the air flow rate resulted in a doubling of the PVC frequency. Besides, he showed that the PVC frequency also reduces with an increase in the equivalence ratio. This was also shown in other publications, such as Yan et al. [93] and Syred [20]. For this work, the focus will be on acoustic instabilities and the influence of fuel properties.

3.1.2. Lean Blowout Limit / Lean blowout relations

As mentioned in the introduction, Lean Blowout (LBO) is of crucial importance for future combustion technologies, to ensure safety but also to further understand the different behaviors of different fuels. Therefore, several researchers conducted experiments and derived empirical relationships to be able to predict LBO limit depending on fuel and combustor design. One famous relation was derived by Lefebvre [27], where he studied several fuels at their lean blowout limits, to be able to derive an empirical equation, which describes the LBO limit depending on fuel, conditional and geometrical properties.

$$\varphi_{LBO} = \left(\frac{A^* f_{pz}}{V_{pz}}\right)\left(\frac{A^* \dot{m}_A}{P_3^{1.3} \exp\left(T_3/300\right)}\right)\left(\frac{D_0^2}{\lambda_{eff} LCV}\right) \qquad (29)$$

The first term on the righthand side represents the combustor design. The second term is related to the combustion condition and the third term is governed by fuel properties, where A^* is a constant, f_{pz} is the air fraction entering the primary zone, V_{pz} is the volume of the primary zone, m is the mass air flow rate, P_3 is the pressure at injection, T_3 is the inlet temperature, D_0 is the Sauter mean diameter of atomized fuel, λ_{eff} is the effective evaporation rate and LCV is the lower heat value of the fuel. Lefebvre explained and derived in another work the effective evaporation rate, which describes the total evaporation of droplets, including heat-up time. This was already discussed in Chapter 2.

Rock et al. [35] tried to find the relation between LBO and a specific or several specific fuel properties. He concluded, that at low inlet temperatures (300 K), the difference in LBO of the tested fuels comes from the differences in vaporization. Vaporization was assumed by the distillation properties of the fuels and was mostly correlating to T_{90} temperature. Secondary connections were found in T_{50} temperature and viscosity. Viscosity might influence the atomization and indirectly prolong the evaporation rate of highly viscous fluids, especially since a pressure atomizer was used for those results. For higher inlet temperatures (450 K), Rock concluded the kinetic behavior of the fuels to be mainly responsible for LBO, which is represented by the DCN number. It was shown, that a high DCN number corresponds to a low LBO limit. Though, a slightly higher correspondence was found in Smoke

Point (SP) and C/H ratio correlation, which is an indication for reactivity as well, and is connected to extinction behavior. The highest negative correlation had the percentage of aromatic content in the fuels, which is related to Smoke Point and reactivity as well.

A follow-up paper of Rock [34] extended the data of his previous publication and added a higher inlet temperature experiment to it, with a total of 18 test fuels. His conclusion was similar to the previous work and stated, that lean blowout is a condition-dependent phenomenon. Nevertheless, the injector of this thesis has a different design, and in Chapter 2 was shown, the initial droplet diameter does not differ between the two fuels, so it can be excluded as an influential factor for the combustion limitation. Nevertheless, it was also shown, that the evaporation rate is higher for HEFA, which was also slightly measurable in the droplet size during combustion. Therefore, further experiments in this chapter should reveal rather or not evaporation rate has an influential effect on the combustion.

3.1.3. Heat release rate

As the name indicates, it describes the density of released heat of a flame, or better it describes the releasing energy of the combustion. In general, e.g. in a gas turbine engine, heat is the source to drive a turbine. In an engine, heat is produced by combusting fuel. The thermodynamic laws describe these processes in various diagrams, such as p-v or T-s diagram, which are only referred here but not deeper explained (for more information [94]).

The reactants, in a typical combustion case, hydrocarbons (CxHy) and oxidizer (air for atmospheric burners), are mixed and externally ignited or self-ignited, depending on the system. Either way, these ignition processes elevate the mixture over a specific activation energy, from where the reactants enter an exothermal process, releasing chemical heat while turning into products (typically water, carbon dioxide, etc.). During the combustion process, heavier hydrocarbons are broken down to lighter hydrocarbons and further to several species. Few of those species are responsible for the illumination of the flame at a different wavelength. In fact, optical emissions from flames are widely used in the research society, to describe and analyze heat release rate, flame behavior, shape, and intensity. One source of mentioned emission is chemiluminescence, which is induced by the electromagnetic radiation

emitted from the de-excitation of electronically excited species that are formed via chemical reactions in the combustion reaction zone. For example, CH* is radiated prior to the C_2 reaction chain. OH* is created at the oxidation of CH prior to the CH_x oxidation chain. Therefore, qualitative measurements of global flame behavior or heat release rate can be conducted by correlating the chemiluminescence signal to the chemical processes of the flame [95][96]. OH* mainly emits ultraviolet light, having an emission peak at around 309 nm, CH* is more responsible for the blue light in e.g. premixed flames with peak emissions at around 431 nm, C_2* often visible in rich flames having multiple peaks in the spectrum and CO_2* is visible with a broadband emission from 350 to 600 nm [97]. Several authors ([98],[99]) mentioned, that especially OH* might be an inappropriate marker for high-pressure combustion such as in a rocket engine, but at the same time describe CH* in good agreement for pressure levels used in the presented work. Additionally, CH* visualization also performs well as a flame position indicator. This is important for non-premixed spray flames to be able to detect lift-off height, like e.g. in [36][100][101] Since highspeed imaging of CH* chemiluminescence can be conducted in a very simple matter, plus such an optical observation is non-intrusive, it is chosen as the description of heat release rate in the current combustion experiments.

3.1.4. Spray visualization

For liquid fuel combustion experiments, especially in the case of non-premixed systems, exists the opportunity to illuminate the fuel in a very simple manner. Compared to gaseous fuel or premixed systems, where complicated optical systems are necessary, such as PLIF (Plasma Laser-Induced Fluorescence) to activate/excite radicals within the gaseous fuel or specific radicals mixed into the fuel (e.g. acetone) for the illuminating purpose (for more information, it is here referred to [102],[103]). The illumination process of liquid fuel or rather liquid droplets is rather straight forward. The light shines through the combustion chamber, and when droplets pass through it, they reflect a part of that light. This reflection is captured by a high-speed camera. With this simple and typically inexpensive method, information about injection time, delay, and spray formation can be extracted for non-premixed

combustion systems. By using laser light, focused to a sheet, the cross-section of the liquid spray can be lid up, considering the spray to be axisymmetric. This method is called Mie-scattering, which happens when the scattered particle (fuel droplets) are similar or bigger than the wavelength of the incident light [104]. It is also the base concept behind Particle Image Velocimetry (PIV). Because of its simple and rather inexpensive setup, compared to other methods, it is widely used in the research community ([50][105]) and is also the method applied in the current study.

3.2. Methodology

As mentioned in Chapter 1, HEFA and Jet-A1 are tested at different conditions, which also include differences in inlet temperature and chamber pressure. Therefore, both setups, one for ambient conditions and one for high temperature and high-pressure condition are introduced. Also, the measurement techniques, which are necessary to fulfill the objectives are subsequently described separately.

3.2.1. Setup for Combustion Experiments

3.2.1.1. Ambient condition facility

At the University of Tokyo Hongo Campus windtunnel, ambient condition combustion experiments were conducted. Nine high-pressure tanks, which can be filled by a compressor to up to 4 MPa, supply the experimental setup with sufficient air. The temperature of air can be assumed to be at ambient temperature. Fuel was supplied from a tank, which was pressurized with nitrogen with a steady pressure of 0.5 MPa, to ensure a constant supply of fuel. Ignition of the burnable mixture was done via a conventional propane burner. Schematics of the setup can be seen in Figure 33.

Also visible in Figure 33 is a window within the combustion chamber. This section of the chamber was designed in a previous study, to visualize combustion and combustion oscillation in a model rocket combustor. For synergic reasons, the used combustor was designed and adapted to fit that visualization section. Most of the combustor parts were produced from stainless steel, except the injector, which was produced from gunmetal, due to its easier processing abilities.

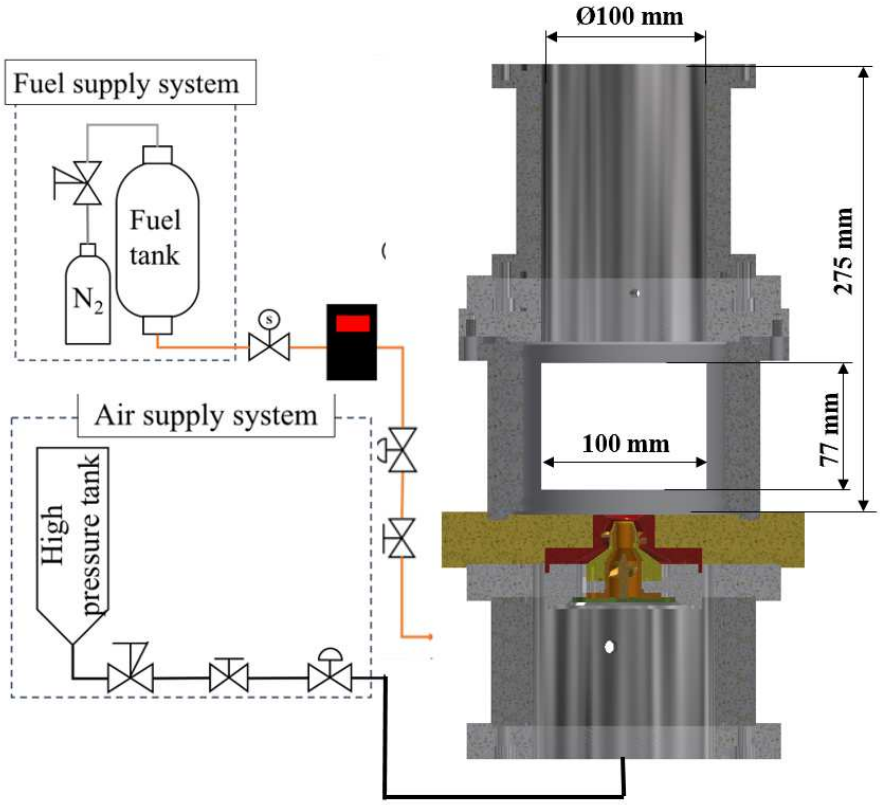

Figure 33: schematics setup for ambient condition

Air flow rate measurement

As mentioned before, air flow rate was provided through several pressurized air tanks. The air flow was controlled with a needle valve from Swagelok (SS-1 RS 6) with an orifice of 6.4 mm. Swagelok offers empirical equations to calculate the mass flow rate depending on the opening of the valve or rather how many turns the valve was rotated. With previous measurements, using a rotameter, to calibrate the needle valve. In a rotameter, a floating body moves through a pipe with a variable cross-section and stabilizes at a certain point at which the gravitational force of the floating body and the buoyancy forces from the airstream reach an equilibrium. By measuring the mass flow rate corresponding to different openings of the controlling valve, the valve flow coefficient (Cv) can be derived from equations (30) and (31), depending on the pressure ratio between the upstream and

downstream condition of the valve. Generally, the valve is operated in choked condition, which means the upstream pressure is always higher than twice the amount of the downstream pressure. This has the advantage, that the downstream system does not influence the air flow rate.

$$For\ 2p_2 > p_1: \dot{m}_A = N_2 C_v p_1 \left(1 - \frac{2\Delta p}{3p_1}\right) \sqrt{\frac{\Delta p}{p_1 G_g T_1}} \qquad (30)$$

$$For\ 2p_2 < p_1: \ \dot{m}_A = 0.471 N_2 C_v p_1 \sqrt{\frac{1}{G_g T_1}} \qquad (31)$$

p_2 and p_1 represent the downstream and upstream pressure of the used valve, respectively. Flowrate is designated with $\dot{m}_A$, Δp is the pressure difference, T_1 the temperature upstream, G_g the gravitational constant and N_2 is a unit constant, which depends on what units are used for the other parameters. Figure 34 shows a certain difference between the measured/calibrated flow coefficient and the one offered by the manufacturer. For the calculation and description of the conditions, measured values will be used from now.

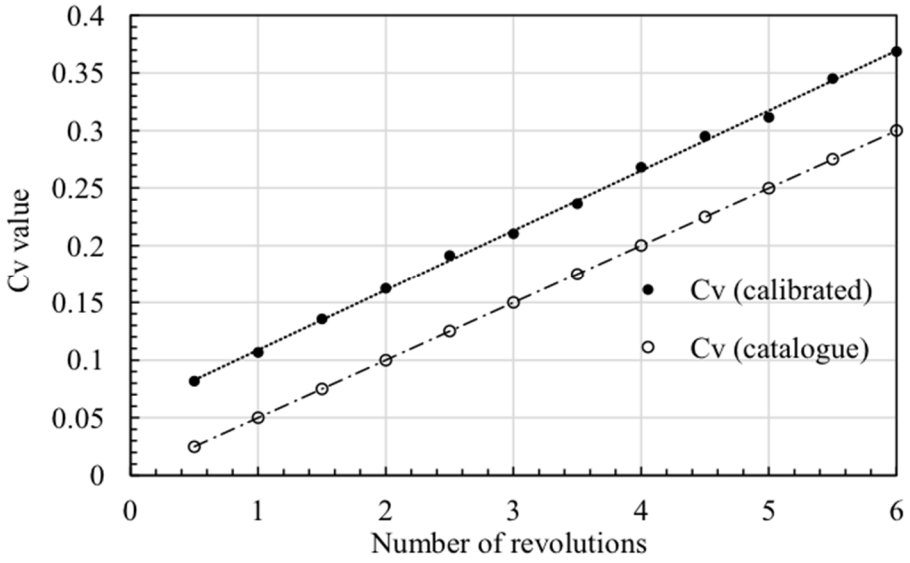

Figure 34: Calibration curve of needle valve for air mass flow rate

Fuel flow rate measurement

For measuring the fuel flow rate, a Coriolis flow meter from Keyence (FD-SS02A) was used, which is able to measure the density and temperature of the fuel, due to its unique function regarding Coriolis measurement. Adjusted was the fuel flowrate via a flow controlling/metering valve from Swagelok (SS-SS4-VH). Previously, the fuel flow rate was also calculated via valve opening and Cv value, but due to the small orifice in the metering valve, particles such as dust or other solid matter interfered with the flow rate within the controlling valve, losing its linear behavior as shown in Figure 34. The flow meter is connected to a Keyence Logger (NR200), to record the fuel flow rate, where a 4 mA signal corresponds to 0 mL/min and a 20 mA signal to 200 mL/min.

3.2.1.2. High pressure and high-temperature condition facility

The University of Tokyo Kashiwa Campus has a High Enthalpy – High-Pressure windtunnel facility located on its grounds (Figure 35). This facility simulates near jet engine conditions by providing a heated temperature and increased pressure. The red arrow in Figure 35 shows the flow path of the used section.

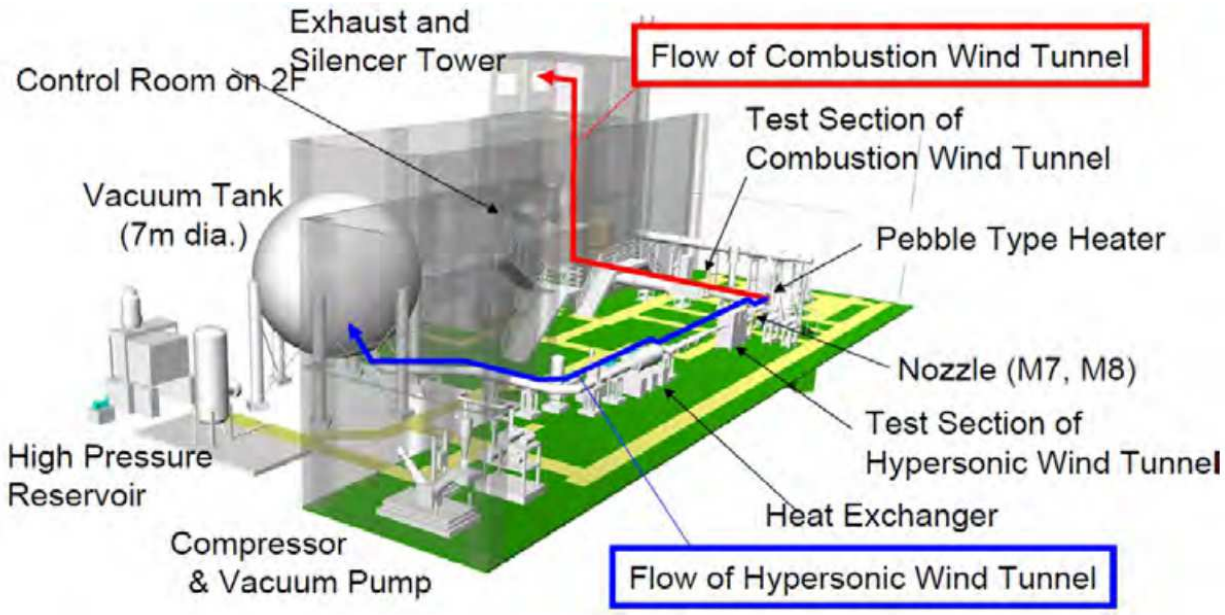

Figure 35: 3D overview of High Enthalpy and High-Pressure windtunnel (obtained from: (http://daedalus.k.u-tokyo.ac.jp/wt/info/UTHYP.pdf)

The high temperature and high-pressure condition, compared to the ambient condition described above, are of crucial importance because, in real jet engines, the inside of the combustion chamber can reach several times the atmospheric pressure and due to the compressor stages upstream of the combustion chamber, the inlet air temperature of the combustor can also reach several hundred degrees Celsius. The high enthalpy windtunnel is able to reach conditions of 1200 K, due to a Pebble Type Heater and a total pressure of up to 0.7 MPa, because of the High-Pressure Reservoir indicated in Figure 35. This lies within the necessary test conditions, which were chosen to be at around 600 K for temperature and 0.5 MPa for pressure, which correspond well with conditions near Lean Blowout.

To create a high pressure of 0.5 MPa inside the combustion chamber during the experiment, the shown chamber in Figure 33 is extended with a nozzle at the end, which dimensions are calculated, so that the mentioned pressure can be reached under certain airflow conditions. The complete setup for high temperature and high-pressure condition can be seen in Figure 36. Schematically added is as well the high-pressure tank/reservoir and the Pebble type heater from Figure 35. The heater is equipped with special ceramic pellets, which can store heat more efficiently. The whole heating process is conducted by burning city gas inside the heater until the adjusted temperature is reached. Since the actual experimental setup is geographically separated from the operating staff, everything needed to be designed so the system can follow an automated procedure. Compared to the manual ignition process for ambient conditions, the high temperature and high-pressure system is automatically ignited via a hydrogen-air igniter, controlled via Labview. Furthermore, the injection of fuel and trigger of camera and sensors recording was also done via Labview. The hydrogen torch started combusting 1 s before fuel injection and stops 12 s before the fuel combustion procedure was finished. The experimental sequence can be seen in detail in Figure 37. Several pressure sensors in the gas pipelines and observation via video camera used for the high temperature and high-pressure experiments, to ensure functionality and safety of the system.

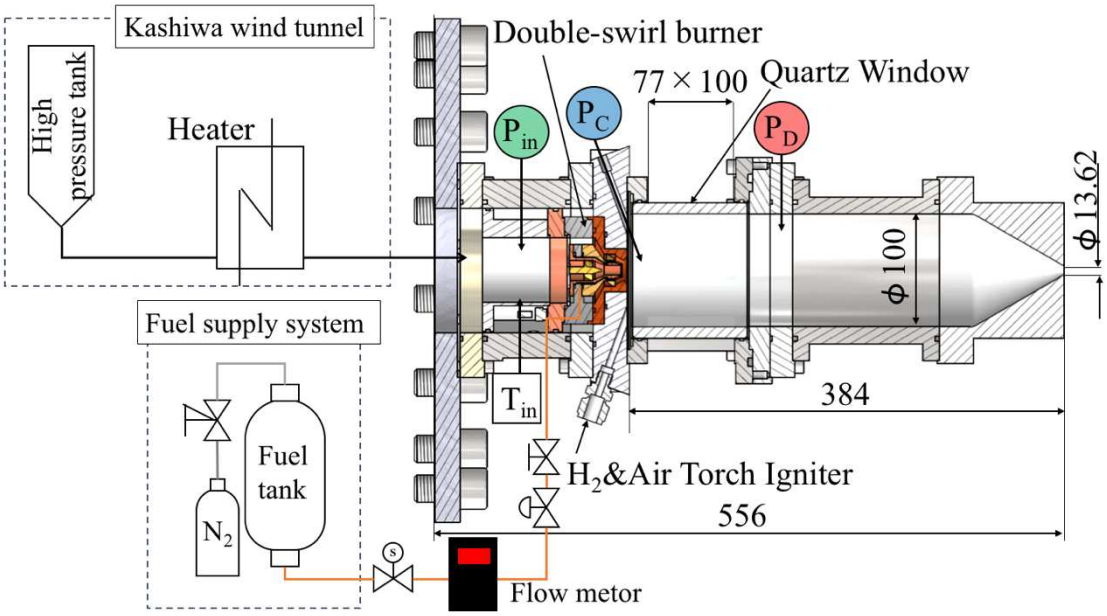

Figure 36: Setup for high temperature / high-pressure condition

Combustion Test

Time [s]	Labview	0	10	20	21	22	23	24	25	26	27	28	29	30	31	32	33	34	38	50	in s
Wind Tunnel	-																				
Air	C2																				
Spark	☆																				
H2	B2																				
Fuel	F1																				
Logger trigger	H1																				
Camera trigger	H1																				
Laser trigger	H1																				

Figure 37: Experimental sequence for high temperature and high-pressure condition

Air flow rate measurement

Since the air flow rate of this experiment was outside (below) the range of the facility's air flow rate measurement system, another way needed to be thought of to calculate the air flow rate. As mentioned before, to reach the necessary pressure inside the combustion chamber, a nozzle at the exit of the combustion chamber was used. This nozzle at the same time creates a choked condition at its smallest exit diameter, reaching sonic speed due to its only diverging form. This experimental setup is in a sense close to real jet engine geometry, because most real engines have a choked nozzle at the end of the combustion chamber, as stated by Dowling [106].

With the well-known equation for mass flow rate (32), the mass flow rate can be derived via NASA-CEA software, by iteration, until the air mass flow rate fits the condition [38][39]. For the solving process, the inlet temperature and the chamber pressure are necessary, which were measured during the experiment. Conservation of law depicts, that the sum of injecting mass flow rates (air mass flow rate and fuel mass flow rate) should pass through the exit nozzle as well the sum.

$$\dot{m} = \frac{Ap_t}{\sqrt{T_t}}\sqrt{\frac{\gamma}{R}}\left(\frac{\gamma+1}{2}\right)^{-\frac{\gamma+1}{2(\gamma-1)}} \qquad (32)$$

A is the cross-section of the smallest diameter in the nozzle, p_t and T_t are total pressure and total temperature, respectively, R is the gas constant and γ is the specific heat ratio. To calculate the mass flow rate of air, complete combustion is assumed. The software itself has the properties for jet fuel and resulting combustion gas properties.

Fuel flow rate measurement

The fuel flow rate was measured as in the ambient condition, with the Keyence mass flow meter (FD-SS02A).

3.2.2. CH* chemiluminescence

Additional to the setups presented further above, a high-speed camera was used with a Nikon Nikkor lens (f85) and an optical bandpass filter with a wavelength of 432 nm (±10 nm), to let only light through, related to CH* chemiluminescence, to record qualitatively the flame behavior and heat release rate. As mentioned before, light emission from CO_2 are superimposed on CH*, but for simplicity, this is being ignored. Figure 38 shows the schematics of the setup at ambient condition. For the CH* chemiluminescence, a V2511 Phantom camera was used with a framerate of 4000 fps. In case of ambient conditions, this setup was mainly used to analyze the lift-off height of the swirling flame. The equivalence ratio was kept at 0.7 and the airflow rate was changed. When the experiments were done for Jet-A1, the fuel was changed, and the conditions were repeated without touching the optical setup

to have an accurate comparison between the two fuels. For the high temperature and high-pressure condition, since those were conducted in another campus, the equipment was limited to the high-speed camera LC310 from Phantom with a framerate of 2000 fps and the same optics as mentioned before for CH* chemiluminescence observation. Since pressure was compared to the heat release rate, two high-frequency pressure transducers (Kyowa) were used to measure the pressure inside the combustion chamber. One sensor at the face plate of the combustion chamber, and one 120 mm further downstream as schematically shown in Figure 36. An additional sensor was installed upstream of the injector, to measure the inlet condition.

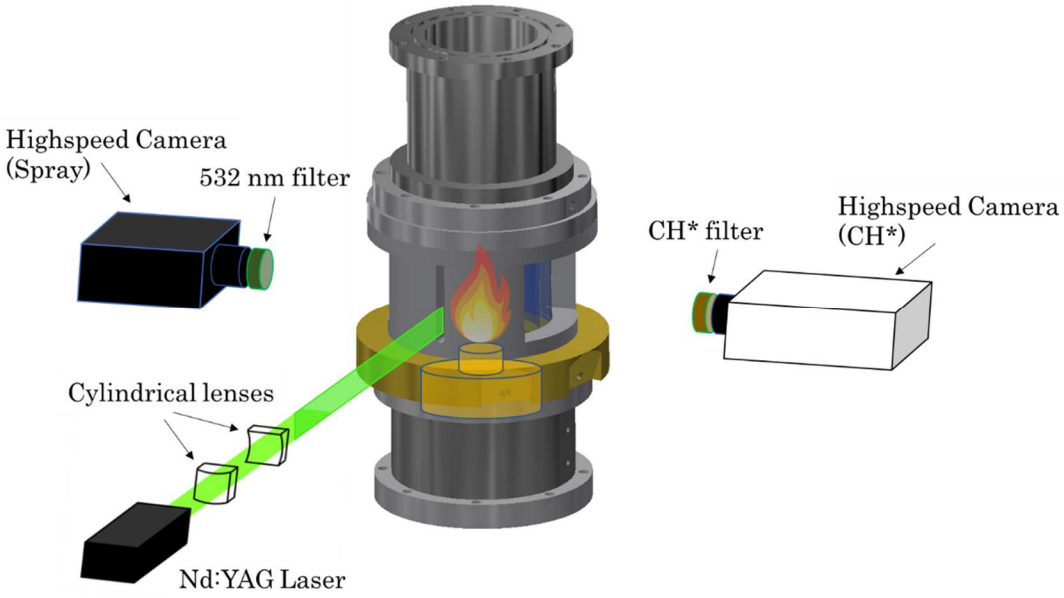

Figure 38: Schematics of optical measurement at ambient condition

3.2.3. Mie scattering

Mie scattering can be realized, with an optically accessible combustion chamber, a light source, and a high-speed camera. For the illumination of the spray, a Nd:YAG laser (Changchun New Industries) with 532 nm wavelength was used. With two cylindrical lenses (CLB-3030-300NM and CLB-3030—1000PM) an appropriate laser sheet was created, to “cut” through the spray, created by the injector,

as presented in Figure 38. The sheet had an approximately 1 mm thickness and a height of 70 mm for ambient condition tests to illuminate the maximum area possible of the observation window. In case of high temperature and high-pressure condition, the laser sheet was focused to 30 mm height since the spray penetration height was much shorter compared to ambient conditions. For the images, a high-speed camera V710 from Phantom with a framerate of 4000 fps was used in ambient conditions. Again, for the high temperature, high-pressure conditions, due to the different location, the equipment was limited to a MiroEx2 Phantom camera with 2000 fps maximum framerate. Spray images were observed near lean blowout limit in both, ambient and high temperature and high-pressure conditions.

3.3. Results

3.3.1. LBO at ambient condition

In case of ambient conditions, the LBO limit was determined, by first adjusting the fuel flow rate before airflow is turned on. After air flow and igniter was set, fuel was injected. As soon as combustion started, the igniter was removed. As long as the flame remained burning for more than 60 s, the tested condition was determined to be "stable". Figure 40 and Figure 39 show typical flame behavior of a blowout case and a stable case, respectively. Each figure shows 12 consecutive images of the flame's CH* chemiluminescence over time, with a timestamp of 1 ms (frame rate 1000 fps). In the case of a blowout, the CH intensity reduces with each frame, until the flame completely disappears. This can

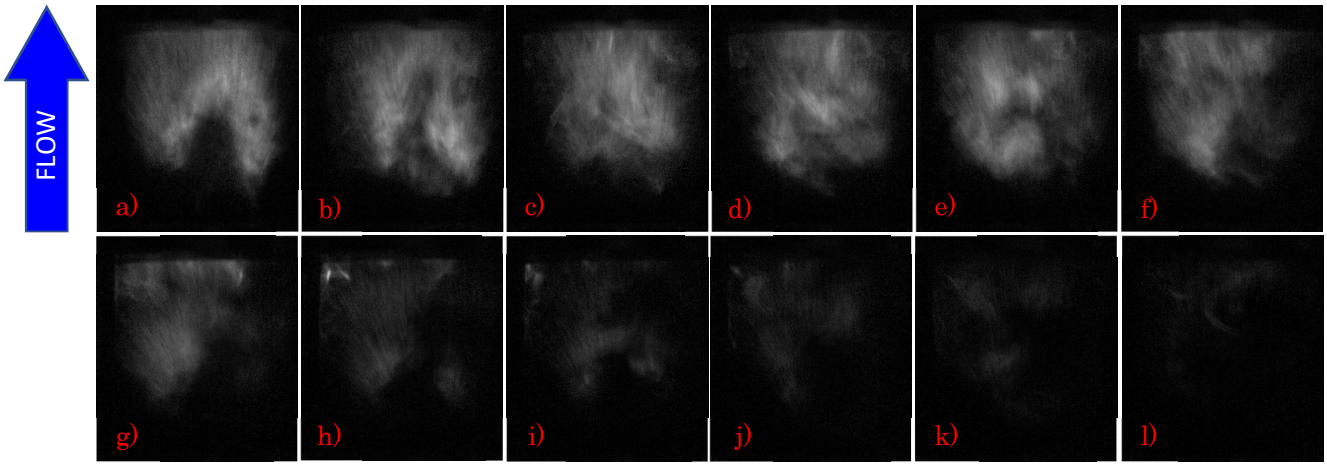

Figure 40: Blowout (φ = 0.632) of HEFA flame at ambient condition at an airflow rate of 25.7 g/s

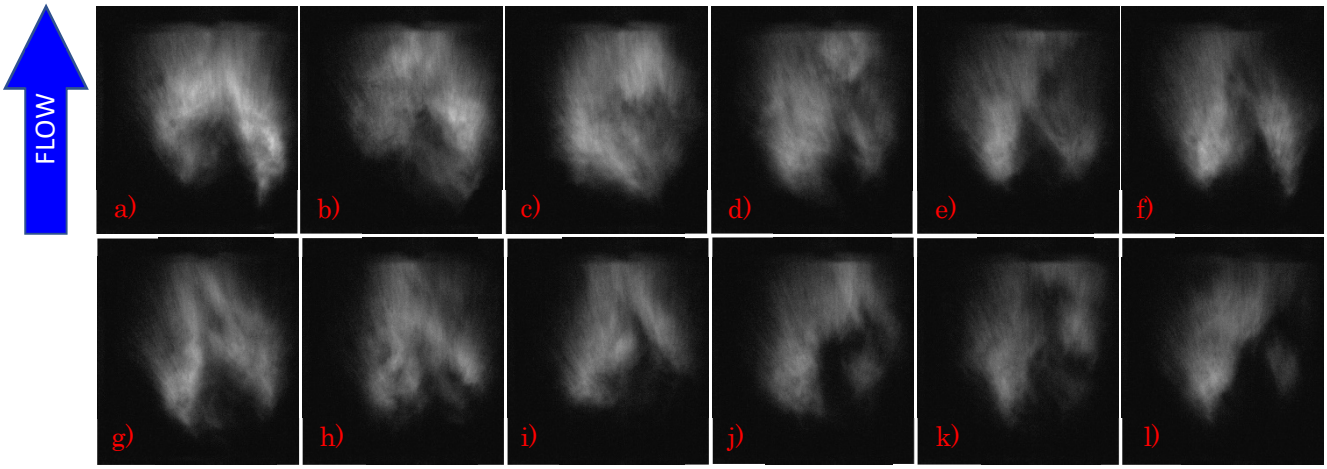

Figure 39: Stable combustion (φ = 0.862) of HEFA flame at ambient condition at an airflow rate of 25.7 g/s

happen several times due to the reignition of the flame until the flame permanently blows out. For the stable case, CH intensity remains similar, as well as flame shape. Similar behavior was observed for Jet-A1 and HEFA, therefore only the HEFA blowout and stable case are shown. If a blowout occurred, the condition would be reignited and if a second blowout occurred, this condition was considered a blowout for the set airflow rate. This was repeated several times, to detect a clear separation between "stable" and blowout conditions as can be seen in Figure 41.

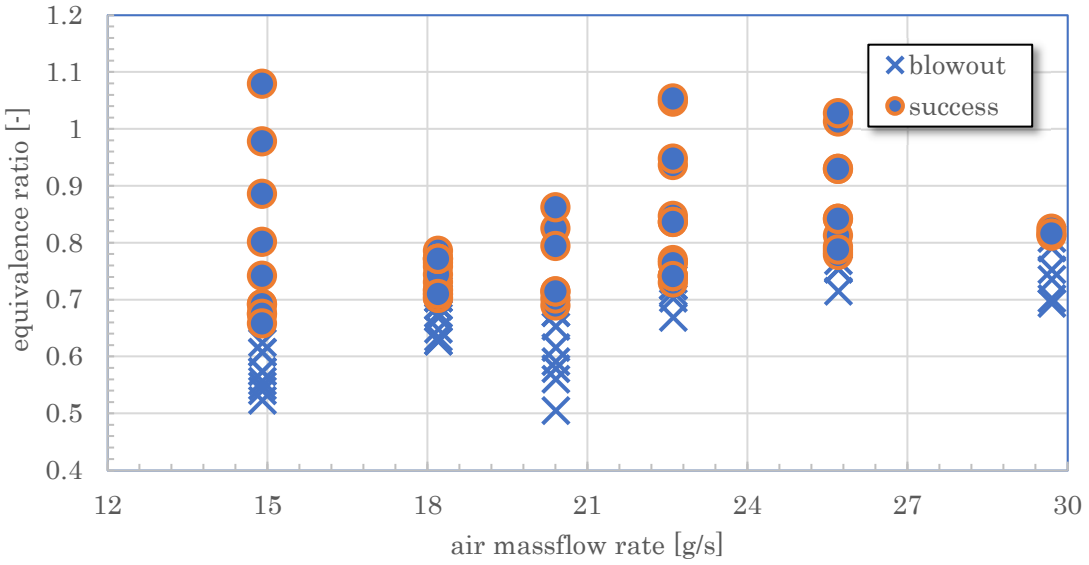

Figure 41: LBO limit at different air flow rates for 45° OSW Jet-A1 case

The non-blowout condition was marked as "stable" because several researchers (e.g. [109]) reported a transition area between truly stable and blowout, where the flame is unstable but does not blowout. According to those papers, this had often something to do with the lift-off height of the flame, where a stable condition is related to attached flame and unstable to lifted flame. Nevertheless, for this work, the focus was not on the unstable area, since for a small swirl number (swirl angle 45° in Table 2) the flame was always in a lifted position. Due to its non-premixed nature, the flame typically stabilizes at a certain distance from the injector.

Logistic regression analysis

In Figure 41, a clear separation between blowout and non-blowout is visible, but to further increase the accuracy of the transitioning limit, the results needed to be statistically processed. A useful tool for that is the logistic regression analysis, which gives a distinct result for a binary problem. The binary problem, in this case, is either blowout or not blowout, depending on the adjusted equivalence ratio. With the aid of logistic regression, the interception point can easily be found out with appropriate deviation. For the logistic regression, a logistic function is used, which takes any real value between "0" and "1", which represent in this case blowout and stable combustion, respectively. The result is an S-shaped curve, also called the Sigmoid function [110]. In the following, a short description of the process is given.

$$\varphi_i = e\text{quivalence ratio for } i^{\text{th}} \text{ test}$$

$$y_i = \begin{cases} 0 : \text{Blowout} \\ 1 : \text{Stable Combustion} \end{cases} \qquad (33)$$

$$P(\varphi) = \frac{1}{1 + \exp(-\beta_0 - \varphi\beta_1)} \qquad (34)$$

P(φ) is the Sigmoid function and represents the probability of a stable flame, at a specific equivalence ratio. The task is, to derive the two constants β_1 and β_2 to describe this function. This can be done with the maximum likelihood method, where the two constants are chosen so that the following equation reaches a maximum:

$$L(\vec{\beta}) = \prod_{i=1}^{n} T(\varphi_i)^{y_i} \left(1 - T(\varphi_i)\right)^{1-y_i} \qquad (35)$$

The lean blowout equivalence ratio was defined as the equivalence ratio at which the flame stabilization probability becomes 50%. Therefore, by setting P(φ) = 0.5 in equation (34), the lean blowout equivalent ratio φ_{LBO} is

$$\phi_{LBO} = -\frac{\beta_0}{\beta_1} \qquad (36)$$

Figure 42 shows the results when applying the logistic regression on the data from Figure 41. Each plot represents one air flowrate and a clear increase in LBO is visible with an increase in airflow rate. The solid line is the regression line obtained from the data and the blue dashed line represents the

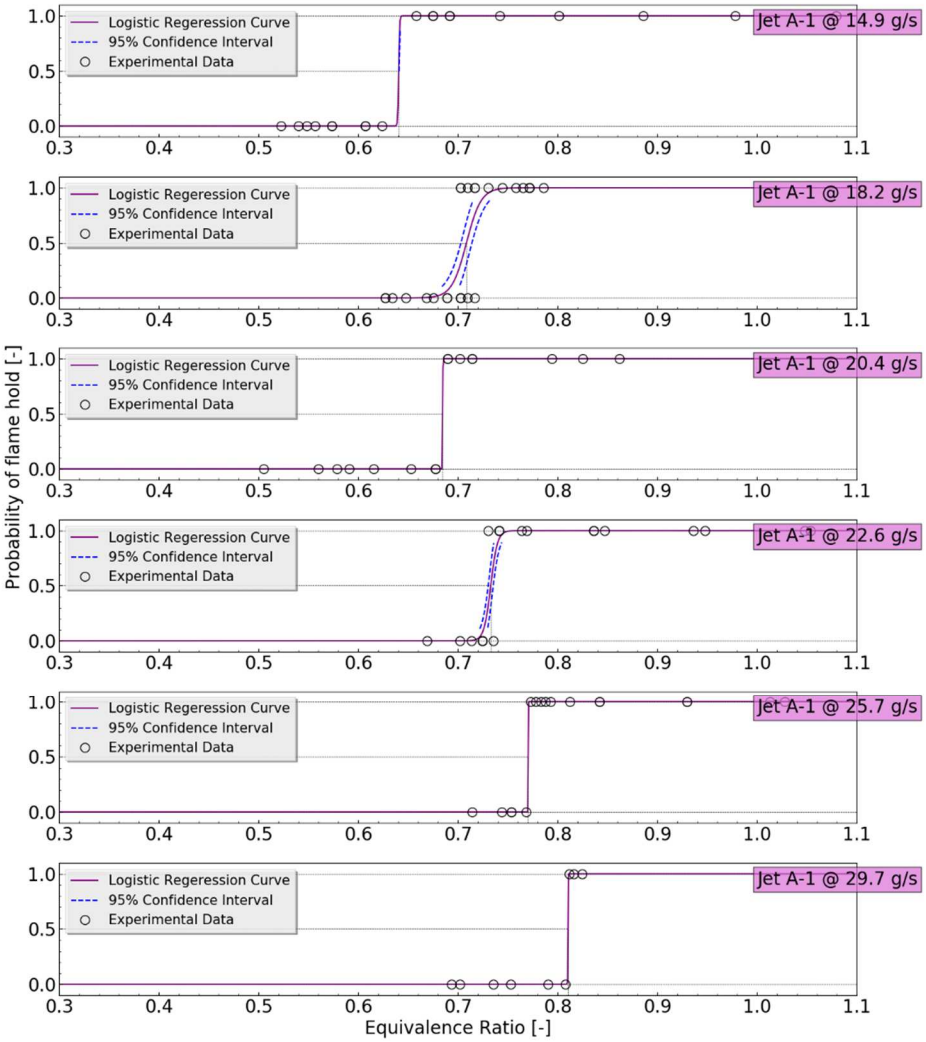

Figure 42: Regression logistic for 45° OSW for Jet-A1 at different air flow rates

95% confidence interval, which means that the true value of the LBO limit lies within this area with a 95% probability.

It can be seen, that even with a relatively small number of experiments for each condition, the LBO limit can be discovered accurately, due to the nature of LBO behavior inside the combustor. Those experiments and post-processing were conducted for HEFA as well and shown in Figure 43. The results for both fuels are represented in Figure 44.

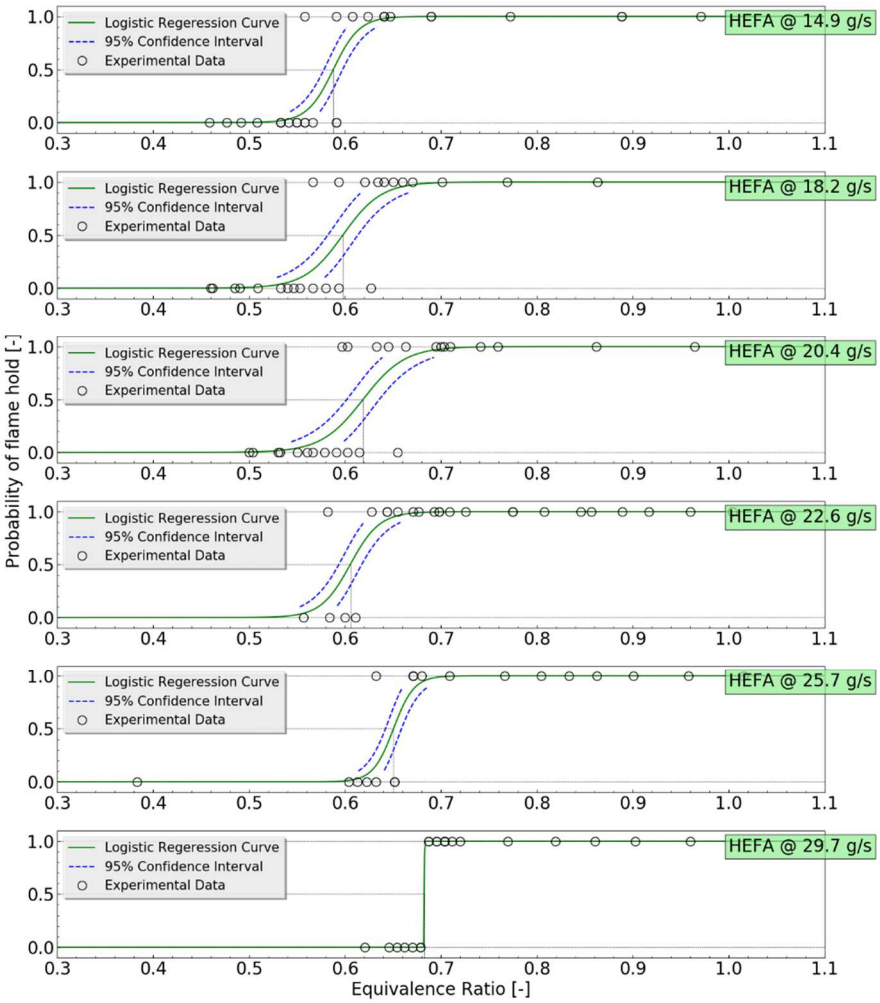

Figure 43: Regression logistic for 45° OSW for HEFA at different air flow rates

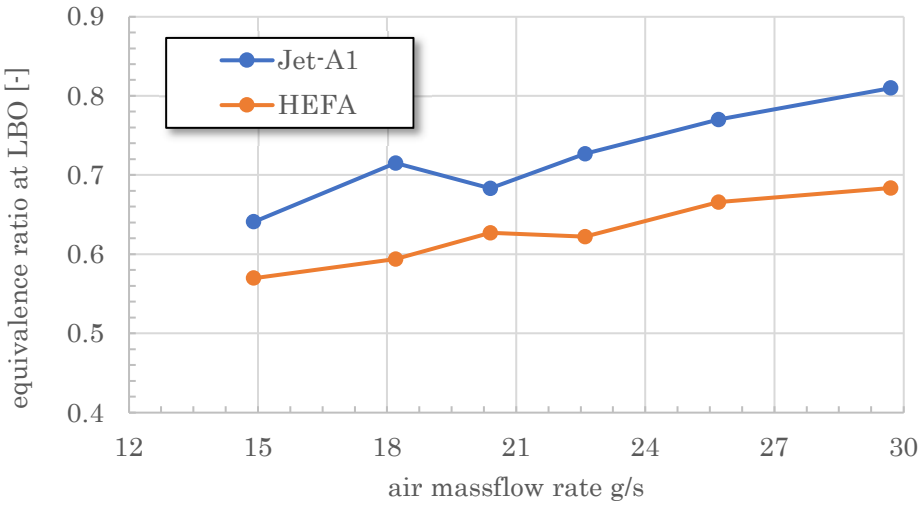

Figure 44: Comparison Jet-A1 & HEFA LBO with 45° OSW

3.3.2. LBO at high temperature and high pressure

High temperature and high-pressure experiments are strongly limited, due to the restricted access. Figure 37 showed the sequence of such an experiment. The blowout occurred with a certain delay after the hydrogen flame was cut off. It was often reported that hydrogen had a highly stabilizing quality when mixed to the fuel. This was researched and also observed by Frenillot et al. [111]. In a case of insufficient fuel flow rate, the flame started to get unstable and quickly grow in amplitude. Eventually, the flame blowout. This behavior was not observed at ambient conditions and might be attributed due to the used nozzle in these conditions. Nevertheless, similar to ambient condition, the difference between blowout and stable flame was clearly distinguishable and are summarized in Figure 45. For mapping the equivalence ratio, a second parameter was included, which represented the maximum pressure peak during combustion (equation (37)). This pressure peak analysis is often conducted in rocket engine oscillation investigations [112][113].

$$P' = 2\overline{|P_C - \bar{P}_C|} \qquad (37)$$

The average of the pressure signal is removed from the total pressure to get the dynamic pressure amplitude. The factor "2" is added to intensify the peaks. As Figure 45 shows, there is no clear contrast between the two fuels in pressure fluctuation. Nevertheless, the fuel shows clear differentiation in the LBO limit, similar to the results of ambient conditions.

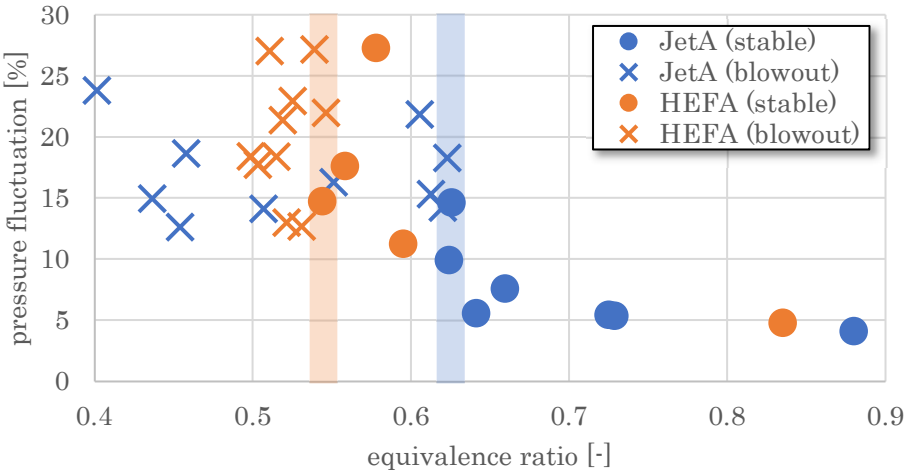

Figure 45: LBO map for 45° OSW at high temperature and high-pressure condition

3.3.3. Observation of lifted flame behavior

To further elucidate the lean blowout results, chemiluminescence images at several air flow rates were recorded. Figure 46 shows the comparison of averaged CH* images of Jet-A1 (left column) and HEFA (right column) at an equivalence ratio of 0.7 and an airflow rate of 25.7 g/s. The upper row shows the swirl flame with 45°, the middle with 60°, and the lower row with 64° outer swirler (OSW). Images for 60° and 64° OSW were taken, to support the difference in SMD measurement during combustion, especially for 64° OSW. The graph on the right side of the figure shows the lift-off height of 45° and 60° OSW. For 64° OSW the lift-off height was not specified, since as visible in the images, the flame is literally at the bottom of the combustion chamber and has therefore nearly 0 mm distance.

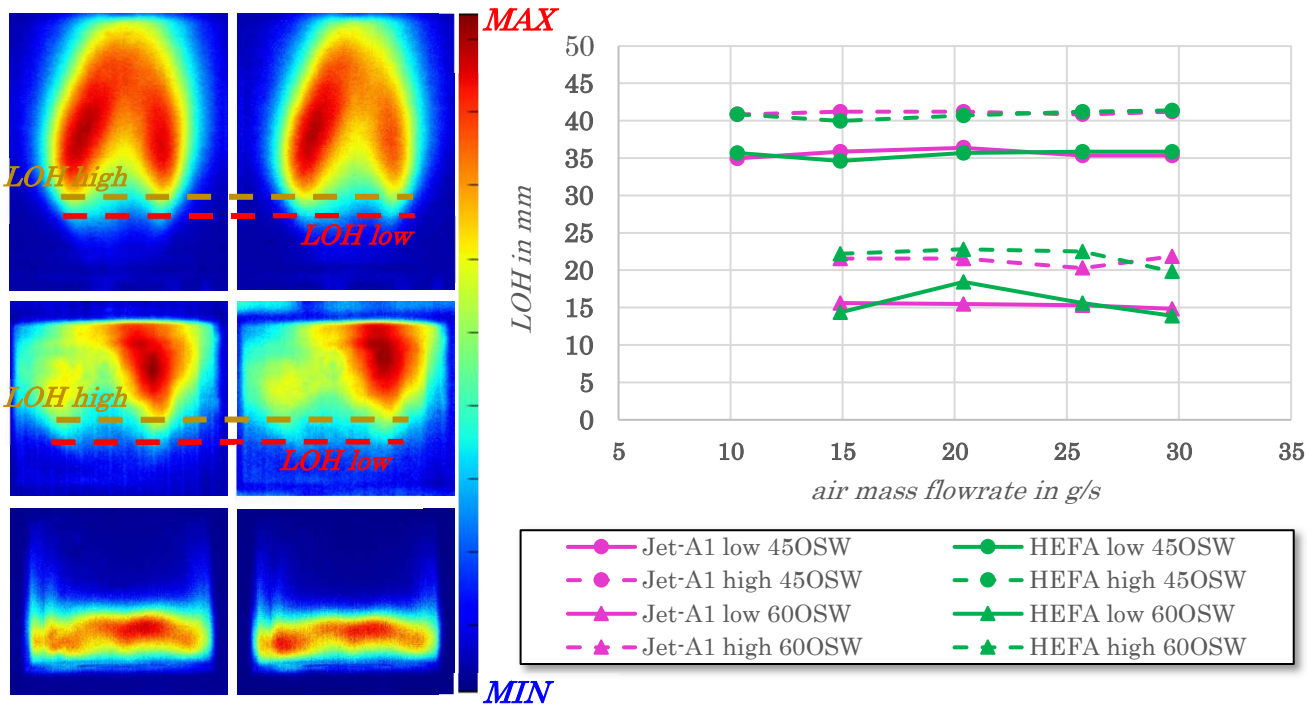

Figure 46: Lift-off height overview of HEFA and Jet-A1 at different airflow conditions and OSW

Remarkable is, that the lift-off height does not change over the whole tested range of airflow rate. Additionally, the two fuels do not show any differences in LOH. This will be further discussed in the next sub-chapter.

The average flame images in Figure 46 show, that Jet-A1 flames look a bit more voluptuous. This may come from a stronger yellow luminosity compared to the HEFA case, which originates from a

higher presence of ring-structure compounds in Jet-A1 fuel (aromatics). Referring to Table 1, HEFA has nearly no aromatic components HEFA.

Additionally, it should be noted, the LBO at higher airflow rates is above the tested condition in Figure 46. In those conditions, LBO did not appear immediately, so CH* images were still able to be recorded. What is important here is the fact, that even an operation at or below LBO has a similar lift-off height than e.g. at lower airflow rates, where the operating condition was far above LBO.

Frequency analysis:

By analyzing the pressure data at ambient condition, a peak at around 530 Hz could be found, which is shown in Figure 47. The peak is relatively small, considering the wide range of pressure signals used for the FFT analysis (2 s). The pressure images also show nearly no difference in amplitude before and after the flame was turned off, which happened in HEFA and Jet-A1 cases at the 12th second. This might indicate, the frequency has no meaningful influence on the combustion. Nevertheless, the value of the frequency indicates to be the longitudinal mode of the combustion chamber, considering one side closed of the chamber. According to literature, the frequency can be calculated with equation (38). Equation (39) represents a slightly more accurate formula for the longitudinal frequency, especially for pipes or cylinders with an open end, since the exact point of reflection of the soundwave is not at the exit plane but rather further downstream, which is compensated by the extra term "0.4D". L and D are the length and diameter of the cylinder, respectively. The expression below the square root is the sonic speed, considering the specific heat ratio γ, the gas constant R, and the temperature inside the chamber T.

$$f = \frac{n\sqrt{\gamma RT}}{2L} \qquad (38)$$

$$f = \frac{n\sqrt{\gamma RT}}{2(L + 0.4D)} \qquad (39)$$

The mentioned 530 Hz were detected at an equivalence ratio of 0.72 for HEFA and 0.84 for Jet-A1, which correspond according to Figure 58 to an adiabatic temperature of 1916 K and 2111 K,

respectively. Considering equation (39), a frequency of 530 Hz responds to a temperature of about 1140 K. Important to note is, that this temperature represents the average temperature over the whole acoustic reflecting volume, which is in this case the inside of the combustion chamber. The adiabatic temperature represents the temperature at complete combustion and might therefore be an oversimplification since e.g. heat losses near the combustor wall are not considered.

Standing wave frequency or even Helmholtz resonating frequency inside the pressure holes is above 3700 Hz (for ambient condition at high temperature up to 9000 Hz), indicating no interference with the measured value of 530 Hz.

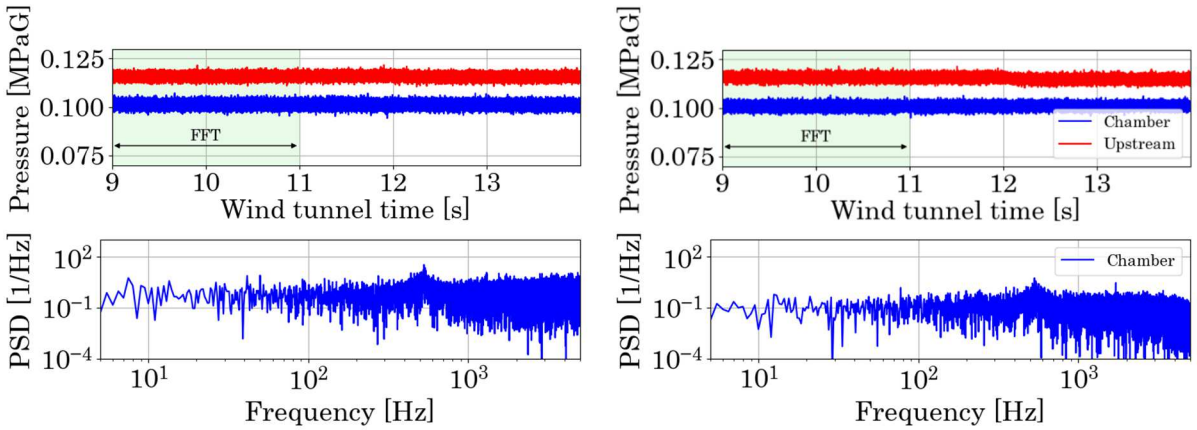

Figure 47: pressure and PSD at ambient condition with an airflow rate of 25.7 g/s, left: HEFA with φ = 0.72; right: Jet-A1 with φ = 0.84

Lift-off height high temperature and high-pressure condition:

Similar to the ambient condition, the lift-off height was also observed in the high temperature and high-pressure condition. Figure 48 compares average flames for stable equivalence ratios (meaning far away from LBO) and average flame images near Lean Blowout. 500 CH* chemiluminescence images were used to create those averages. Lift-off height was marked at 60% intensity.

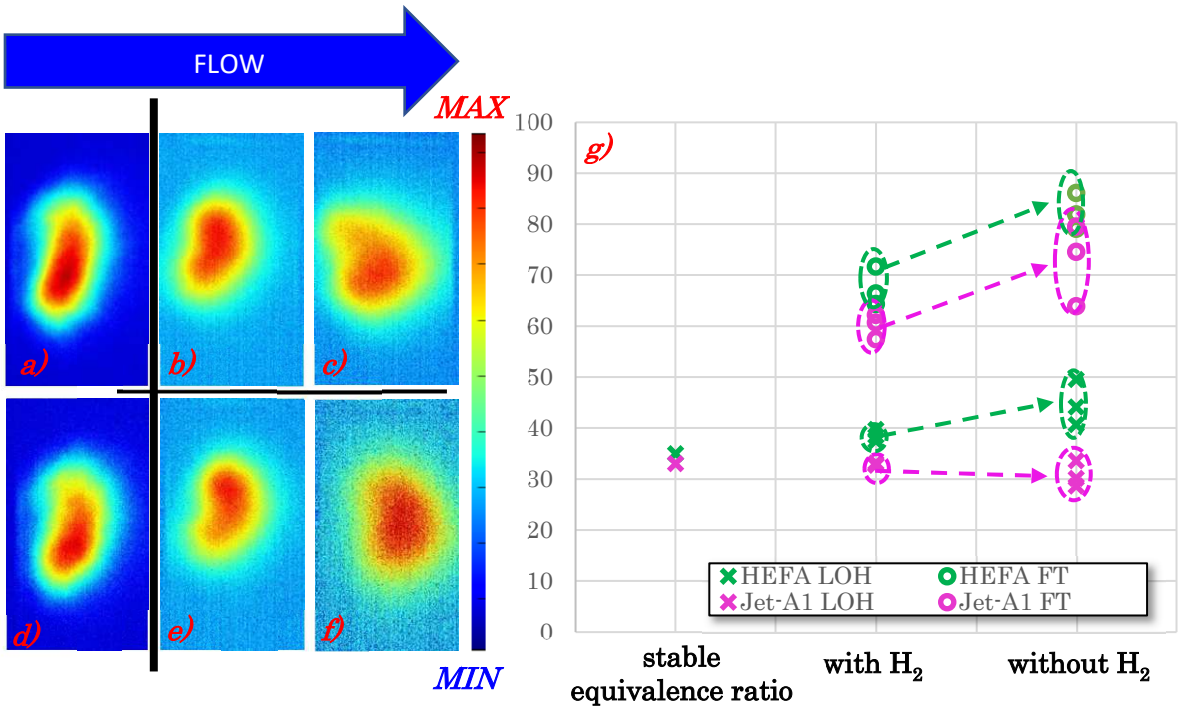

*Figure 48: Change in flame position: averaged CH*chemiluminescence, a) b) c) Jet-A1 at φ = 0.86, φ = 0.624 with and without H_2 igniter; c) d) e) HEFA at φ = 0.83, φ = 0.531 with and without H_2 igniter; g) LOH and FT of Jet-A1 and HEFA flame near LBO*

Figure 48 a) and d) show a stable condition for both fuels, indicating in g), that their lift-off height is almost identical. When looking into unstable conditions, close to LBO, the averaged image of the CH* chemiluminescence change their position. Figure 48 shows in b) and c) how the average flame moves from with hydrogen igniter to without hydrogen igniter for Jet-A1 condition at 0.624 equivalence ratio. Compared to that, figure e) and f) shows the same effect for a HEFA flame with an equivalence ratio of 0.531. A clear difference in lift-off height (LOH) and flame top (FT) is recognizable between the two fuels, which is shown on the right side of the figure for three experimental runs for each fuel. Visible is the general higher LOH for the HEFA cases. After the hydrogen igniter is cut off, the LOH even increases in cases of HEFA. The stabilizing effect of hydrogen on a kerosene flame was already shown by Frenilott et al.[111], where additional mixed hydrogen lowered the LBO of the kerosene flame. Also, the LOH was also reduced, due to the mixed hydrogen, and it was concluded, that this effect resulted from hydrogen's increased flame speed.

3.3.4. Combustion instability at high temperature and high pressure

Frequency analysis:

In this section, the combustion behavior near lean blowout and at lean blowout is shown. Figure 49 presents the appearance of fluctuation of the chamber pressure at different equivalence ratios for both researched fuels. It is shown, that with an increase in equivalence ratio, the fluctuation of pressure reduces, clearly indicating the observation of near LBO oscillation. For the description of the condition, the ratio of actual equivalence ratio to the lean blowout equivalence ratio was chosen. For the LBO equivalence ratio, the values as shown in Chapter 3.3.2 were used. The observed oscillation is strongly related to the Helmholtz frequency, created by the plenum of the combustor (upstream volume) and the outer swirler path of the injector (neck). The frequency can be calculated with the following equation:

$$f_H = \frac{c}{2\pi}\sqrt{\frac{A_0}{V_o L_{eq}}} \qquad (40)$$

where c is the sonic speed and A_0, V_0 and L_{eq} are the neck area, the bottle volume, and the length of the neck, respectively. Since the form of the swirler path is rather complicated compared to a simple bottle neck, additional adjustments to the values were necessary. Instead of just using the general length of the swirl path, a term depending on the hydraulic diameter (D) was added, to compensate for end correction. Leq can then be calculated with:

$$L_{eq} = L_n + 0.3 * D \qquad (41)$$

where L_n represents the general length of the swirl path.

The hydraulic diameter is calculated by the difference of outer and inner diameter, due to the nozzle's annular shape. The representative neck cross-section is calculated by the swirl path volume V_{swirl} and its geometrical total length L_n:

$$A_0 = \frac{V_{swirl}}{L_n} \qquad (42)$$

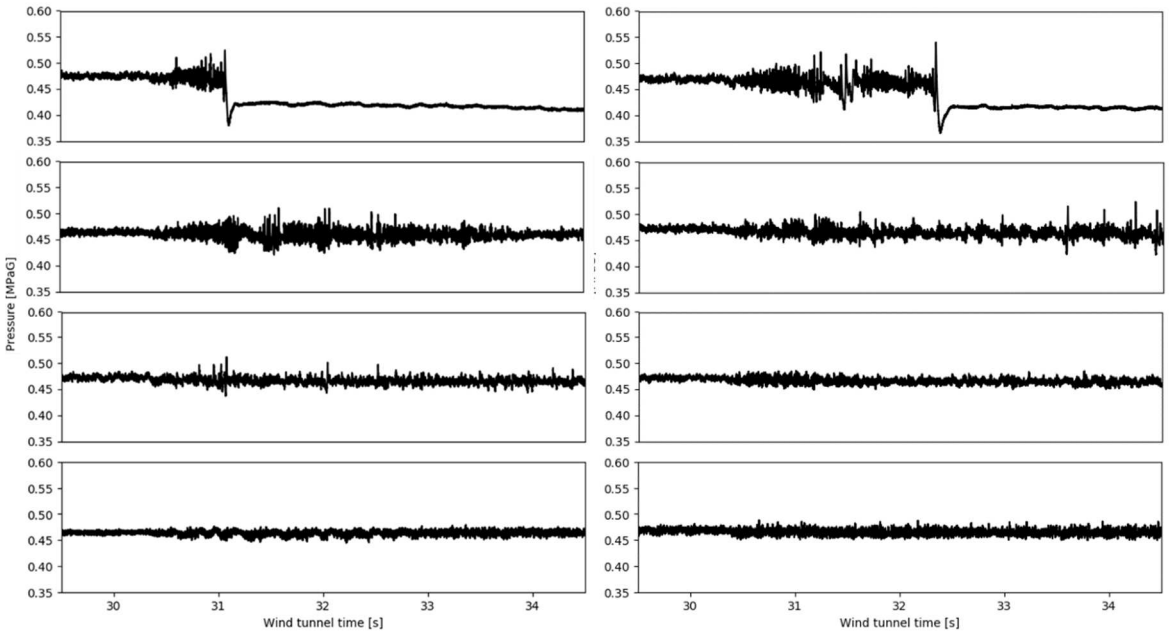

Figure 49: Route of chamber pressure to Lean Blowout: left: HEFA from top: $\frac{\varphi}{\varphi_{LBO}}$= 0.974, 1.03 , 1.09, 1.52; right: Jet-A1 from top: $\frac{\varphi}{\varphi_{LBO}}$= 0.998, 1.003, 1.16, 1.39

By applying a Fast Fourier Transform (FFT) on the pressure data shown in Figure 49 and adding the data of the upstream pressure as indicated in the schematics of Figure 36, the power spectrum density (PSD) of both pressure sensors according to the conditions in Figure 49 can be derived and shown as in Figure 50. For the graphs, the data from 30.5 to 30.98 s were used to create the PSD, to have the same amount of data of each experiment for unbiased comparison. The green line marks the Helmholtz frequency of around 120 Hz and it is visible, that both fuels exhibit a peak in the PSD near that line. The peak near 1000 Hz belongs to the 1st longitudinal frequency of the combustion chamber which corresponds to 1150 Hz and can be calculated with

$$f_L = \frac{c}{2L_{Ch}} \qquad (43)$$

where L_{Ch} is the chamber length, which is 0.384 m with the exit nozzle. Considering roughly 1936 K for 0.6 equivalence ratio (see Figure 58), the longitudinal frequency result in 1148 Hz. Further right in Figure 50 can be seen another peak at around 1760 Hz. This might be the eigenfrequency of the pressure hole since this peak could also be observed after the flame is extinguished.

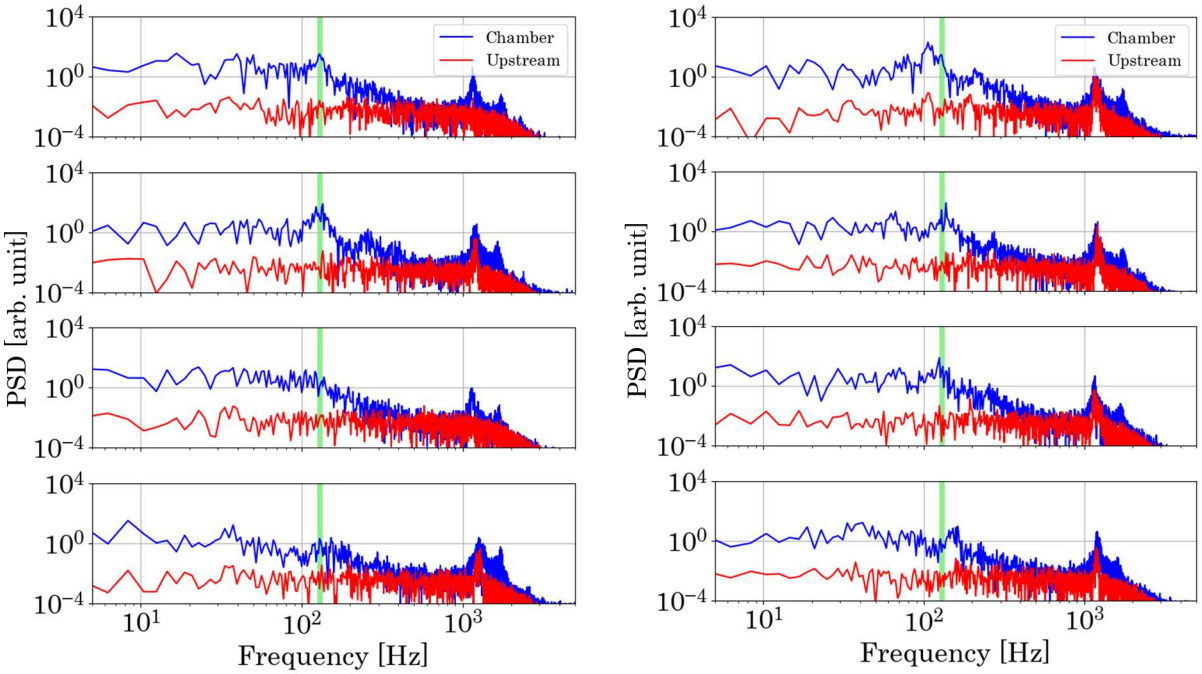

Figure 50: PSD HEFA (left) from top: $\frac{\varphi}{\varphi_{LBO}}$= 0.974, 1.03 , 1.09, 1.52; PSD Jet-A1(right) from top: $\frac{\varphi}{\varphi_{LBO}}$= 0.998, 1.003, 1.16, 1.39

The peak for Helmholtz instability reduces for HEFA with increasing equivalence ratio, though for Jet-A1 it stays in all conditions. By checking the PSD for wider time ranges, before the hydrogen igniter is turned off or even after obvious fluctuation stopped, a peak near the Helmholtz frequency can always be found, indicating, that this instability exists throughout the combustion, and is driving the Lean Blowout. Figure 50 also indicates no peak at 120 Hz for the upstream pressure transducer, indicating further, that the Helmholtz instability is created within the swirl path.

Another important aspect in Figure 50 is, that the Helmholtz peak is detectible not only at Lean Blowout condition, but also at stable condition, indicating the fluctuation is the same, but due to the strong fluctuation at LBO, best describable at this condition.

Intensity of spray and CH*chemiluminescence compared with pressure signal:

By looking into the CH*chemiluminescence images, the flame or rather the heat release rate of the flame can be observed during the reported oscillation. When comparing the heat release images with the pressure data in Figure 51, it is noticeable, that the intensity of the heat release rate (HHR) reaches its peak at the same moment, when the pressure gets to its summit, indicating the HHR and pressure are in phase and fulfill the Rayleigh criterion for inducing combustion oscillation. The first

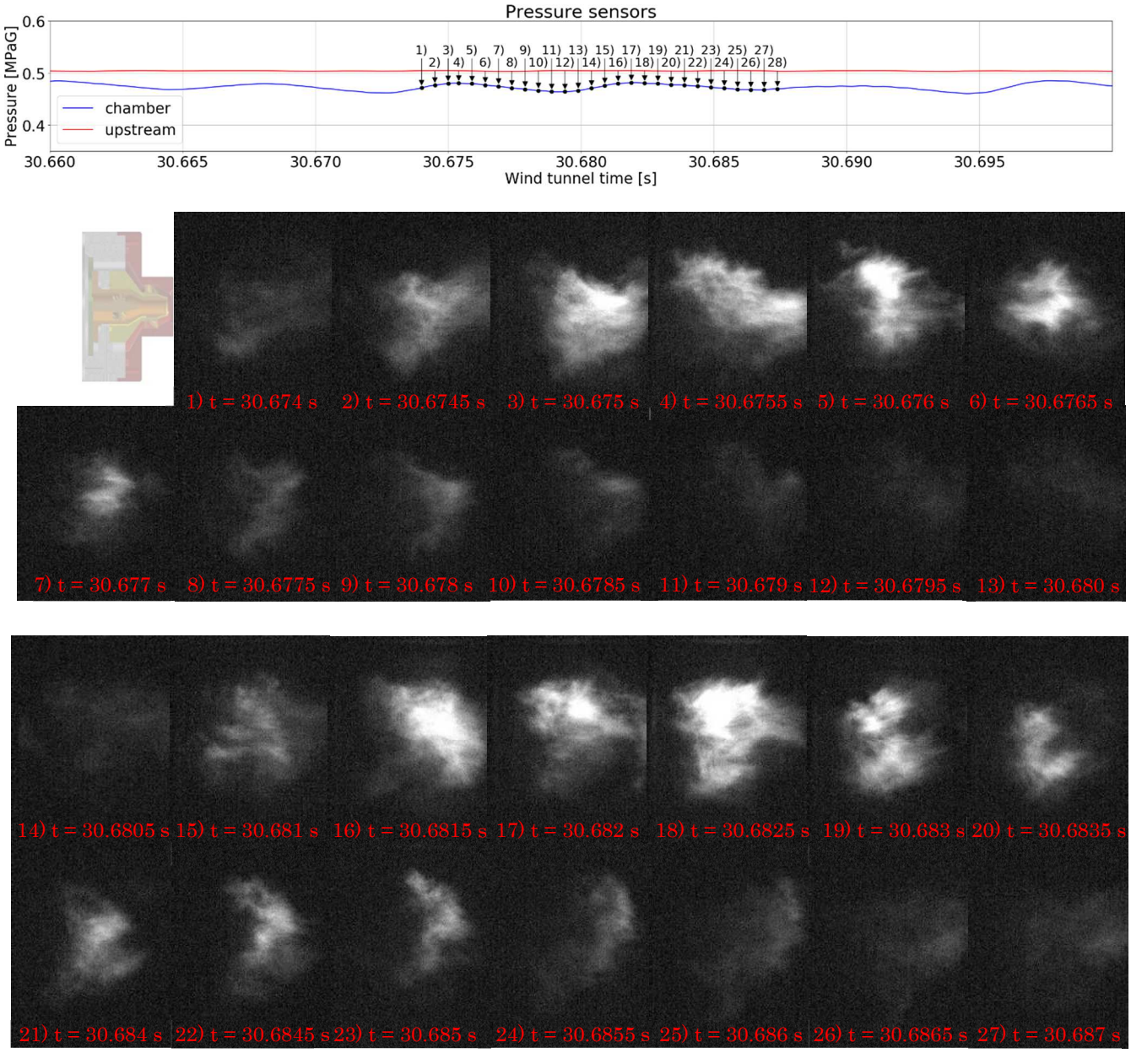

Figure 51: CH chemiluminescence fluctuation of HEFA at condition* $\frac{\varphi}{\varphi_{LBO}}$ *= 0.974*

image in the upper left corner shows the injector of the experimental setup, indicating the upstream position towards the CH*chemiluminescence images. Interesting to see is, that the high heat release rate starts further downstream and moves upstream towards the igniter with each image from 1) to 6) and the same counts from 16) to 19) in Figure 51. Then, from 7) to 12) as well as from 19) to 26), the intensity moves from upstream to downstream with decreasing intensity. Considering an airflow rate or rather an airflow velocity fluctuation reversed to the pressure oscillation, meaning a high pressure would result in a low airflow rate, and low pressure causes a high airflow rate (as in [114]), it would fit the natural behavior of a flame moving further downstream when the airflow speed increases as from 7) to 12) and 19) to 26). The possible increase in airflow speed might cause local extinction, leading to a temporary blowout or at least weak HRR. Figure 52 shows the associating fluctuation of the spray. Image 1) and 8) show a stronger spray compare to the rest and when correlating with the corresponding images in Figure 51, it seems there is a certain delay between maximum in spray and maximum in CH* chemiluminescence images.

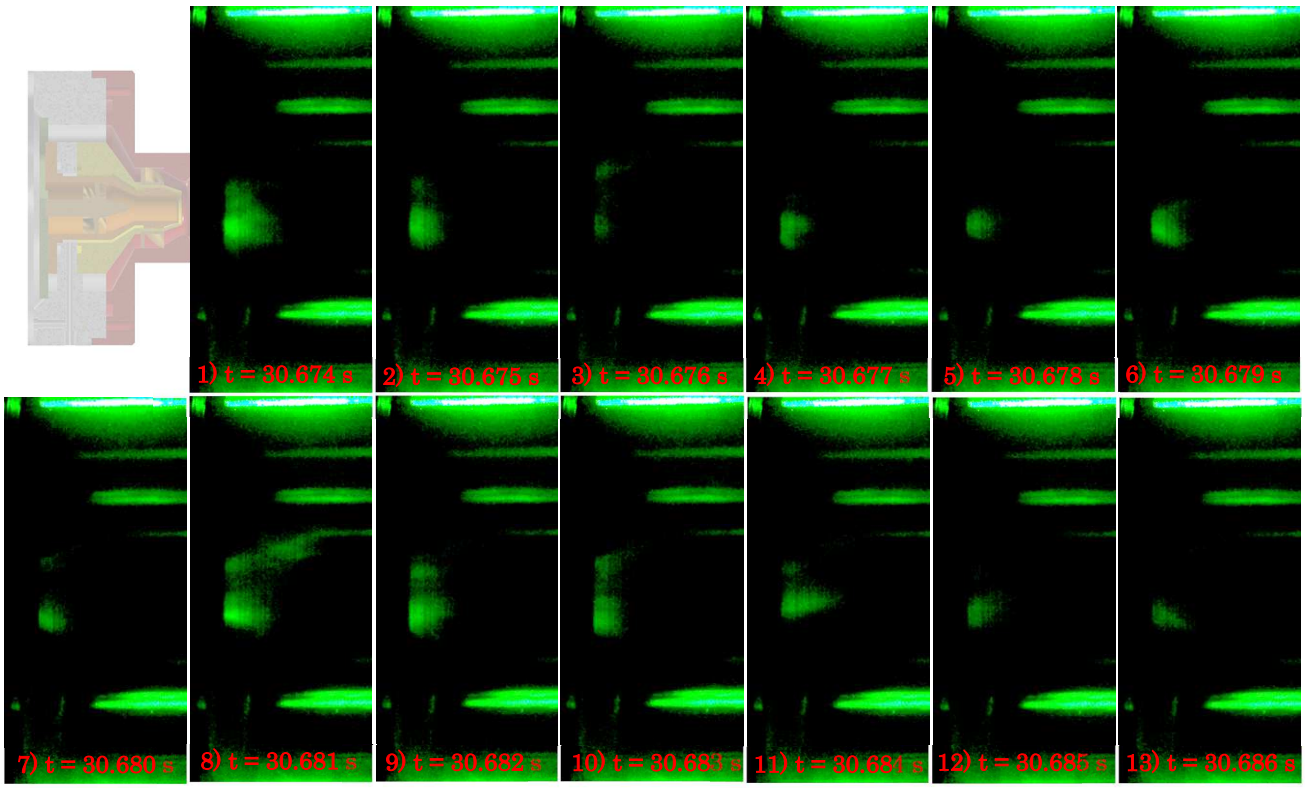

Figure 52: Spray fluctuation of HEFA at condition $\frac{\varphi}{\varphi_{LBO}} = 0.974$

As expected from Figure 49 and Figure 50 already, Jet-A1 LBO combustion shows a similar behavior as HEFA, which is presented in Figure 53. nearly two full cycles of oscillation are shown, with image 1) to 5) as well as 16) to 21) revealing the HRR moving from downstream towards the injector upstream as in the HEFA case. 6) to 12) and 22) to 27) showing an increase in lift-off height during the decrease phase of the pressure, also same to HEFA case. Figure 54 shows the corresponding spray fluctuation of the Jet-A1 flame. Comparing here spray and CH* chemiluminescence, the appearance of the

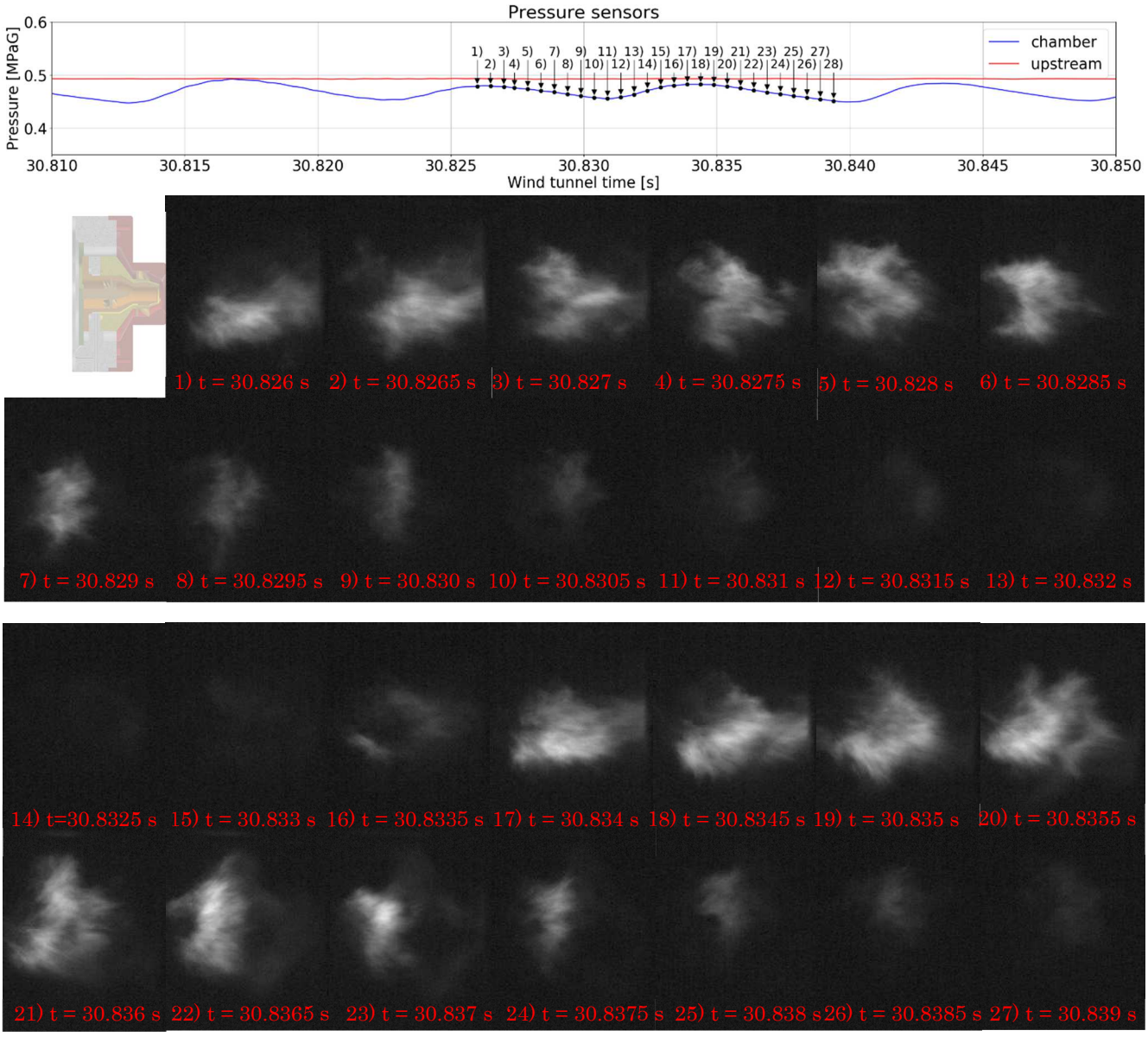

Figure 53: CH chemiluminescence fluctuation of Jet-A1 at condition* $\frac{\varphi}{\varphi_{LBO}} = 0.998$

maxima seem to be simultaneous, not delayed like in the HEFA case. The intensity of the spray reflection in the Jet-A1 case looks weaker than in the HEFA case. This comes from different laser intensities, where 4 W was used in the case of Jet-A1, and 7 W was used in the case of HEFA.

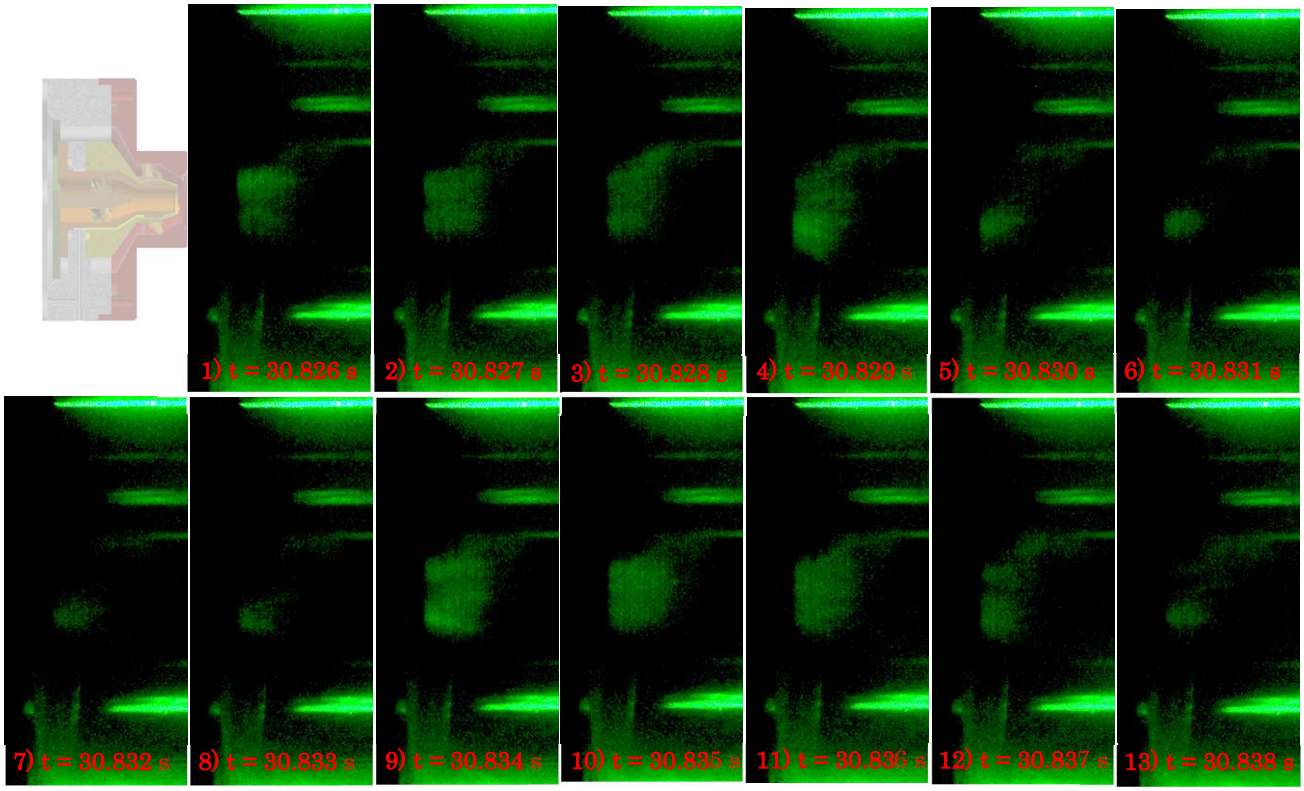

Figure 54: Spray fluctuation of Jet-A1 at condition $\frac{\varphi}{\varphi_{LBO}} = 0.998$

Figure 49 shows in both fuel cases, that the pressure peak increases towards blowout. In fact, the pressure does increase to a value above the upstream pressure in the plenum. This most likely leads to a cut-off of incoming airflow. This happened several times along the combustion oscillation process towards the LBO event for both fuels. Figure 55 shows such an event for HEFA as representation. The pressure first exhibits a reduction between the time 31.595 and 31.597 s. This reduction might cause an increase in airflow rate for a short period of time, filling up the combustion chamber with a fuel-air mixture. Therefore, slight CH* intensity is visible in the early images. In image 6) and 7), the flame starts to envelop the whole observation area. That is the point, where the chamber pressure reaches

the same value as the upstream pressure. From image 7) to 10) the HHR moves slightly towards the injector and looks like settling down at the inlet of the combustion chamber. In image 11), also where the chamber pressure crosses the inlet pressure, a flame appears at the inlet (or assumingly inlet, since the inlet is 15 mm further downstream of the observation window). Further in time, the appeared flame reduces in intensity and a certain remnant of it remains until image 16). Starting with image

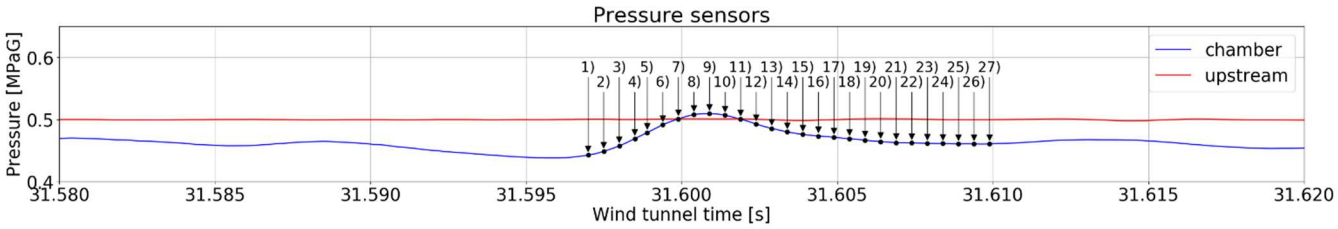

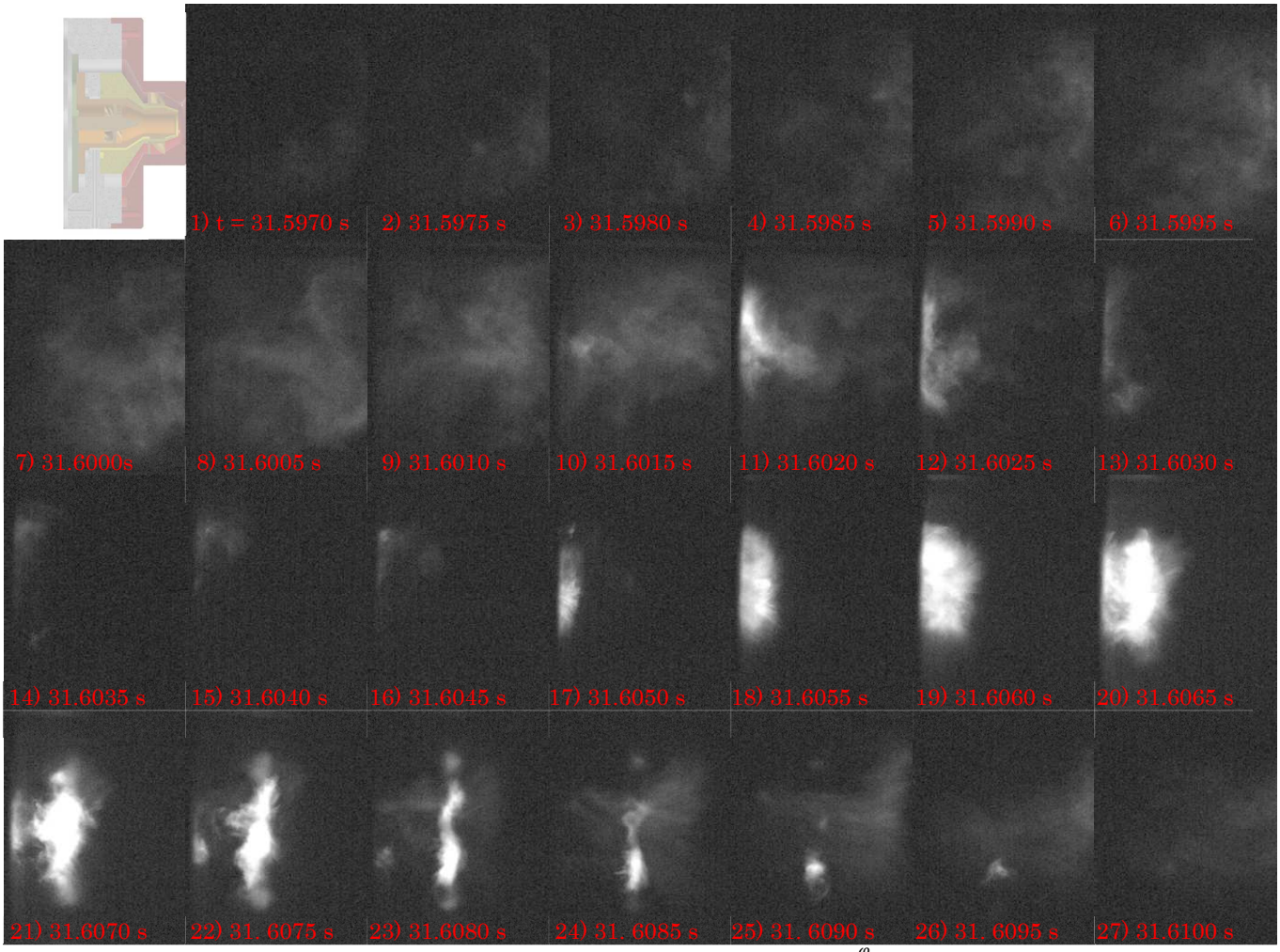

Figure 55: CH chemiluminescence precursor event at LBO condition of HEFA: $\frac{\varphi}{\varphi_{LBO}} = 0.945$*

17) a strong intensity flame appears, growing until image 19) and starts to lift-off from image 20). This flame or rather flame ring increases slowly its lift-off height with a simultaneous reduction of intensity, completely disappearing in image 27). What appears to be the cross-section of this flame ring can be seen from images 22) to 25).

By calculating the global intensity of the observation window for CH*chemiluminescence as well as the spray, both can be correlated with the pressure signal as in Figure 56. The top image shows the correlation in the HEFA case, whereas the low image shows the case for Jet-A1. Clearly visible when using HEFA is that the spray is leading towards HRR and pressure. In the case of Jet-A1, spray, CH* and pressure are almost fully aligned over the whole shown time span.

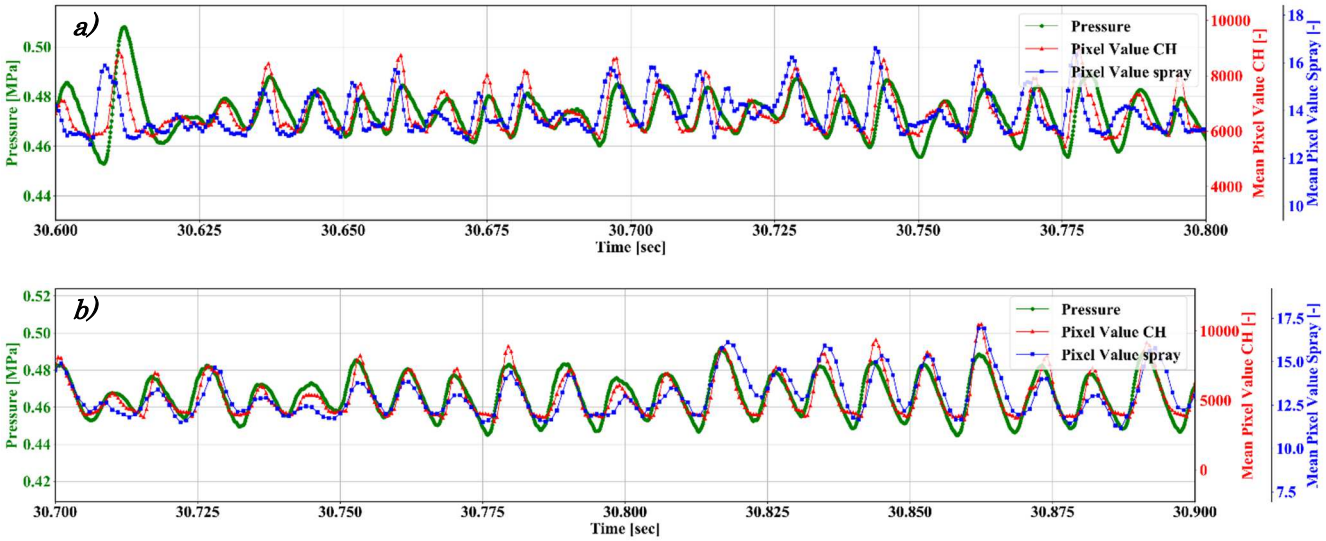

Figure 56: pressure – CH - spray correlation: a) HEFA case for* $\frac{\varphi}{\varphi_{LBO}}$ *= 0.974; b) Jet-A1 case for* $\frac{\varphi}{\varphi_{LBO}}$ *= 0.998*

Figure 57 shows the fluctuation of both fuels before blowout for the cases presented in Figure 49. In a) it can be seen, that HRR and pressure slightly lag towards spray intensity, with increasing lag towards LBO. Visible is the spray peak before the last pressure peak, having a phase lag of 180°. Similar behavior can be seen in b) for Jet-A1, though the fluctuation between CH, pressure and spray almost remain synchronic except before LBO, where spray also shows a phase lead of 180° towards

pressure. In addition, it is visible, that the pressure in both fuels experiences a growing amplitude towards the LBO point, with a simultaneous growth in periodic time (peak-to-peak time).

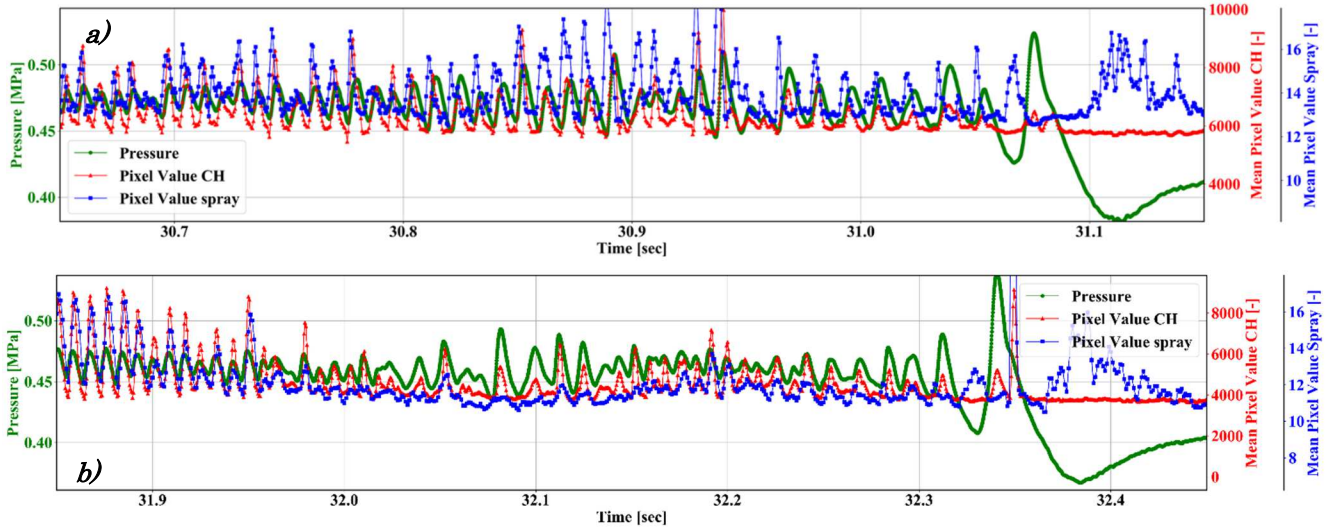

Figure 57: pressure – CH - spray correlation near LBO precursor: a) HEFA case for* $\frac{\varphi}{\varphi_{LBO}}$ *= 0.974; b) Jet-A1 case for* $\frac{\varphi}{\varphi_{LBO}}$ *= 0.998*

3.4. Discussion

3.4.1. Lean Blowout

As in the previous section visible in Figure 44 and Figure 45, HEFA seems more stable compared to Jet-A1 when it comes to "static stability" [15]. In the following, a discussion is conducted, where this difference might come from.

In equation (29), the relationship of lean blowout limit to several combustion relevant properties was shown, which was derived by Lefebvre [27]. Mellor et al. [38] implied, that the LBO limit is proportional to the reciprocal of three characteristic timescales, which he put together to the following equation:

$$\varphi_{LBO} \sim \left(\frac{1}{\tau_{chem}} + \frac{1}{\tau_{evap}} + \frac{1}{\tau_{mix}} \right)^{-1} \qquad (44)$$

These equations were used by several other authors ([49][39]) to describe their LBO behaviors over different conditions and fuel properties. By comparing Lefebvre's and Mellor's equation, it is recognizable, that they somehow correlate with each other. Lefebvre uses the mass air flow rate, which can be represented by the time scale for mixing since with air flow rate, the characteristic velocity in the combustion chamber (the inlet air velocity) increases. The evaporation time scale is connected to the droplet size and effective evaporation rate, and the chemical time scale is loosely connected to the lower calorific value. These suggestions are only a few possibilities according to Heyne et al. [17]. Recently, it was found that LBO correlates very well with the Derived Cetane Number (DCN), which is strongly connected to ignition delay time. For the evaporation timescale, typically the atomization, heat-up period, and steady-state evaporation of the droplets are considered. Atomization time is often omitted because the process happens within several µs. Also, the heat-up period is often ignored, believing, that for such small droplets, the heat-up time should be neglectable small compared to the evaporation rate. It was already shown in Chapter 2, that heat-up time causes a significant portion of the total evaporation time.

It remains an open question, what temperature values exist inside the combustor and especially near the leading edge of the flame. Nevertheless, Figure 46 showed, that there is virtually no difference between the two fuels when it comes to lift-off height, as well as the calculated adiabatic temperature in Figure 58 shows no recognizable difference in temperature between the two fuels and can be assumed similar [115]. Therefore, to use equation (29), the difference of effective evaporation rate is relatively assumed, by using the following relation:

$$\frac{\varphi_{LBOi}}{\varphi_{LBOi+1}} \sim \frac{T_{adi}}{T_{adi+1}} \sim \frac{\lambda_{effi}}{\lambda_{effi+1}} \qquad (45)$$

Effective evaporation rate was calculated in Chapter 2 and droplet measurements are as well in the same chapter. The first part of the right-hand side of equation (29) represents the combustor geometry, which can be omitted since the same combustor was used for those experiments.

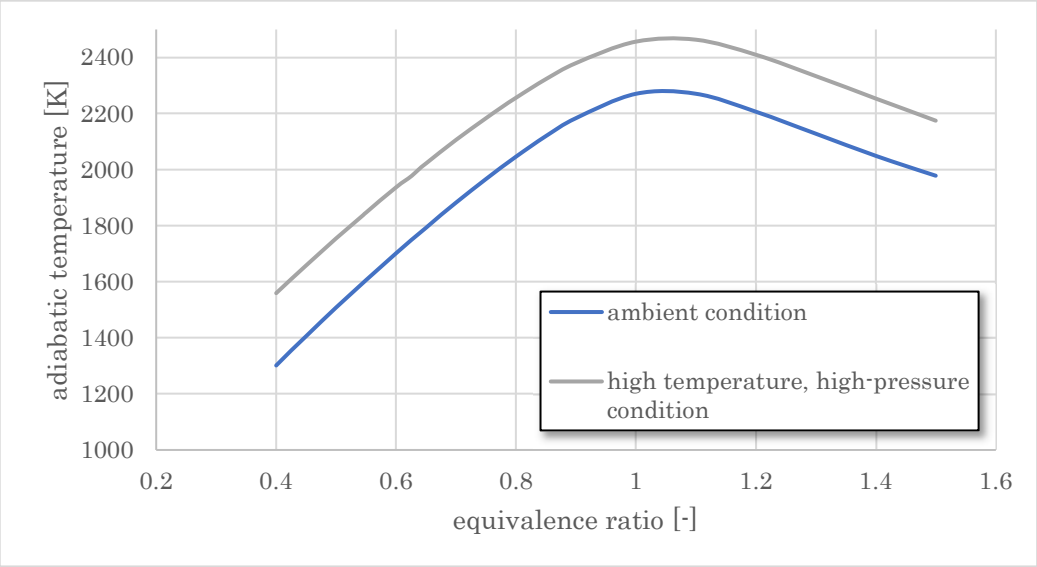

Figure 58: Adiabatic Temperature profiles

Figure 59 shows the results of equation (29) - Lefebvre's empirical model - with additional optimizations for both fuels. Lefebvre's prediction drifts off completely, almost 90° perpendicular to the perfect prediction line. This might come from the atomizer's nature. In chapter 2.4.1 was shown, that the empirical equation (21) can predict the SMD produced by the injector used in this work. SMD is reverse proportional to the air flow velocity. So by considering the droplet size squared in

equation (29), it is obvious, that the prediction drifts off by nearly 90°. Figure 59 shows, by adding an exponent of "2.6" to the air mass flow rate in both fuel cases, the prediction becomes much closer to the measurement data, but by relating the LBO values only to the air mass flow rate, the data points almost align fully, indicating, that in the non-premixed spray flame case of an airblast dual swirl prefilm injector, the lean blowout of a single fuel is linearly correlated to the mass air flow rate.

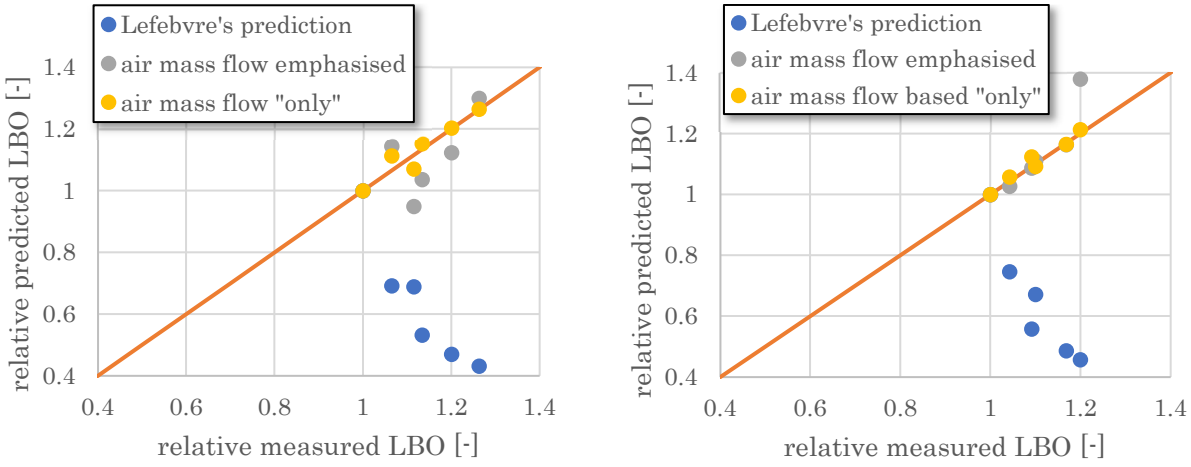

Figure 59: prediction of 45° OSW LBO behavior at ambient condition for a) Jet-A1; b) HEFA

The ratio in lean blowout between Jet-A1 and HEFA is 0.865 ±0.0277 considering the LBO results in Figure 44. Looking at the difference of effective evaporation rate in Figure 32, it is clear to be of similar value. A simplified approach of equation (29) reveals that the product of effective evaporation rate ratio and lower heat value ratio of different fuels indicate the difference in LBO limit of non-premixed ambient condition combustion (equation (46)).

$$\frac{\varphi_{LBO\_HEFA}}{\varphi_{LBO_{Jet-A1}}} \sim \frac{\lambda_{eff\_Jet-A1}}{\lambda_{eff\_HEFA}} \frac{LCV_{Jet-A1}}{LCV_{HEFA}} \qquad (46)$$

The product on the right-hand side results in 0.88 ±0.0031 considering the modeled values in Chapter 2.4.3 for effective evaporation rate and the given values for low heat values in Table 1. The calculated values in equation (46) do correlate very well, indicating the equation's usefulness when it comes to comparing different fuel's LBO limit.

3.4.2. Lift-off height and timescales

By comparing the main timescale parameters, as suggested by Plee and Mellor [38] and also used by Burger [49], the following diagram can be derived:

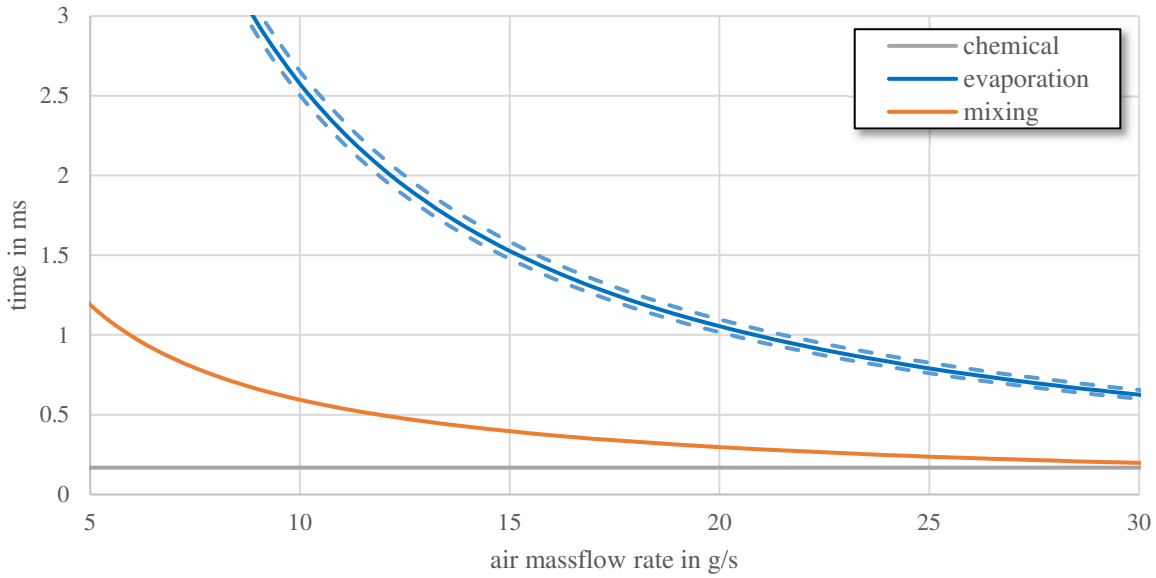

Figure 60: comparison of driving timescales in case of ambient condition

In this schematic diagram, the mixing timescale is typically described as the ratio of injector diameter divided by the air inflow velocity, so it is inverse proportional to the air mass flow rate. The chemical timescale is strongly temperature-dependent, but rather small considering the high temperature shown in Figure 58 and comparing it to ignition delay times presented in Figure A. 4 in Appendix A. In Figure 60, the temperature chosen for assuming ignition delay time and the evaporation rate is 1600 K, which is an appropriate value considering the adiabatic temperature near lean blowout according to Figure 58. With an increase in temperature, the grey line in Figure 60 would move to lower time values, increasing the distance to the evaporation timescale curve further. The evaporation rate, also strongly temperature related, is the ratio of droplet square, divided by the effective evaporation rate and therefore inverse proportional to the square of the mass flowrate considering equation (21). The reason why the graph for evaporation timescale is highest in Figure 60 is due to the droplet measurement in Chapter 2. It was shown, that at combustion, the SMD in an observation

area just below the lift-off height is near the initial SMD of the injector, suggesting that either due to the heat-up period or because of the low temperature near the injector in such a lifted flame condition, the evaporation of droplets is delayed, so that by comparing the timescales, an additional factor should be added to the evaporation timescale, which represents the distance between injector and flame leading edge. A simplified factor is lift-off height divided by injector exit velocity. As long as lift-off height is longer than the injector exit diameter, evaporation will govern the process over mixing according to the calculated timescales. Since the leading edge at lift-off height is the stabilizer of the flame, and ignition happens near that area, the chemical timescale needs to be lower than the evaporation timescale since SMD near the leading edge is similar to the initial SMD. Considering a lower temperature than the above mentioned 1600 K, the chemical and evaporation timescale curve would cross, with the chemical timescale having the higher value at high air mass flow rates. This possibility can be excluded, because, as mentioned, especially in the high air mass flow rates, droplets near the leading edge are still similar in size than compared to the initial droplets, therefore evaporation must be the ruling process in the ambient condition. The two dashed lines of the evaporation time scale represent the upper and lower limit of the quantifying error of the droplet size measurement method. Although the quantification error is relatively high for low initial droplet sizes (8.7% at 29.7 g/s air mass flow rate), the influence on the timescale does not have a significant influence on the relationship between the different timescales.

The relatively big droplets near the leading edge are most likely the reason for the stable LOH in Figure 46. The majority of those droplets will create a locally stoichiometric condition, keeping the local laminar flame speed constant, independent of the operating condition. This was suggested by Cavaliere et al. [116] already for spray flame stabilization. The review paper of Lyon [117] described five concepts for the stabilization of non-premixed flames and two mechanisms, that either a premixed flame stabilizing the non-premixed flame or that a partly premixed flame stabilizing the non-premixed flame supports the assumption stated in the above paragraph.

The confinement of the flame used in this work most likely produces an outer recirculation zone due to a rather straight injection of the 45° OSW, which is able to stabilize the flame over a wide range of

airflow rates as also suggested by Kasabov et al. [100]. Their lift-off height changed with the operational condition but at an inlet temperature high enough to cause full evaporation, which led the non-premixed spray flame to switch into prevaporized premixed mode. They concluded that lift-off height is a good indicator for the premixedness of the fuel-air mixture. In the case of a fully evaporated spray, the flame will act like a premixed gaseous flame and changes its LOH with equivalence ratio, where a high equivalence ratio closer to stoichiometry is causing a reduced LOH and an equivalence ratio close to LBO causing a high lift-off, which can be correlated to the burning velocity of the mixture as in Figure A. 1 in Appendix A. Exactly this behavior was observed in Figure 48, where the HEFA case in the high temperature and high-pressure condition changes its lift-off height over equivalence ratio, but the Jet-A1 flame remained almost stable at one height. Therefore, HEFA fully evaporates and is probably driven by the chemical timescale, where Jet-A1 continued to be stabilized by the droplets reaching the leading edge. This assumption is further supported by the results of Chapter 2, where it was shown, that HEFA has always a higher effective evaporation rate than Jet-A1.

Using equation (21) for SMD prediction with the derived parameters in Chapter 2 and a suggested air flowrate of 62 g/s at a pressure of 0.5 MPa and inlet temperature of 630 K (ρ_{air} = 2.6 kg/m^3), the SMD is suggested to be 7 µm for the steady-state condition in the high temperature and high-pressure case. Based on the measurement data, which shows an SMD of roughly 11 µm at the same airflow velocity for ambient condition and considering Lefebvre [80], which used variation in pressure and temperature to derive the semiempirical equation (21), the assumption of 7 µm for the high temperature and high-pressure condition is acceptable.

There is a small but distinguishable difference in evaporation time between the two fuels, with an increasing difference at low temperature, as shown in Figure 61. Considering the above-mentioned condition, the inlet velocity would be 88.5 m/s. With a lift-off height from Figure 48 of 33 mm, this would correspond to a convection time of 0.358 ms from injector to lift-off height. However, the lift-off height is based on 60% intensity form the CH* chemiluminescence images, which means the flame's true lift-off might be slightly lower, moving into the gap zone between Jet-A1 and HEFA, shown as

solid lines in Figure 61. Although, the statistic analysis in Chapter 2.4.4 gives no evidence, that the two fuels cause different initial droplet sizes, for the sake of completeness, an uncertainty of 3% is used for the initial droplet size for each fuel. The 3% originates from the difference in mean value from Table 4. These uncertainties are represented by the dashed lines in Figure 61. Since an increase of droplet size for HEFA and an additional decrease of droplet size for Jet-A1 causes an overlap of the uncertainty line, indicating a 6% difference of the evaporation time concerning initial droplet size. This shows, that with a measured uncertainty of 3%, the evaporation time still reflects a difference between the two fuels. It should be noted again, that according to statistics, the two fuels produce same initial droplet sizes and the uncertainty discussion only indicates a clear difference in evaporation time between the two fuels for high temperature and high-pressure case.

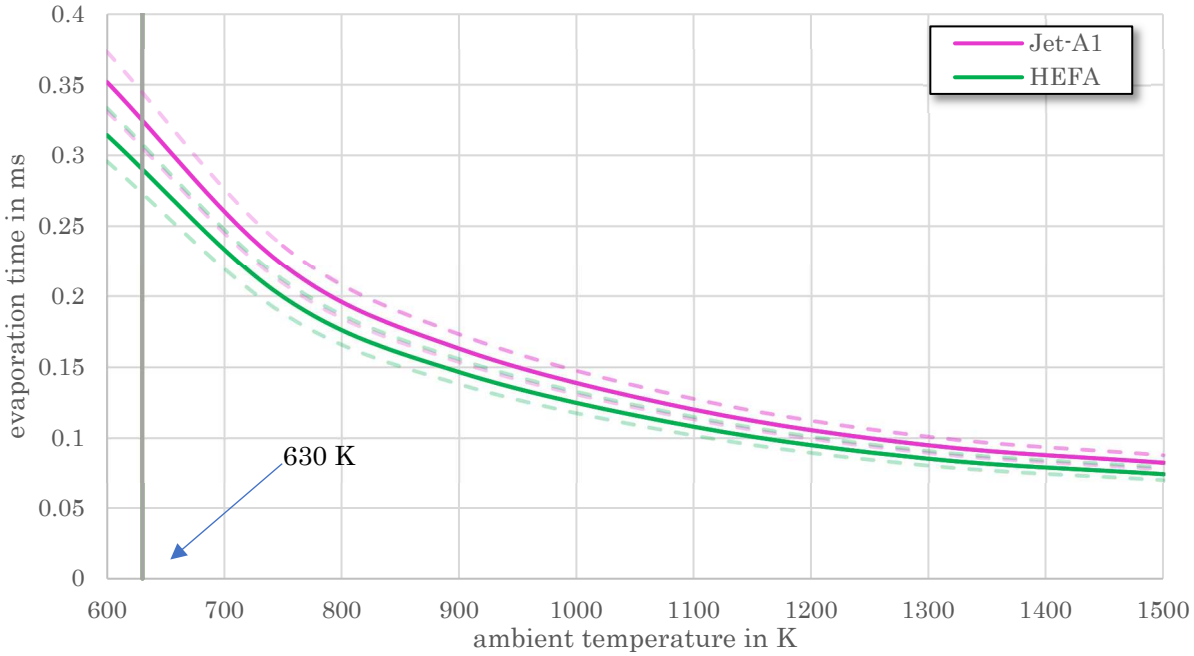

Figure 61: Evaporation time of a 7 µm droplet at different environmental temperatures at 0.5 MPa

Since HEFA may transit into a pervaporated and premixing flame and Jet-A1 most likely stays a non-premixed flame, comparing both with each other at high temperature and high-pressure condition might be obsolete. Nevertheless, the ratio of LBO values shows a value of 0.873, based on Jet-A1 LBO. The ratio of effective evaporation rate at an injection temperature of 630 K is about 0.897, based on

HEFA evaporation. Using equation (29) as a basis and add the difference of lower heat value of both fuels, which is 0.9828, a total ratio of 0.88 can be reached, which is in good agreement.

3.4.3. Characteristic combustion time

In Figure 56, a certain difference between the spray and heat release signal could be seen when comparing the two researched fuels. To further elucidate this difference, the phase shift between the spray and CH signal is formed, by using the Hilbert transformation. The Hilbert transformation turns a time-dependent signal into a complex number and forms so the phase of the original signal (for more information, see Bachmann [118]). Since the instantaneous phase angle is strongly fluctuating, because the Hilbert transformation can turn small distortions in the signal into a big phase angle, the windowed rolling correction function was used, to smoothen the signal. The result of the phase shift between spray and heat release rate can be seen in Figure 62 and Figure 63 for HEFA and Jet-A1 near lean blowout, respectively. Clearly visible between the two cases is the lower correlation factor for HEFA, revealing a longer characteristic combustion time. This is somehow contradictory to the general opinions in the literature since this kind of biofuel typically shows higher DCN (Table A.1) than

Figure 62: Phase shift of near LBO oscillation of HEFA case with $\frac{\varphi}{\varphi_{LBO}}$ *= 0.974*

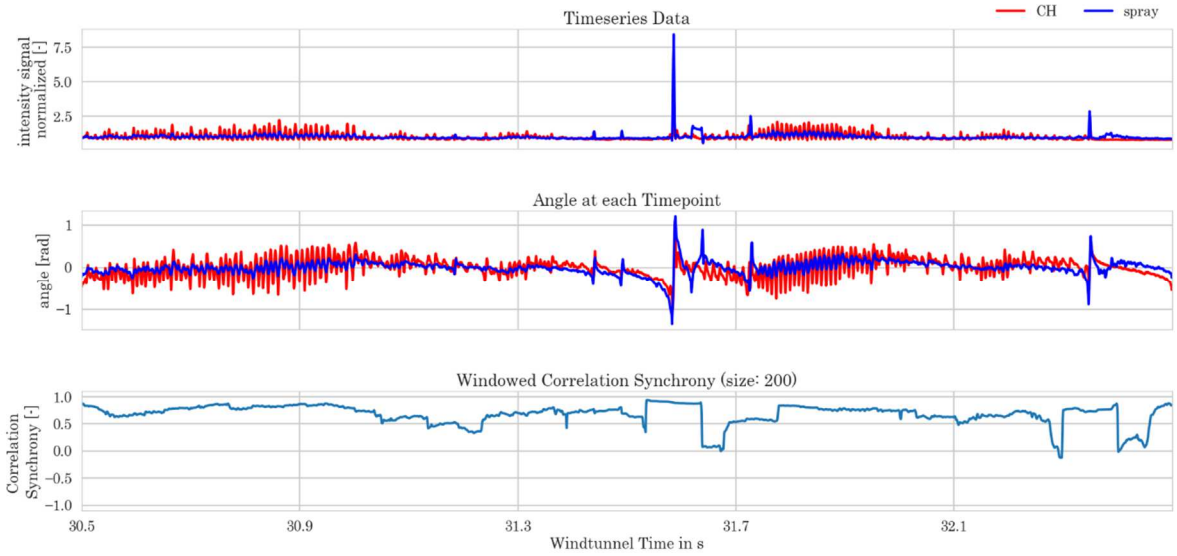

Figure 63: Phase shift of near LBO oscillation of Jet-A1 case with $\frac{\varphi}{\varphi_{LBO}} = 0.998$

conventional petroleum-derived jet fuel. By comparing several blowout cases, HEFA in general showed a lower correlation factor (Figure 64). Since the length of fluctuating period near LBO are in each case somehow individual, a relative time t_r was defined as

$$t_r = \frac{t - t_{min}}{t_{max} - t_{min}} \qquad (47)$$

with t being the general windtunnel time, t_{min} and t_{max} are the start and end times of the fluctuating stage before the lean blowout, respectively, although t_{min} was 30.5 s in all cases.

Figure 64 gives a qualitative comparison of the delay time between the two fuels. To further investigate the differences, the distances between the signal peaks of spray and CH* chemiluminescence intensity were put in contrast and were summarized in Figure 65. This figure shows the quantitative difference in characteristic combustion time between the two fuels, where most instantaneous delay times of HEFA gather in a higher value area compared to the instantaneous delay times of Jet-A1. Jet-A1's tendency towards negative values may come from the convection delay time between the injection plane and observation window plane (15 mm difference). This though does not influence the difference in delay time between HEFA and Jet-A1. For a better overview, Figure 66

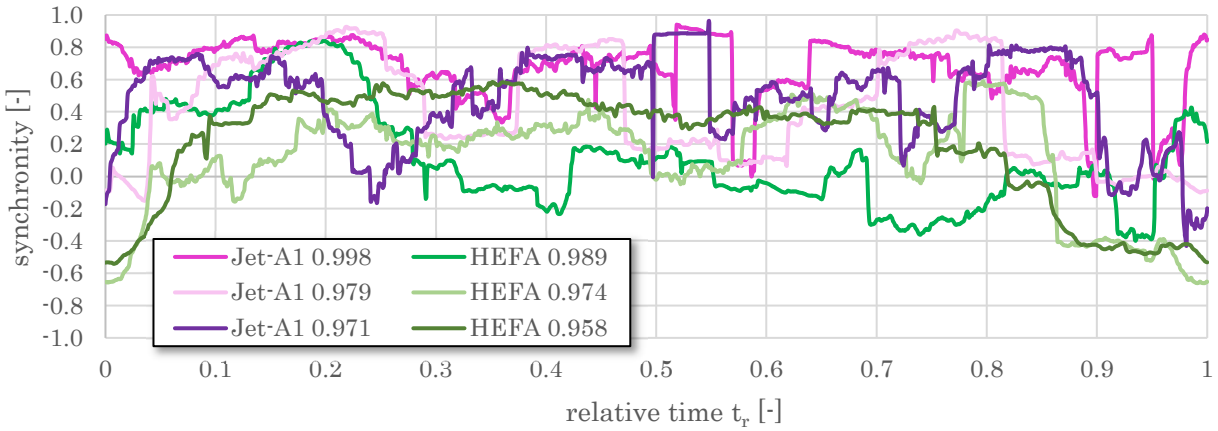

Figure 64: Correlation of spray and heat release rate for three Jet-A1 cases vs. three HEFA cases near LBO

shows the combined average of individual delay points in Figure 65 for each fuel in the form of boxplots. The data within a 0.1 s range of the relative time were combined, to form each boxplot. Since the boxes between the two fuels do not overlap, the delay time is clearly different. The wider boxes for HEFA at 0.65 and 0.95 s, as well as for Jet-A1 at 0.55, 0.65 and 0.95 s indicate lean blowout precursors as shown in Figure 55, indicating that at such precursors, but also at LBO (t_r = 0.95 s) the delay time strongly increases. The dots outside the boxplots show outliers, meaning they are outside of a 99.3% probability. These results indicate a longer characteristic combustion time for the bioderived fuel than for the petroleum-derived one. Zhang et.al. [23] mentioned, that the characteristic combustion time or ignitability of a fuel can be represented by the DCN number, but considering $DCN_{HEFA} > DCN_{Jet\text{-}A1}$,

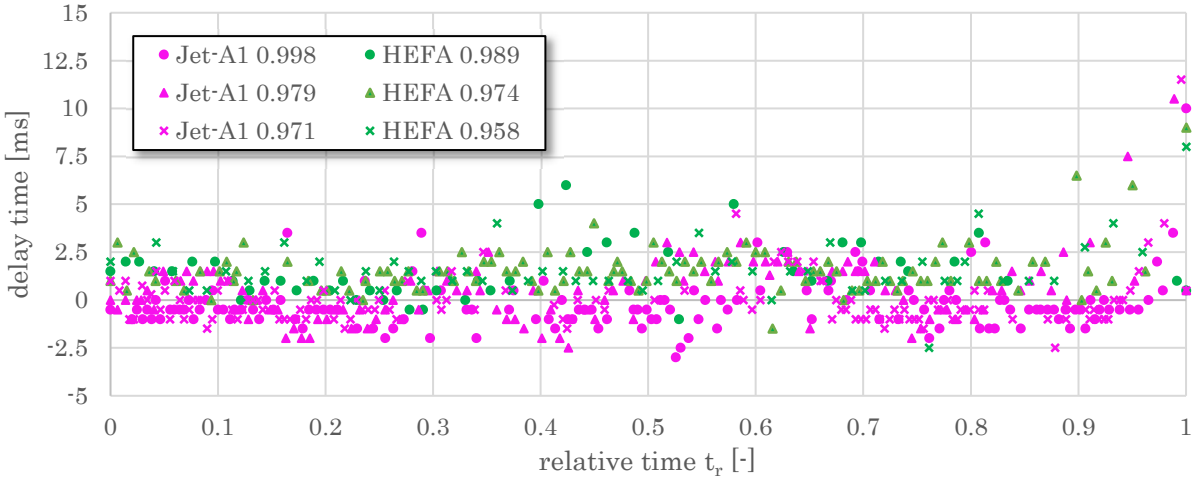

Figure 65: Instantaneous delay time for Jet-A1 and HEFA near LBO

the current results contradict this correlation. The Derived Cetane Number (DCN) is defined by the ASTM-D7668, where fuel is directly injected into a constant volume chamber and the time is measured from point of injection till the point of pressure increase. It is a condition-based parameter because it is measured in an Ignition Quality Tester (IQT) at a temperature of 555 °C (828 K) and a pressure of roughly 1.21 MPa. This is different from a typical condition in a jet engine (approx. 2000 K and in this work's case 0.5 MPa) [119]. Additionally, the fuel is injected through a single-hole pintle-type injector, whose produced SMD might be affected by the different fuel properties, as mentioned in [10] and [120]. These are indications, that the DCN might not be an appropriate value to evaluate different fuels on their characteristic combustion time unbiased.

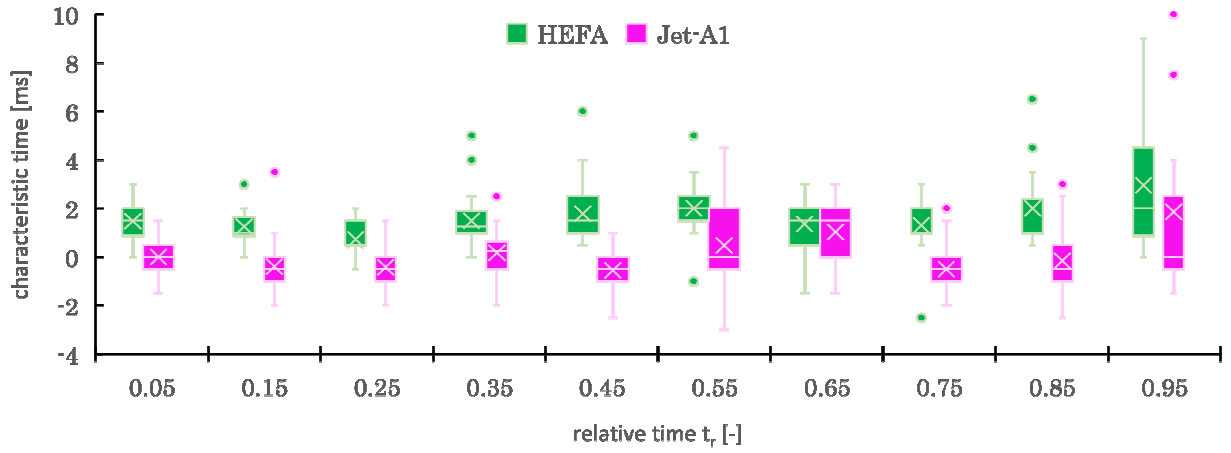

Figure 66: Local collective boxplots of the delay time between spray and CH intensity maxima for HEFA and Jet-A1*

Table 7 gives a summary of the analyzed cases near LBO. The negative delay time for Jet-A1 cases can be explained with the 15 mm gap between injection and observation window and an appropriate exit velocity of 88.5 m/s, which corresponds to a delay of 0.17 ms.

Table 7: Summary of delay time over investigated cases for HEFA and Jet-A1

	Equivalence ratio [-]	Adiabatic temp. [K]	Delay time [ms]	Averaged delay time [ms]
HEFA 0.989	0.539	1827	1.37	1.44
HEFA 0.974	0.531	1812	1.50	
HEFA 0.958	0.522	1796	1.45	
Jet-A1 0.998	0.624	1985	-0.34	-0.11
Jet-A1 0.979	0.613	1964	0.30	
Jet-A1 0.971	0.608	1955	-0.18	

According to Lefebvre and Ballal [9], the characteristic combustion time τ_{comb} is defined as

$$\tau_{comb} = \tau_{mixing} + \tau_{evaporation} + \tau_{ignition} \qquad (48)$$

where τ_{mixing} is the timescale for mixing, $\tau_{evaporation}$ the timescale for evaporation of the fuel and $\tau_{ignition}$ is the chemical timescale for ignition delay. They further stated that the evaporation rate of different fuels influences combustion delay, if there is a significant divergence in evaporation between the fuels, e.g. at least half of the periodic time of an observed oscillation. It would mean a difference of at least 3 ms in the current case (120 Hz oscillation).

Considering the difference in evaporation time between Jet-A1 and HEFA of < 0.05 ms for 600 K at 0.5 MPa (Figure 61) and declining for higher temperatures, it seems to be true, that the evaporation time itself has no direct influence on the presented difference in delay time. Considering mixing and ignition delay time, their general influence diminishes as well, with high injection velocity putting the mixing time below 0.21 ms (injector exit diameter divided by exit velocity) and high temperature (Figure 58) causing similar or lower timescales for ignition as mixing, presented in Figure 67. Using the average temperature between inlet temperature and adiabatic temperature of the individual LBO condition of HEFA and Jet-A1, the resulting temperatures will be near 1240 K and 1300 K, which lead to an ignition delay time below of 0.27 ms and 0.17 ms, respectively. The difference is an order below the actual time delay between HEFA and Jet-A1 flame. Although the temperature is only assumed

through adiabatic calculation, comparing the three main timescales, evaporation seems to be the longest and therefore dominant for this case.

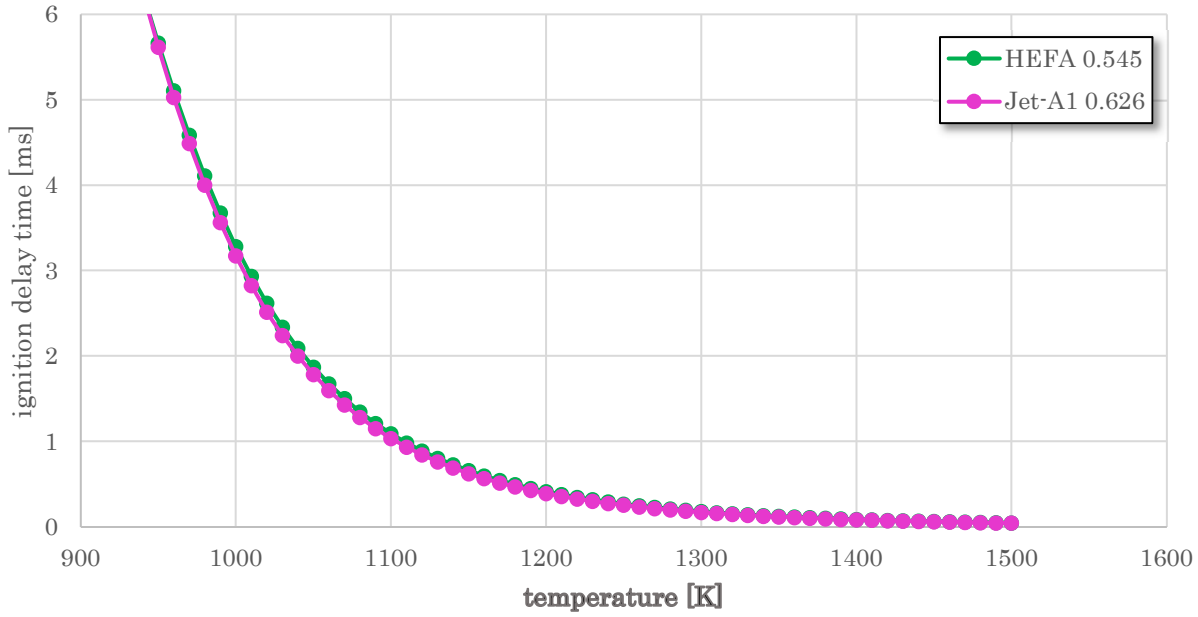

Figure 67: ignition delay time near LBO for HEFA and Jet-A1 at high pressure

Lieuwen et al. [121] researched the importance of time delay in a gas turbine combustor and emphasized the role of a convective timescale, causing instabilities by changing the distance of the injector towards the combustion chamber. However, his research focused on gaseous fuels. Nevertheless, the convective time fits the situation, where all mentioned timescales are too little to cause such a strong increase in characteristic combustion time. As shown in Figure 48, HEFA exhibit a longer lift-off height than Jet-A1 by approximately 15 mm. Considering a typical bulk flow velocity inside the combustion chamber in an area between the two lift-off-heights, the bulk flow velocity at 1840 K and 0.5 MPa would be then approximately 8.9 m/s. This would result in a convective time of 1.7 ms, which correlates very well with the measurements in Table 7. Therefore, it is suggested the characteristic combustion time is more appropriate with an added convective term for non-premixed airblast spray flames transforming into premixed flames.

This is of crucial importance, especially considering non-premixed ultra-lean combustion technologies for drop-in fuels. If a drop-in fuel causes another characteristic combustion time due to

faster evaporation, this could lead to unknown combustion instabilities (Lieuwen [121]). In addition, a different flame position might affect the combustor inner wall, which may only be designed for the original flame position. Therefore, these findings are believed to be useful for future developments.

3.4.4. Rayleigh Criterion

When looking into the phase shift between CH*chemiluminescence and pressure to explore rather or not the Rayleigh criterion is fulfilled, Figure 68 and Figure 69 show no strong difference between HEFA and Jet-A1. The Rayleigh criterion can be expressed with the following loop integral [122].

$$\oint p'\dot{q}'dt > 0 \qquad (49)$$

The integral states, that as long as the product of pressure fluctuation p' and heat release rate fluctuation $\dot{q}'$ over one period stays positive, the Rayleigh criterion is fulfilled and the combustion process possibly causes a thermo-acoustic instability. This relation results in the following requirement for the phase angle difference between pressure and heat release rate θ_{pq} ([18],[123]).

$$0° < \theta_{pq} < 90° \qquad (50)$$

Looking at Figure 69, it can be seen that all analyzed cases' phase shifts between pressure and HHR are located around a synchronity of 0.8, which corresponds to a phase angle of 36° and according to equation (50) fulfill the Rayleigh criterion. The phase angle drops immensely for cases like Jet-A1 with a relative equivalence ratio of 0.998 and 0.971 at a relative time between 0.5 and 0.6, as well as near tr = 1 for 0.998. When compared with Figure 68 and also with the phase shift between HRR and spray intensity, it is recognizable, that those drastic changes in phase angle are related to the lean blowout precursors shown in Figure 55. One explanation for such behavior might be a gathering of the combustible mixture due to fuel injection without immediate combustion, which leads to an abrupt ignition and intense rise of pressure, stopping the airflow for a moment into the chamber. As soon as the pressure drops below a certain threshold, airflow starts to move again, causing the formation, visible in Figure 55, which looks like a ring of fire, similar to a smoke ring. This phenomenon happens,

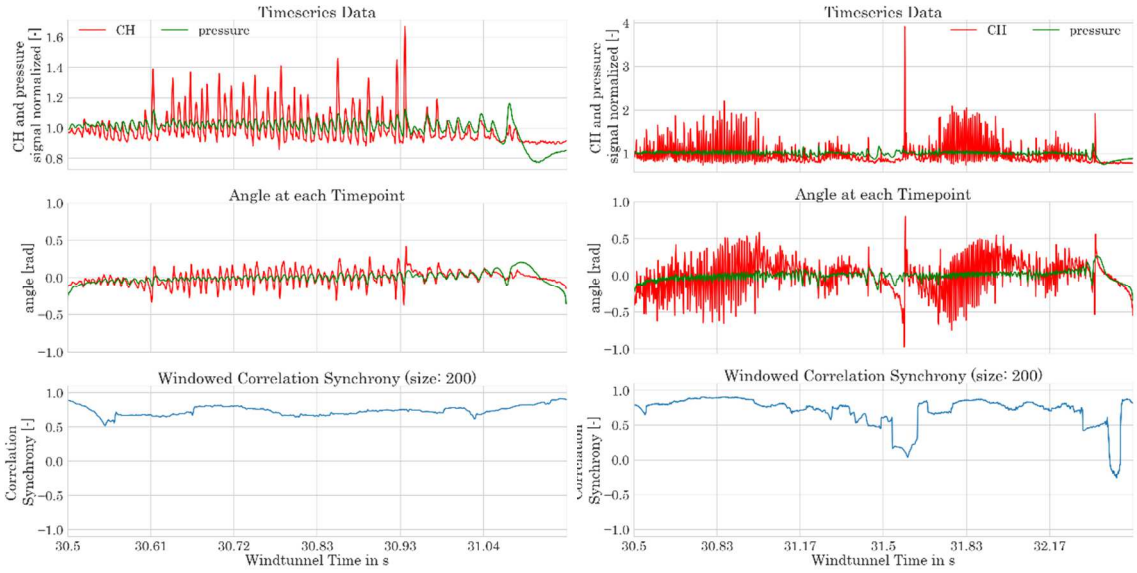

Figure 68: phase correlation between CH and pressure HEFA with* $\frac{\varphi}{\varphi_{LBO}}$ *= 0.974 (left); Jet-A1 with* $\frac{\varphi}{\varphi_{LBO}}$ *= 0.998 (right)*

if airflow in the center of the volume, in this case, the chamber axis, abruptly flows, causing a low-pressure area in the centerline. The airflow speed reduces at the edge of the injector, creating a toroidal rotation of the burning fuel, resulting in the observed fire ring. The "ring" slowly moves downstream with the incoming air and dissolves after a few frames. This phenomenon indicates that the air flow stops for a period of time, as long as the chamber pressure is above a certain threshold, especially close

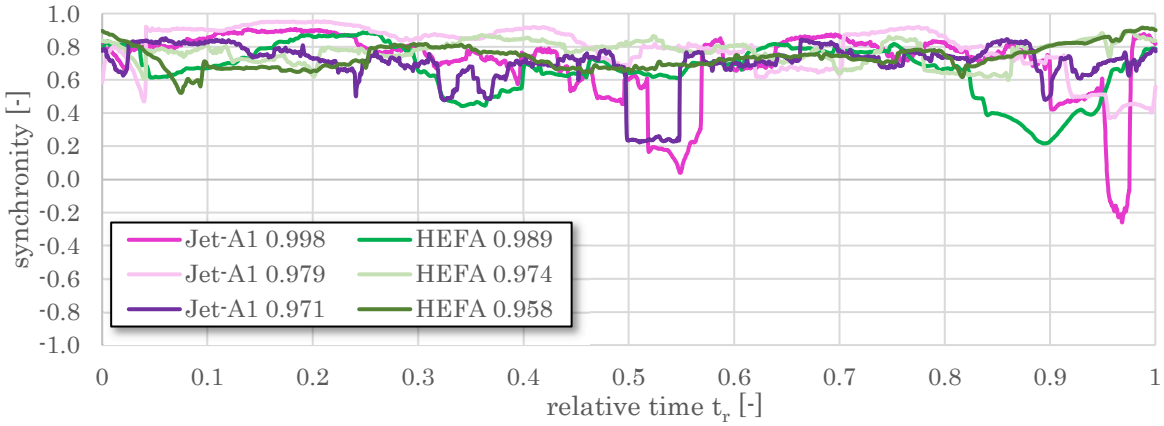

Figure 69: cumulative Rayleigh criterion for tested cases

to the plenum pressure upstream. According to the data, this phenomenon appears, when the phase shift between CH* chemiluminescence and spray increases, consequently causing a high peak in pressure and lead to the "ring" formation, therefore this appearance is termed a precursor for blowout, since it usually appears at lean blowout, but also during the instability near LBO.

To further elucidate the periodic fluctuation of both fuels, a similar approach was presented by Temme et al.[114] and Lieuwen [121] was taken. The fluctuation of the measurement data was compared with the pressure fluctuation to calculate the individual phase angles as shown in Figure 70. The connection between inlet velocity fluctuation and pressure can be simply derived from Bernoulli. Physically speaking, with an increase in pressure, the pressure drop over the injector reduces, and therefore the inlet velocity reduces as well. The reduced phase angle of 166° comes from aerodynamic dampening related to the design of the injector. Temme used an MIT model created by Ghoniem and co-workers [124], which included the following equation for momentum:

$$\frac{du_i'}{dt} = \frac{-p_c'}{\rho_i L_i} - \frac{\bar{u}_i}{L_i} u_i' \qquad (51)$$

The equation shows the connection of velocity fluctuation (left term) with pressure fluctuation (first right term) and viscous dampening (second right term). In the MIT model, a Helmholtz solver was defined, which describes Li as the neck length for the Helmholtz frequency. Temme derived then the analytical solution for the velocity fluctuation as

$$u_i' = C_1 \left[\cos \omega t - \left(\frac{\bar{u}_i}{L_i \omega}\right) \sin \omega t\right] \qquad (52)$$

and from there, the phase angle between u_i' and p_c' can be described as:

$$\phi_1 = \frac{3\pi}{2} - \left(\frac{\bar{u}_i}{L_i \omega}\right) \qquad (53)$$

The mentioned dampening term depends on the average inlet velocity (88.5 m/s), the swirl path length related to the Helmholtz instability (56.7 mm), and the fluctuating frequency (120 Hz). It was not possible to measure the air inlet velocity in this study, but Temme used a similar setup and proved a strong correlation between the approximating equation and measurement values, which give

confidence in the calculated value above. The strong fluctuating airflow velocity based on pressure oscillation indicates an equivalence ratio oscillation based on a periodical change of airflow rate. Since the fuel line had a pressure drop of 0.5 MPa and the chamber pressure fluctuated with ±0.02 MPa, it can be assumed, that the change in fuel mass flow rate is neglectable (similar to Temme).

The third graph in Figure 70 represents the fluctuation of the lift-off height. Temme explained, that the lift-off height towards the inlet velocity comes from convection, where a change at combustor inlet needs a certain time until it propagated to the flame. The inlet velocity is assumed to be the main cause for the LOH fluctuation, where a high airflow velocity pushes the flame downstream, and a low inlet velocity lets the flame move more upstream. LOH was taken and compared with the pressure fluctuation from images, such as seen in Figure 51 and Figure 53.

The fourth curve shows the fluctuation of the spray intensity. As shown above, HEFA and Jet-A1 differ strongly in delay time. The phase angle was calculated with the measured delay time between spray and heat release rate. Assuming the inlet velocity fluctuation is correct, the spray intensity movement shows a maximum near inlet velocity minimum and vice versa. This could be related to atomization. A low inlet airflow produces bigger droplets, which increases the Mie Scattering of the laser light.

The fifth curve visualizes the heat release rate fluctuation of the combustion. For both fuels, the HHR and pressure fluctuation are almost aligned, indicating the Rayleigh criterion as a good explanation for the instability caused. Lieuwen [121] stated, for equivalence ratio instability, if the timescale between the point of origin till the flame tip causes the heat release rate to be in phase with the pressure fluctuation, it is most likely the reason for the instability. Hathout et al. [124] showed, that the time lag Lieuwen mentioned is the period between the zero crossings of pressure fluctuation to the minimum of the heat release rate fluctuation, marked as τ_c in Figure 70. This comes from the flame transfer function of Hathout, which states

$$\frac{dQ_f'}{dt} = C_2 p_c'(t - \tau_c) \qquad (54)$$

Temme derived the phase angle of the heat release rate fluctuation from equation (54) to

$$\Phi_4 = \frac{\pi}{2} + \tau_c \omega \qquad (55)$$

Using the phase angle for HEFA and Jet-A1, marked in Figure 70, and an oscillating frequency of 120 Hz, this would lead to a time lag c of 5.9 and 6.1 ms, respectively. Using the average flame center location of 65 mm and 52 mm for HEFA and Jet-A1 respectively, the convection velocity for the given

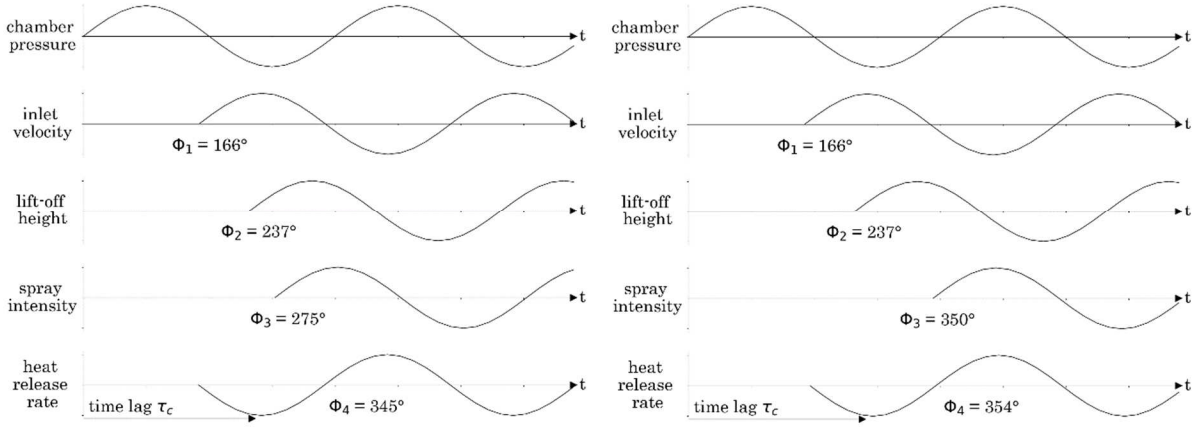

Figure 70: schematic phase differences of measured values, HEFA (left); Jet-A1 (right)

time lags would be around 11 m/s and 8.9 m/s, which is a possible value for this study's condition and design and correlates well with the previous bulk flow velocity assumption.

When looking at other experimental runs at high temperature and high-pressure condition, HEFA did not always oscillate clearly periodically. In fact, HEFA showed several times random fluctuations, where Jet-A1 always showed periodical fluctuation near LBO (indicated with Figure 71). This further confirms the above claim, that Jet-A1's combustion delay may fit the periodic time of Helmholtz instability more, compared to HEFA, whose longer characteristic combustion time at lean blowout leads to an asynchrony between spray, CH and pressure. Considering the conditions in Figure 71, it can be concluded, that due to the higher evaporation rate of HEFA, the non-premixed injection turns into a prevaporized premixed condition, result in a higher lift-off position compared to the still non-premixed Jet-A1 flame. The higher position induces additional convection to the spray – HHR

interaction, further causing random fluctuation if exceeding a threshold due to a generally more unstable position further away from the injector.

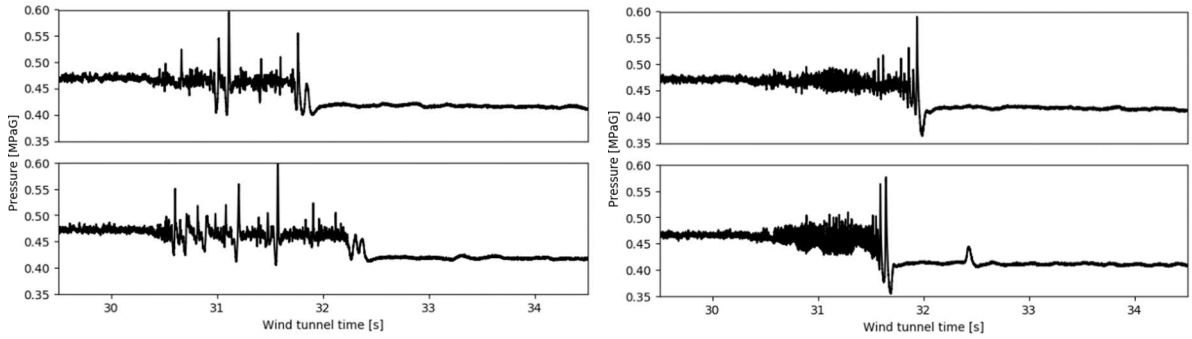

Figure 71: chamber pressure; left: HEFA LBO cases with $\frac{\varphi}{\varphi_{LBO}}$ *= 0.945 (top) and 0.963 (bottom); right: Jet-A1 cases with* $\frac{\varphi}{\varphi_{LBO}}$ *= 0.977 (top) and 0.993 (bottom)*

Chapter 4. Conclusion

This research aimed to identify experimentally differences in combustion behavior between conventional petroleum-derived Jet-A1 fuel and bioderived "Hydrotreated Esters and Fatty Acids" fuel (HEFA). Based on experimental approaches using a self-designed prefilm dual swirl airblast injector emphasis was taken on lean combustion behavior, especially lean blowout (LBO), lift-off height (LOH), and characteristic combustion time. Jet-A1 and HEFA were tested at several air mass flow rates in ambient condition and one specific air mass flow rate at high temperature and high-pressure condition. The contribution of physical properties to the combustion behavior was analyzed through atomization quality of the two liquid fuels via droplet size measurement. Therefore, a new combustion chamber was designed and manufactured, as well as a Laser Interferometry for Droplet Sizing (ILIDS) system was put together. Additionally, the evaporation rate of the two fuels was measured in a drop tower facility. For the purpose of explanation, qualitative analyses were conducted. The analyzing methods and measurement techniques are well-known, but the combination of the experimental approach and the analysis in a jet engine model combustor by using a dual swirl airblast injector had not been conducted. Following findings between the two tested fuels were found:

- In the used injector configuration, HEFA showed in all tested conditions a lower LBO limit compared to Jet-A1. The difference at ambient condition is nearly constant over a wide range of airflow rate at an average of 13.5%
- The LOH of HEFA and Jet-A1 flame showed no clear difference and is rather independent of the airflow rate and equivalence ratio in ambient condition

Evaporation rate measurement and empirical modeling showed a similar correlation to the LBO difference between the fuels. In addition, the droplet size measurement indicated similar initial droplet sizes for each tested airflow rate between Jet-A1 and HEFA, which is comparable to findings of other publications using similar fuels but different injector designs. It showed that the difference in physical properties between the two tested fuels did not influence the atomization process to a

measurable difference. Nevertheless, this further supported the strong dependency of LBO on evaporation rate at ambient condition. An additional timescale analysis also demonstrated the evaporation rate to be the dominant factor, compared to mixing and ignition delay.

Droplet measurement near the flame leading edge during combustion indicated a highly non-premixed condition, creating, according to literature, a stoichiometric mixture and stabilize the flame at the same position. Both fuels showed similar laminar flame speeds further contributing to the constant LOH. The constant height over different airflow rates suggested an outer recirculation flow, stabilizing the flame independent of inflow air velocity, though this is only an assumption and needs to be further examined via Particle Image Velocimetry.

- High-temperature and high-pressure condition showed an increased LBO difference between the two fuels compared to ambient condition, with Jet-A1 having a 12.7% higher LBO limit for the tested condition.
- HEFA flame showed an increasing average LOH with a reducing equivalence ratio, where the average Jet-A1 flame remained nearly at the same position for all tested equivalence ratios.
- Near LBO, thermo-acoustic instability with a dominant frequency corresponding to the injector's Helmholtz frequency was observed for both, HEFA and Jet-A1 flame, following Rayleigh's criterion. Although, HEFA was more prone to chaotic fluctuation.
- Comparing the global light intensities of Mie scattering of the spray with the heat release rate of CH* chemiluminescence, HEFA showed a 1.55 ms longer characteristic combustion time than Jet-A1.

Similar to ambient condition, the advantageous LBO behavior of HEFA was correlated to a higher evaporation rate. The increased difference is suggested to stem from chemical properties, with the difference in lower heat value correlating well to this variance. The increased lift-off height for HEFA indicates a transition from non-premixed to premixed flame also due to its higher evaporation rate. The increased distance from the injector leads to additional convection from the fuel-air-mixture to the flame, which causes the prolonged characteristic combustion time for HEFA. The higher time delay

for HEFA can cause the response of other frequencies if such exist in the combustor or test facility, or as in the present case, lead to chaotic fluctuation.

One of the original contributions to knowledge of this work is for one the droplet size measurement of Jet-A1 and HEFA in a dual swirl prefilm airblast injector, which has, to the author's knowledge, not been conducted before. The used droplet size measurement system had its limitations, especially for highly dense spray as in the high temperature and high-pressure condition. It is suggested to optimize the system by using different lenses to increase accuracy and measurement increment.

The second original contribution to knowledge is the measurement of the characteristic combustion time during oscillating combustion in a model jet engine combustor with a dual swirl prefilm airblast injector. Although the literature suggests that biofuel like HEFA has a shorter characteristic combustion time due to its faster ignition response and higher evaporation rate, measurements presented in this thesis show the opposite. It is suggested, to further investigate this phenomenon by using single-component fuels with properties to decouple evaporation rate and chemical advantage as in the case of HEFA.

The important message of this work is, that attention needs to be paid to future ultra-lean combustion technologies using multi-fuel injection systems. This thesis showed that a slight difference in evaporation rate between conventional and drop-in fuel can lead to a change in flame position, as well as response time between injection and flame at near jet engine conditions. In the worst case, thermal stress at unwanted areas inside the combustor or a different response in combustion fluctuation leading to serious damage of the combustor are the results. Therefore, in designing such future technologies, utmost care needs to be taken to secure safe operation.

References

[1] M. Kaltschmitt, *Biokerosene - Status and Prospects*. Springer Berlin Heidelberg, 2017.

[2] D. R. Reddy and C. Lee, "AN OVERVIEW OF LOW-EMISSION COMBUSTION RESEARCH AT NASA GLENN," in *Proc. ASME Turbo Expo 2016*, 2016.

[3] D. Dunn-Rankin and P. Therkelsen, Eds., *Lean Combustion - Technology and Control*, 2nd ed. Elsevier, 2016.

[4] Y. Liu, X. Sun, V. Sethi, D. Nalianda, Y. G. Li, and L. Wang, "Review of modern low emissions combustion technologies for aero gas turbine engines," *Prog. Aerosp. Sci.*, vol. 94, no. November 2016, pp. 12–45, 2017.

[5] C. K. Law, *Combustion Physics*. Cambridge University Press, 2006.

[6] S. R. Turns, *An Introduction to Combustion - Concepts and Applications*, 2nd ed. McGraw-Hill Book Co, 2000.

[7] X. Ren, X. Xue, K. B. Brady, C. J. Sung, and H. C. Mongia, "Fundamental investigations for lowering emissions and improving operability," *Propuls. Power Res.*, vol. 7, no. 3, pp. 197–204, 2018.

[8] S. K. Dhanuka, J. E. Temme, J. F. Driscoll, and H. C. Mongia, "Vortex-shedding and mixing layer effects on periodic flashback in a lean premixed prevaporized gas turbine combustor," *Proc. Combust. Inst.*, vol. 32, no. 2, pp. 2901–2908, 2009.

[9] A. H. Lefebvre and D. R. Ballal, "Chapter 7 - Combustion Noise," in *Gas Turbine Combustion - Alternative Fuels and Emissions*, 3rd ed., CRC Press, 2010, pp. 293–313.

[10] A. H. Lefebvre and V. G. McDonell, *Atomization and sprays*. 2017.

[11] L. S. Christensen and S. L. Steely, "Monodisperse Atomizers for Agricultural Aviation Applications," 1980.

[12] Y. Huang and V. Yang, "Dynamics and stability of lean-premixed swirl-stabilized combustion," *Prog. Energy Combust. Sci.*, vol. 35, pp. 293–364, 2009.

[13] Y. Huang and V. Yang, "Effect of swirl on combustion dynamics in a lean-premixed swirl-

stabilized combustor," *Proc. Combust. Inst.*, vol. 30, pp. 1775–1782, 2005.

[14] D. Durox *et al.*, "Flame dynamics of a variable swirl number system and instability control," *Combust. Flame*, vol. 160, pp. 1729–1742, 2013.

[15] T. C. Lieuwen, "The Gas Turbine Handbook: Static and Dynamic Combustion stability," *Gas Turbine Handb.*, p. 7, 2006.

[16] E. E. Peiffer, J. S. Heyne, and M. Colket, "Characteristic timescales for lean blowout of alternative jet fuels in four combustor rigs," in *2018 Joint Propulsion Conference*, 2018.

[17] J. S. Heyne *et al.*, "Year 3 of the National Jet Fuels Combustion Program: Practical and Scientific Impacts," in *AIAA Aerospace Sciences Meeting, 2018*, 2018.

[18] T. C. Lieuwen and V. Yang, *Combustion instabilities in gas turbine engines: operational experience, fundamental mechanisms and modeling*, vol. 210, no. 3. 2005.

[19] T. Poinsot, "Prediction and control of combustion instabilities in real engines," *Proc. Combust. Inst.*, vol. 36, no. 1, pp. 1–28, 2017.

[20] N. Syred, "A review of oscillation mechanisms and the role of the precessing vortex core (PVC) in swirl combustion systems," *Prog. Energy Combust. Sci.*, vol. 32, no. 2, pp. 93–161, 2006.

[21] K. Oberleithner, M. Stöhr, S. H. Im, C. M. Arndt, and A. M. Steinberg, "Formation and flame-induced suppression of the precessing vortex core in a swirl combustor: Experiments and linear stability analysis," *Combust. Flame*, vol. 162, no. 8, pp. 3100–3114, 2015.

[22] R. Mawhood, E. Gazis, S. de Jong, R. Hoefnagels, and R. Slade, "Production pathways for renewable jet fuel: a review of commercialization status and future prospects," *Biofuels, Bioprod. Biorefining*, 2016.

[23] C. Zhang, X. Hui, Y. Lin, and C. J. Sung, "Recent development in studies of alternative jet fuel combustion: Progress, challenges, and opportunities," *Renew. Sustain. Energy Rev.*, vol. 54, pp. 120–138, 2016.

[24] W.-C. Wang *et al.*, "Review of Biojet Fuel Conversion Technologies," 2016.

[25] E. Corporan *et al.*, "Chemical, thermal stability, seal swell, and emissions studies of alternative jet fuels," *Energy and Fuels*, vol. 25, no. 3, pp. 955–966, 2011.

[26] K. S. Venkataramani, "Aviation fuel property effects on altitude relight," Ohio, Cleveland, 1987.

[27] A. H. Lefebvre, "Fuel effects on gas turbine combustion-ignition, stability, and combustion efficiency," *J. Eng. Gas Turbines Power*, vol. 107, no. 1, pp. 24–37, 1985.

[28] D. R. Ballal and A. H. Lefebvre, "Ignition and Flame Quenching of Quiescent Fuel Mists," *Proc. R. Soc. A*, vol. 364, pp. 277–294, 1978.

[29] C. A. Moses and P. N. J. Roets, "Properties, Characteristics, and Combustion Performance of Sasol Fully Synthetic Jet Fuel," *J. Eng. Gas Turbines Power*, vol. 131, no. 041502, pp. 1–17, 2009.

[30] D. Fyffe, J. Moran, K. Kannaiyan, R. Sadr, and A. Al-sharshani, "Effect of GTL-like Jet Fuel Composition on GT Engine Altitude Ignition Performance – Part I: Combustor operability," in *Proceedings of ASME Turbo Expo 2011*, 2011, pp. 1–10.

[31] N. Rock *et al.*, "Reacting Pressurized Spray Combustor Dynamics, Part 1. Fuel Sensitivities and Blowoff Characterization," in *Proceedings of ASME Turbo Expo 2016*, 2016, pp. 1–14.

[32] J. Grohmann, B. Rauch, T. Kathrotia, W. Meier, and M. Aigner, "Investigation of differences in lean blowout of liquid single-component fuels in a gas turbine model combustor," in *Propulsion and Energy Forum*, 2016, pp. 1–17.

[33] V. Burger, A. Yates, and C. Vilijoen, "Influence of Fuel Physical Properties and Reaction Rate on Threshold Heterogeneous Gas Turbine Combustion," in *Proceedings of ASME Turbo Expo 2012*, 2012.

[34] N. Rock, I. Chterev, B. Emerson, S. H. Won, J. Seitzman, and T. Lieuwen, "Liquid fuel property effects on lean blowout in an aircraft relevant combustor," *J. Eng. Gas Turbines Power*, vol. 141, no. 7, 2019.

[35] N. Rock, I. Chterev, B. Emerson, J. Seitzman, and T. Lieuwen, "Blowout sensitivities in a liquid fueled combustor: Fuel composition and preheat temperature effects," in *Proceedings of the ASME Turbo Expo 2017*, pp. 1–11.

[36] N. Rock, B. Emerson, J. Seitzman, and T. C. Lieuwen, "Dynamics of Spray Flames under Near-Lean Blowoff Conditions," in *AIAA Scitech 2019 Forum*, 2019, pp. 1–16.

[37] A. M. Mellor, "SEMI-EMPIRICAL CORRELATIONS FOR GAS TURBINE EMISSIONS , IGNITION , AND FLAME STABILIZATION," *Prog. Energy Combust. Sci.*, vol. 6, pp. 347–358, 1980.

[38] S. L. Plee and A. M. Mellor, "Characteristic time correlation for lean blowoff of bluff-body-stabilized flames," *Combust. Flame*, vol. 35, pp. 61–80, 1979.

[39] D. C. Bell, J. S. Heyne, S. H. Won, and F. L. Dryer, "The impact of preferential vaporization on lean blowout in a referee combustor at figure of merit conditions," *Am. Soc. Mech. Eng. Power Div. POWER*, vol. 1, pp. 1–11, 2018.

[40] S. H. Won *et al.*, "Predicting the global combustion behaviors of petroleum-derived and alternative jet fuels by simple fuel property measurements," *Fuel*, vol. 168, pp. 34–46, 2016.

[41] H. Fujiwara, S. Nakaya, M. Tsue, and K. Okai, "Innovations in Sustainable Energy and Cleaner Environment," in *Green Energy and Technology*, A. K. Gupta, A. De, S. K. Aggarwal, A. Kushari, and A. Runchal, Eds. 2020.

[42] C. J. Wijesinghe and B. Khandelwal, "Impact of alternative fuel on gas turbine noise, vibration and instability," *AIAA Scitech 2019 Forum*, no. January, pp. 1–7, 2019.

[43] F. Chen, C. Ruan, T. Yu, W. Cai, Y. Mao, and X. Lu, "Effects of fuel variation and inlet air temperature on combustion stability in a gas turbine model combustor," *Aerosp. Sci. Technol.*, vol. 92, pp. 126–138, 2019.

[44] T. C. Lieuwen, V. McDonell, E. Petersen, and D. A. Santavicca, "Fuel Flexibility Influences on Premixed Combustor Blowout , Flashback , Autoignition , and," *J. Eng. Gas Turbines Power*, vol. 130, no. 011506, pp. 1–10, 2008.

[45] A. Ni, W. Polifke, and F. Joos, "THERMO-ACOUSTIC INSTABILITY IN SEQUENTIAL COMBUSTION," in *Proceedings of ASME Turboexpo 2000*, pp. 1–9.

[46] J. Bae, S. Jeong, and Y. Yoon, "Acta Astronautica Effect of delay time on the combustion instability in a single-element combustor," *Acta Astronaut.*, vol. 178, pp. 783–792, 2021.

[47] C. Ruan *et al.*, "Experimental study on combustion stability characteristics in liquid-fueled gas turbine model combustor: Fuel sensitivities and flame/flow dynamics," *Fuel*, vol. 265, p. 116973,

2020.

[48] D. Shin, A. J. Bokhart, N. S. Rodrigues, P. E. Sojka, J. P. Gore, and R. P. Lucht, "Nonreacting Spray Characteristics for Alternative Aviation Fuels at Near-Lean Blowout Conditions," *J. Propuls. Power*, vol. 36, no. 3, pp. 323–334, 2020.

[49] Victor Burger, "The Influence of Fuel Properties on Threshold Combustion in Aviation Gas Turbine Engines," 2017.

[50] M. M. Tareq, R. A. Dafsari, S. Jung, and J. Lee, "Effect of the physical properties of liquid and ALR on the spray characteristics of a pre-filming airblast nozzle," *Int. J. Multiph. Flow*, vol. 126, 2020.

[51] D. Sivakumar, R. Sakthikumar, B. N. Raghunandan, J. T. C. Hu, S. K. Puri, and A. K. Jain, "Atomization characteristics of Camelina-based alternative aviation fuels discharging drom dual-orifice injector," *J. Eng. Gas Turbines Power*, vol. 137, no. 8, pp. 1–11, 2015.

[52] S. Nakaya, K. Fujishima, M. Tsue, M. Kono, and D. Segawa, "Effects of droplet diameter on instantaneous burning rate of isolated fuel droplets in argon-rich or carbon dioxide-rich ambiences under microgravity," *Proc. Combust. Inst.*, vol. 34, no. 1, pp. 1601–1608, 2013.

[53] Y. C. Liu, Y. Xu, M. C. Hicks, and C. T. Avedisian, "Comprehensive study of initial diameter effects and other observations on convection-free droplet combustion in the standard atmosphere for n-heptane, n-octane, and n-decane," *Combust. Flame*, vol. 171, pp. 27–41, 2016.

[54] B. J. Wood, H. Wise, and S. H. Inami, "Heterogeneous combustion of multicomponent fuels," *Combust. Flame*, vol. 4, pp. 235–242, 1960.

[55] S. S. Sazhin, M. Al Qubeissi, R. Kolodnytska, A. E. Elwardany, R. Nasiri, and M. R. Heikal, "Modelling of biodiesel fuel droplet heating and evaporation," *Fuel*, vol. 115, pp. 559–572, 2014.

[56] L. Chen, G. Li, and B. Fang, "Droplet evaporation characteristics of aviation kerosene surrogate fuel and butanol blends under forced convection," *Int. J. Multiph. Flow*, vol. 114, pp. 229–239, 2019.

[57] A. Miglani, S. Basu, and R. Kumar, "Insight into instabilities in burning droplets," *Phys. Fluids*, vol. 26, no. 3, 2014.

[58] G. A. E. Godsave, “Studies of the combustion of drops in a fuel spray-the burning of single drops of fuel,” *Symp. Combust.*, vol. 4, no. 1, pp. 818–830, 1953.

[59] D. B. Spalding, “The combustion of liquid fuels,” *Symp. Combust.*, vol. 4, no. 1, pp. 847–864, 1953.

[60] J. S. Chin and A. H. Lefebvre, “Effective values of evaporation constant for hydrocarbon fuel drops,” in *Proceedings of the 20th Automotive Technology Development Contractor Coordination Meeting*, 1982, pp. 325–331.

[61] H. Fujiwara *et al.*, “バイオジェット燃料を用いた小型ガスタービンのエンジン試験,” *Gasturbine Soc. Japan*, vol. 44, no. 3, pp. 182–188, 2016.

[62] K. Okai, H. Fujiwara, M. Makida, and K. Shimodaira, “The effect of the fuel change from petroleum kerosene to HEFA alternative jet fuel on the number of nvPM emission of an RQL gas turbine combustor,” in *AIAA Scitech 2019 Forum*, 2019, no. 1, pp. 1–10.

[63] K. Okai, H. Fujiwara, M. Makida, and K. Shimodaira, “The effect of the fuel change from petroleum kerosene to HEFA alternative jet fuel on the emission of an RQL gas turbine combustor under high pressure and high temperature conditions,” in *AIAA Scitech 2020 Forum*, 2020, pp. 1–15.

[64] H. Iida, “ダブルスワールインジェクタによる旋回流噴霧火炎の CH*化学発光画像を用いた独立成分分析,” The University of Tokyo, 2018.

[65] J. M. Beer and N. A. Chigier, *Combustion Aerodynamics*. Wiley Publishing Co., 1972.

[66] S. Candel, D. Durox, T. Schuller, J.-F. Bourgouin, and J. P. Moeck, “Dynamics of Swirling Flames,” *Annu. Rev. Fluid Mech.*, vol. 46, pp. 147–173, 2014.

[67] S. Sivasegaram and J. H. Whitelaw, “The influence of swirl on oscillations in ducted premixed flames,” *Combust. Flame*, vol. 85, pp. 195–205, 1991.

[68] G. König, K. Anders, and A. Frohn, “A new light-scattering technique to measure the diameter of periodically generated moving droplets,” *J. Aerosol Sci.*, vol. 17, no. 2, pp. 157–167, 1986.

[69] A. R. Glover, S. M. Skippon, and R. D. Boyle, “Interferometric laser imaging for droplet sizing:

a method for droplet-size measurement in sparse spray systems," *Appl. Opt.*, vol. 34, no. 36, pp. 8409–8421, 1995.

[70] M. Maeda, T. Kawaguchi, and K. Hishida, "Novel interferometric measurement of size and velocity distributions of spherical particles in fluid flows," *Meas. Sci. Technol.*, vol. 11, no. 12, pp. L13–L18, 2000.

[71] R. Ragucci, A. Cavaliere, and P. Massoli, "Drop Sizing by Laser Light Scattring Exploiting Intensity Angular Oscillation in the mie regime," *Part. Part. Syst. Charact.*, vol. 7, pp. 221–225, 1990.

[72] S. Pu, "Développement de méthodes interférométriques pour la caractérisation des champs de particules," 2005.

[73] H. C. Van de Hulst, *Light Scattering by Small Particles*. NewYork: John Wiley & Sons, 1957.

[74] P. Salman, H. Ishikawa, S. Nakaya, and M. Tsue, "Evaporation Rate Measurement of n-Decane by ILIDS in a Turbulent Swirling Flow," in *12th Asia-Pacific Conference on Combustion*, 2019.

[75] G. Naka, "レーザー干渉画像法を用いたダブルスワールバーナ火炎中の燃料噴霧粒径の測定," 2017.

[76] C. Holmes *et al.*, "Monitoring Water Contamination in Jet Fuel Using Silica-Based Bragg Gratings," *IEEE Sens. J.*, vol. 19, no. 8, pp. 2984–2990, 2019.

[77] S. Ando, Y. Wu, S. Nakaya, and M. Tsue, "Droplet combustion behavior of oxidatively degraded methyl laurate and methyl oleate in microgravity," *Combust. Flame*, vol. 214, pp. 199–210, 2020.

[78] G. Charalampous and Y. Hardalupas, "Numerical evaluation of droplet sizing based on the ratio of fluorescent and scattered light intensities (LIF / Mie technique)," *Appl. Opt.*, vol. 50, no. 9, pp. 1197–1209, 2011.

[79] A. E. Saufi *et al.*, "An experimental and CFD modeling study of suspended droplets evaporation in buoyancy driven convection," *Chem. Eng. J.*, vol. 375, 2019.

[80] A. H. Lefebvre, "Airblast atomization," *Prog. Energy Combust. Sci.*, vol. 6, no. 3, pp. 233–261, 1980.

[81] K. P. Shanmugadas, S. R. Chakravarthy, R. N. Chiranthan, J. Sekar, and S. Krishnaswami, "Characterization of wall filming and atomization inside a gas-turbine swirl injector," *Exp. Fluids*, vol. 59, no. 151, 2018.

[82] L.-P. Hsiang and G. M. Faeth, "Near-limit drop deformation and secondary breakup," *Int. J. Multiph. Flow*, vol. 18, no. 5, pp. 635–652, 1992.

[83] M. Aigner and S. Wittig, "Swirl and Counterswirl Effects in Prefilming Airblast Atomizers," *J. Eng. Gas Turbines Power*, vol. 110, pp. 105–110, 1988.

[84] S. Dehaeck and J. Van Beeck, "Designing a maximum precision interferometric particle imaging set-up," *Exp. Fluids*, vol. 42, pp. 767–781, 2007.

[85] R. S. Witte and J. S. Witte, "Chapter 14: t Test for Two Independent Samples," in *Statistics*, 11th Editi., Hoboken: John Wiley & Sons, 2017, pp. 245–267.

[86] Y. C. Liu, A. J. Savas, and C. T. Avedisian, "The spherically symmetric droplet burning characteristics of Jet-A and biofuels derived from camelina and tallow," *Fuel*, vol. 108, pp. 824–832, 2013.

[87] K. M. Watson, "Prediction of Critical Temperatures and Heats of Vaporization," *Ind. Eng. Chem.*, vol. 23, no. 4, pp. 360–364, 1931.

[88] M. R. Riazi, *Characterization and Properties of Petroleum Fractions*, 1st ed. Philadelphia, USA, 2005.

[89] M. R. G. Zoby, S. Navarro-Martinez, A. Kronenburg, and A. J. Marquis, "Evaporation rates of droplet arrays in turbulent reacting flows," *Proc. Combust. Inst.*, vol. 33, no. 2, pp. 2117–2125, 2011.

[90] R. T. Imaoka and W. A. Sirignano, "Vaporization and combustion in three-dimensional droplet arrays," *Proc. Combust. Inst.*, vol. 30, no. 2, pp. 1981–1989, 2005.

[91] F. Akamatsu, Y. Miutani, M. Katsuki, S. Tsushima, and Y. D. Cho, "Measurement of the local group combustion number of droplet clusters in a premixed spray stream," *Symp. Combust.*, vol. 26, no. 1, pp. 1723–1729, 1996.

[92] H. Lienemann and J. S. Shrimpton, "Timescale considerations for internal combustion engine

sprays," *Proc. ILASS Eur.*, no. September, pp. 1–6, 2002.

[93] H. Yan, S. Zhang, and X. Yu, "Dynamics character of swirling flame investigated by OH and CH2O planar laser-induced fluorescence," in *5th International Symposium on Laser Interaction with Matter*, 2018, no. 11046.

[94] V. McDonell, *Lean combustion in gas turbines*. Elsevier Inc., 2016.

[95] V. Nori and J. Seitzman, "Evaluation of Chemiluminescence as a Combustion," in *46th AIAA Aerospace Sciences Meeting and Exhibit*, pp. 1–14.

[96] H. N. Najm, P. H. Paul, C. J. Mueller, and P. S. Wyckoff, "On the Adequacy of Certain Experimental Observables as Measurements of Flame Burning Rate," *Combust. Flame*, vol. 113, pp. 312–332, 1998.

[97] Y. Ikeda, J. Kojima, T. Nakajima, F. Akamatsu, and M. Katsuki, "MEASUREMENT OF THE LOCAL FLAMEFRONT STRUCTURE OF TURBULENT PREMIXED FLAMES BY LOCAL CHEMILUMINESCENCE," *Proc. Combust. Inst.*, vol. 28, pp. 343–350, 2000.

[98] M. J. Bedard, T. L. Fuller, S. Sardeshmukh, and W. E. Anderson, "Chemiluminescence as a diagnostic in studying combustion instability in a practical combustor," *Combust. Flame*, vol. 213, pp. 211–225, 2020.

[99] S. Sardeshmukh, M. Bedard, and W. Anderson, "The use of OH * and CH * as heat release markers in combustion dynamics," *Spray Combust. Dyn.*, vol. 9, no. 4, pp. 409–423, 2017.

[100] P. Kasabov, N. Zarzalis, and P. Habisreuther, "Experimental study on lifted flames operated with liquid kerosene at elevated pressure and stabilized by outer recirculation," *Flow, Turbul. Combust.*, vol. 90, no. 3, pp. 605–619, 2013.

[101] T. Yi and D. A. Santavicca, "Combustion instability and flame structure of turbulent swirl-stabilized liquid-fueled combustion," *J. Propuls. Power*, vol. 28, no. 5, pp. 1000–1014, 2012.

[102] M. Stöhr, Z. Yin, and W. Meier, "Interaction between velocity fluctuations and equivalence ratio fluctuations during thermoacoustic oscillations in a partially premixed swirl combustor," *Proc. Combust. Inst.*, vol. 36, no. 3, pp. 3907–3915, 2017.

[103] I. Chterev *et al.*, "Simultaneous High Speed (5 kHz) Fuel-PLIE, OH-PLIF and Stereo PIV

Imaging of Pressurized Swirl-Stabilized Flames using Liquid Fuels," in *55th AIAA Aerospace Sciences Meeting*, 2017, no. January, pp. 1–17.

[104] D. J. Lockwood, "Rayleigh and Mie Scattering," in *Encylopedia of Color Science and Technology*, 2016, pp. 1097–1107.

[105] R. Yuan, J. Kariuki, and E. Mastorakos, "Measurements in swirling spray flames at blow-off," *Int. J. Spray Combust. Dyn.*, vol. 10, no. 3, pp. 185–210, 2018.

[106] A. P. Dowling and Y. Mahmoudi, "Combustion noise," *Proc. Combust. Inst.*, vol. 35, pp. 65–100, 2015.

[107] S. Gordon and B. J. McBride, *Computer Program for Calculation of Complex Chemical Equilibrium Compositions and Applications I. Analysis*. 1994, p. 58.

[108] S. Gordon and B. J. McBride, *Computer Program for Calculation of Complex Chemical Equilibrium Compositions and Applications: Part II - User Manual and Description*. 1996.

[109] G. Muthuselvan, M. Suryanarayana Rao, V. S. Iyengar, M. Pulumathi, S. Thirumalachari, and S. K, "Effect of Atomization Quality on Lean Blow-Out Limits and Acoustic Oscillations in a Swirl Stabilized Burner," *Combust. Sci. Technol.*, pp. 1–25, 2019.

[110] D. W. Hosmer, S. Lemeshow, and R. X. Sturdivant, *Applied Logistic Regression.*, 3rd ed. Wiley Publishing Co., 2013.

[111] J.-P. Frenillot, G. Cabot, M. Cazalens, B. Renou, and M. A. Boukhalfa, "Impact of H2 addition on flame stability and pollutant emissions for an atmospheric kerosene/air swirled flame," in *Proceedings of the European Combustion Meeting 2009*, 2009.

[112] J. S. Hardi, H. Camilo, G. Martinez, and M. Oschwald, "LOx Jet Atomization Under Transverse Acoustic Oscillations," *J. Propuls. Power*, vol. 30, no. 2, pp. 337–349, 2014.

[113] S. Gröning, J. S. Hardi, D. Suslov, and M. Oschwald, "Injector-Driven Combustion Instabilities in a Hydrogen / Oxygen Rocket Combustor," *J. Propuls. Power*, vol. 32, no. 3, pp. 560–573, 2016.

[114] J. E. Temme, P. M. Allison, and J. F. Driscoll, "Combustion instability of a lean premixed prevaporized gas turbine combustor studied using phase-averaged PIV," *Combust. Flame*, vol. 161, no. 4, pp. 958–970, 2014.

[115] K. M. Tacina, C. T. Chang, C. Lee, Z. He, and J. Herbon, "Effects of burning alternative fuel in a 5-cup combustor sector," in *9th U. S. National Combustion Meeting*, 2015, pp. 1–9.

[116] D. E. Cavaliere, J. Kariuki, and E. Mastorakos, "A comparison of the blow-off behaviour of swirl-stabilized premixed, non-premixed and spray flames," *Flow, Turbul. Combust.*, vol. 91, no. 2, pp. 347–372, 2013.

[117] K. M. Lyons, "Toward an understanding of the stabilization mechanisms of lifted turbulent jet flames : Experiments," *Prog. Energy Combust. Sci.*, vol. 33, pp. 211–231, 2007.

[118] W. Bachmann, "Hilbert-Transformation und Anwendung," in *Signalanalyse*, Vieweg+Teubner Verlag, 1992, pp. 122–134.

[119] Z. Zheng, T. Badawy, N. Henein, and E. Sattler, "Investigation of physical and chemical delay periods of different fuels in the ignition quality tester," *J. Eng. Gas Turbines Power*, vol. 135, no. 6, 2013.

[120] B. Sudarmanta and S. Winardi, "The Atomization And Combustion Characteristics of Biodiesel And Fossil Diesel Fuel Blend The Atomization And Combustion Characteristics of Biodiesel And Fossil Diesel Fuel Blend," in *Regional Conference of Chemical Engineering*, 2007.

[121] T. Lieuwen and B. T. Zinn, "A Mechanism of Combustion Instability in Lean Premixed Gas Turbine Combustors," *J. Eng. Gas Turbines Power*, vol. 123, pp. 182–189, 2001.

[122] J. O'Connor, S. Hemchandra, and T. C. Lieuwen, "Combustion Instabilities in Lean Premixed Systems," in *Lean Combustion*, 2nd ed., D. Dunn-Rankin and P. Therkelsen, Eds. Academic Press, 2016, pp. 231–259.

[123] T. C. Lieuwen, "Decomposition and Evolution of Disturbances," in *Unsteady Combustor Physics*, Cambridge University Press, 2012, pp. 17–49.

[124] J. P. Hathout, R. B. Corporation, P. Alto, J. Z. Company, A. M. Annaswamy, and A. F. Ghoniem, "Combustion Instability Active Control Using Periodic Fuel Injection," vol. 18, no. 2, 2002.

[125] X. Hui, K. Kumar, C. J. Sung, T. Edwards, and D. Gardner, "Experimental studies on the combustion characteristics of alternative jet fuels," *Fuel*, vol. 98, pp. 176–182, 2012.

[126] a M. Starik, "Gaseous and Particulate Emissions with Jet Engine Exhaust and Atmospheric

Pollution," *Adv. Propuls. Technol. High-Speed Aircraf*, vol. 150, no. 15, pp. 1–22, 2008.

[127] S. H. Won, D. Carpenter, S. Nates, and F. L. Dryer, "Derived cetane number as chemical potential indicator for nearlimit combustion behaviors in gas turbine applications," *Am. Soc. Mech. Eng. Power Div. POWER*, vol. 1, pp. 1–8, 2018.

[128] E. Ranzi *et al.*, "Hierarchical and comparative kinetic modeling of laminar fl ame speeds of hydrocarbon and oxygenated fuels," *Prog. Energy Combust. Sci.*, vol. 38, no. 4, pp. 468–501, 2012.

[129] S. Dooley *et al.*, "The experimental evaluation of a methodology for surrogate fuel formulation to emulate gas phase combustion kinetic phenomena," *Combust. Flame*, vol. 159, no. 4, pp. 1444–1466, 2012.

[130] C. Allen, D. Valco, E. Toulson, T. Edwards, and T. Lee, "Ignition behavior and surrogate modeling of JP-8 and of camelina and tallow hydrotreated renewable jet fuels at low temperatures," *Combust. Flame*, vol. 160, no. 2, pp. 232–239, 2013.

[131] S. Dooley *et al.*, "A jet fuel surrogate formulated by real fuel properties," *Combust. Flame*, vol. 157, no. 12, pp. 2333–2339, 2010.

[132] S. Burden, A. Tekawade, and M. A. Oehlschlaeger, "Ignition delay times for jet and diesel fuels: Constant volume spray and gas-phase shock tube measurements," *Fuel*, vol. 219, pp. 312–319, 2018.

[133] C. K. Westbrook, M. Mehl, W. J. Pitz, G. Kukkadapu, S. Wagnon, and K. Zhang, "Multi-fuel surrogate chemical kinetic mechanisms for real world applications," *Phys. Chem. Chem. Phys.*, vol. 20, no. 16, pp. 10588–10606, 2018.

[134] S. Dooley *et al.*, "The combustion kinetics of a synthetic paraffinic jet aviation fuel and a fundamentally formulated, experimentally validated surrogate fuel," *Combust. Flame*, vol. 159, no. 10, pp. 3014–3020, 2012.

[135] H. Wang and M. A. Oehlschlaeger, "Autoignition studies of conventional and Fischer-Tropsch jet fuels," *Fuel*, vol. 98, pp. 249–258, 2012.

[136] S. S. Vasu, D. F. Davidson, and R. K. Hanson, "Jet fuel ignition delay times: Shock tube

experiments over wide conditions and surrogate model predictions," *Combust. Flame*, vol. 152, pp. 125–143, 2008.

[137] C. Allen, E. Toulson, T. Edwards, and T. Lee, "Application of a novel charge preparation approach to testing the autoignition characteristics of JP-8 and camelina hydroprocessed renewable jet fuel in a rapid compression machine," *Combust. Flame*, vol. 159, pp. 2780–2788, 2012.

[138] S. Gowdagiri, W. Wang, and M. A. Oehlschlaeger, "A shock tube ignition delay study of conventional diesel fuel and hydroprocessed renewable diesel fuel from algal oil," *Fuel*, vol. 128, pp. 21–29, 2014.

[139] A. Vandersickel *et al.*, "The autoignition of practical fuels at HCCI conditions：High-pressure shock tube experiments and phenomenological modeling," *Fuel*, vol. 93, pp. 492–501, 2012.

[140] H. Wang and M. A. Oehlschlaeger, "Autoignition studies of conventional and Fischer-Tropsch jet fuels," *Fuel*, vol. 98, pp. 249–258, 2012.

[141] D. J. Valco, K. Min, A. Oldani, T. Edwards, and T. Lee, "Low temperature autoignition of conventional jet fuels and surrogate jet fuels with targeted properties in a rapid compression machine," *Proc. Combust. Inst.*, vol. 36, pp. 3687–3694, 2017.

[142] Y. J. Zhang, Z. H. Huang, J. H. Wang, and S. L. Xu, "Shock tube study on auto-ignition characteristics of kerosene/air mixtures," *Chinese Sci. Bull.*, vol. 56, no. 13, pp. 1399–1406, 2011.

[143] Y. Shigeta, K. Hayashi, M. Ichiyanagi, and K. Hishida, "Measurement of droplet size, velocity and spatial distribution of mass flux in spray by combining focus and defocus imaging technique," *Nihon Kikai Gakkai Ronbunshu, B Hen/Transactions Japan Soc. Mech. Eng. Part B*, vol. 78, no. 788, pp. 867–880, 2012.

Appendix A

By comparing the fuel properties in Table 1 with other literatures and considering that the bioderived fuel is tallow based, other parameters, such as the Derived Cetane Number (DCN) can be assumed. Hui et.al [125] researched on the ignition delay time as well as extinction stretch rate and laminar flame speed of several alternative jet fuels. HEFA fuel of this study and Hui's tallow HRJ fuel correlate very well in properties, therefore molecular weight, DCN and chemical equation are assumed to be the same, which are collected in Table A. 1. Additionally, synthetic fuel S-8, which is derived from natural gas by Fischer Tropsch process and R-8 are another hydroprocessed alternatives similar to this study's HEFA, because their basic material comes also from tallow and grease.

With the aid of the molar weight (MW) of carbon (MW_C = 12.0107 g/mol) and of hydrogen (MW_H = 1.00784) the H/C ratio of HEFA and Jet-A1 can be derived from the data of Table 1 with equation (A.1).

$$ {}^{H}/_{C}\, ratio = \frac{mass\%\ H * MW_C}{mass\%\ C * MW_H} \qquad (A.1) $$

Table A. 1: additional fuel properties

Properties	HEFA	Jet-A1	reference
H/C ratio [-]	2.14	1.91	calculated
MW [g/mol]	174	153.3	HEFA [125]; Jet-A1 [23]
DCN [-] (ASTM D7170)	65.85	49.35	HEFA [125]; Jet-A1 [44]
Molecular Formula	$C_{12.271}H_{26.412}$	$C_{11}H_{21}$	HEFA [125];Jet-A1 [126]
TSI	6.0	20.7	HEFA [127]; Jet-A1 [127]

Laminar flame speed

Hui et al. [125] also showed additionally experimental data for laminar flame speed of petroleum based and tallow based jet fuel at an ambient temperature of Tu = 400 K and concluded, that no significant difference exist between those two fuels. Zhang et al.[23] additionally states, that laminar flame speed is dictated by the flame temperature, which is dependent on heat of combustion. Both fuels show in Table 1 similar heat of combustion and therefore an appropriate reason for the similarities in laminar flame speed. The data from Hui are presented in Figure A. 1 with additional results from the well-known Ranzi kinetic mechanism [128] used on the surrogate, developed by Dooley et al. [129].

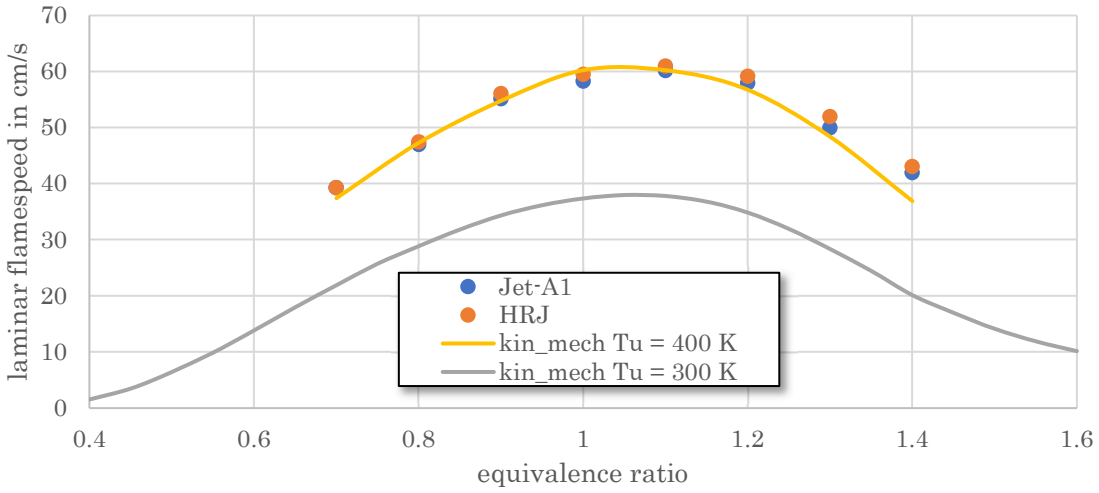

Figure A. 1: Laminar flame speed of Jet-A1 and HRJ fuel (data from [125]*, mechanism: Ranzi* [128]*, surrogate: Dooley* [129]*)*

Ignition delay time

After fuel is atomized and evaporated and mixed with air, an ignition source is necessary, to start the combustion. Jet engines have a permanent combustion, not like internal combustion engines with their four strokes, which means the ignition source is usually constantly available in the form of the recirculation zone or the heated volume from the flame or the flame itself. The ignitability of fuels or rather their ignition delay, which is the time from starting the ignition to the maximum of the heat release, is an immense research topic, since this delay is important for all transportation systems using combustion as power source. Therefore, fuels are tested in different systems, like ignition quality tester (IQT), shock-tube or rapid compression machine (RCM). Many researchers offer a wide range of publications regarding the ignition behavior of jet fuels and alternative jet fuels [130][129][131][132][133][134].

Allen showed, that between JP-8, which is a military jet fuel, almost completely equal to Jet-A1, which is used in this study, and tallow and camelina hydrotreated renewable jet fuel, which is similar to HEFA of this study, exists a wide difference in ignition delay time at intermediate to high pressure and at temperatures in a range of 625 to 730 K. Although the difference between the conventional and renewable jet fuels are remarkable, Allen's experiments focused only on low temperature region. In a jet engine combustor are typically temperatures way above 1000 K. Zhang et al. [23] collected data from Wang [135], Vasu [136] and Allen [137] and compared the "full" ignition delay curve over temperature as in Figure A. 2. Clearly visible are the differences in ignition delay time in the low temperature region as Allen [130] presented, but with an increase in temperature, this difference diminishes, until all fuels collect along one line in the high temperature region ($T > 1000$ K). Zhang and other researchers concluded that the high temperature chemistry is not affected by the different fuel composition.

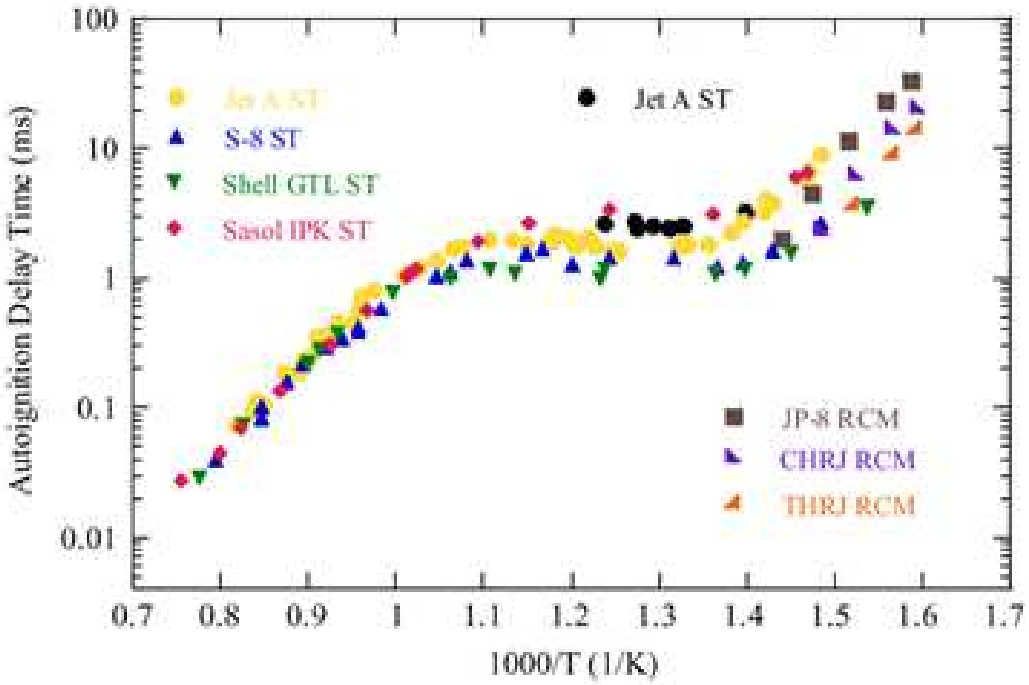

Figure A. 2: ignition delay time over a wide range of temperature (with permission from publisher for [23]*)*

In many publications, it was concluded, that the ignition delay time correlates very well with the derived cetane number (DCN). The DCN is a dimensionless number, also describing the ignitability of fuel-air mixtures. The difference to autoignition is, that DCN expresses the ignition of non-premixed combustion, from the time of injection of the fuel to the start of combustion. This means, the whole process includes fuel atomization and spraying, evaporation, mixing and ignition, so that DCN gives a direct measure for ignition propensity [23].

A low DCN number leads to a high ignition delay time and reciprocal. This often leads to the convenient conclusion, that ignition delay time is the responsible parameter, when comparing stability of different fuels.

To get an indication of the ignition delay time, which is one of the possible chemical timescale for lean blowout, Gowdagiri et al. [138] formulated a simple three-Arrhenius model for ignition delay time that includes DCN functionality. He used own data for petroleum-based jet fuel (F-76) and renewable hydroprocessed jet fuel (HRD-76) in addition to other researchers' data to verify his simple model. The

model showed same behavior as the real data, and most importantly for this research, no difference in ignition delay time in the high temperature region. The structure of the Arrhenius model consists of a combination of three timescales based on low, medium and high temperature range, represented by equation (A.2) and shown in Figure A. 3, which was derived by Vandersickel et al. [139]. The time constants of the three parts of the model can be expressed with Arrhenius temperature dependence and power-law functions for pressure, equivalence ratio and DCN dependence. The author concluded that the model is fit for DCN between 31 and 78.5, which corresponds well with Jet-A1 (49) and HEFA (65). Test data ranged between the temperatures 671 and 1266 K. Test pressure was between 10 and 20 atm, which still gave a very good fit for 8 atm in their publication. Therefore, it is used for the assumptions of this study.

$$\frac{1}{\tau} = \frac{1}{\tau_L + \tau_M} + \frac{1}{\tau_H} \qquad (A.2)$$

With L,M and H as low, middle and high temperature range, respectively.

$$\tau_i = A_i \left(\frac{P}{P_{ref}}\right)^{\alpha_i} \varphi^{\beta_i} \left(\frac{DCN}{DCN_{ref}}\right)^{\gamma_i} exp\left(\frac{T_{act,i}}{T}\right) \text{ for i = L,M,H} \qquad (A.3)$$

For reference pressure and reference DCN, 1 atm and 50 were chosen, respectively. The other parameters are best fit choices by Gowdagiri et al. [138].

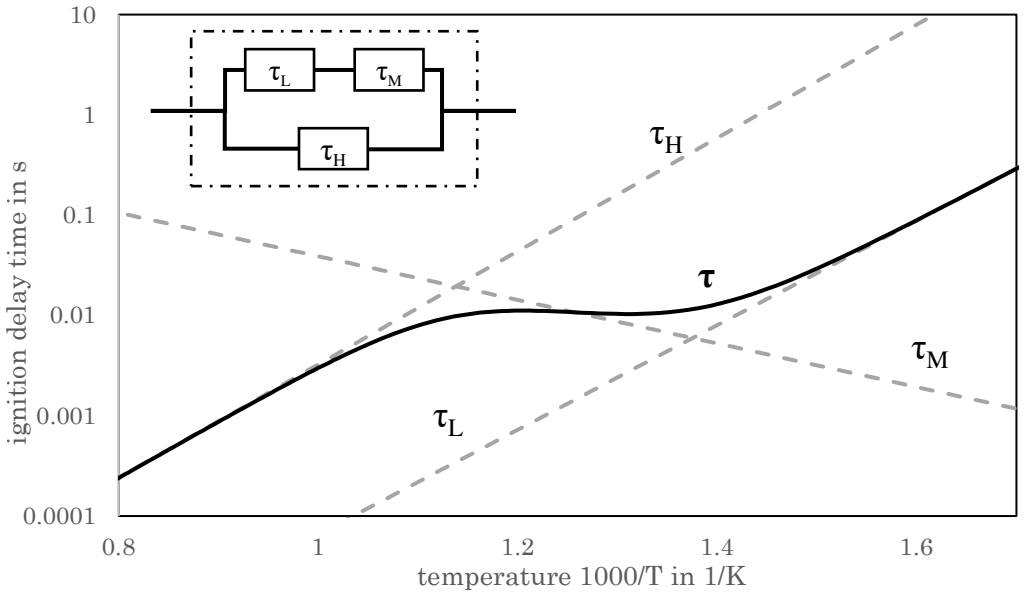

Figure A. 3: Three Arrhenius model for ignition delay time (based on [139]*)*

Using the data from Table 1, simple models for the ignition delay time for HEFA and Jet-A1 of this study can be derived and compared in Figure A. 4. Clearly shown is the dependency of ignition delay time over temperature. As mentioned above, the graph shows ignition delay time difference in the low

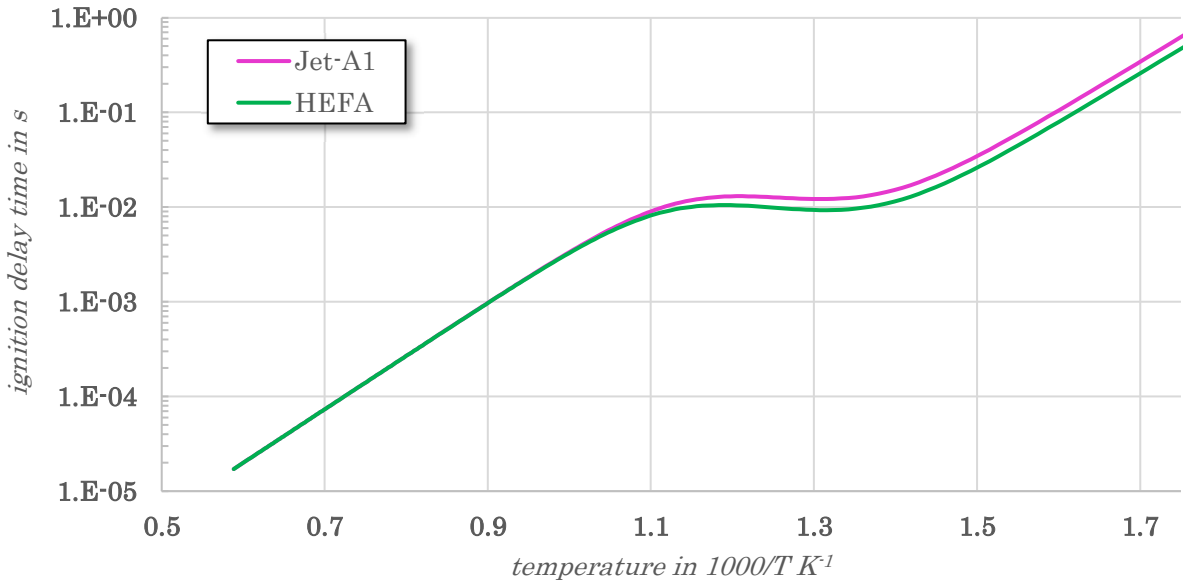

Figure A. 4: ignition delay time according to Three-Arrhenius model for Jet-A1 and HEFA for 0.5 MPa and φ = 1.0

temperature region, but above 1000 K, the difference of both fuels diminishes, and the two graphs align. This indicates neglectable difference in ignition delay time at temperatures typical inside the combustion chamber of jet engines. Additionally, Figure A. 5 shows the ignition delay time dependency over different equivalence ratios. An increase in equivalence ratio shows a reduction of ignition delay time, though in a narrow range. A zero-dimension simulation with Cantera showed similar values for ignition delay time of a Jet-A1 surrogate (this is not included in this study anymore).

In Figure A. 2, it was shown, that the ignition delay time of different jet fuels of mentioned publications gather together when reaching high temperature region (T>1000 K), therefore it can be assumed, that there is no difference between Jet-A1 and HEFA. The Arrhenius model shows an increase in ignition delay time with an decrease in equivalence ratio, as described and researched by several publications [140][130][141]. Although, it is only a model, other researchers showed experimental data, proofing that behavior, like Zhang et al. [142].

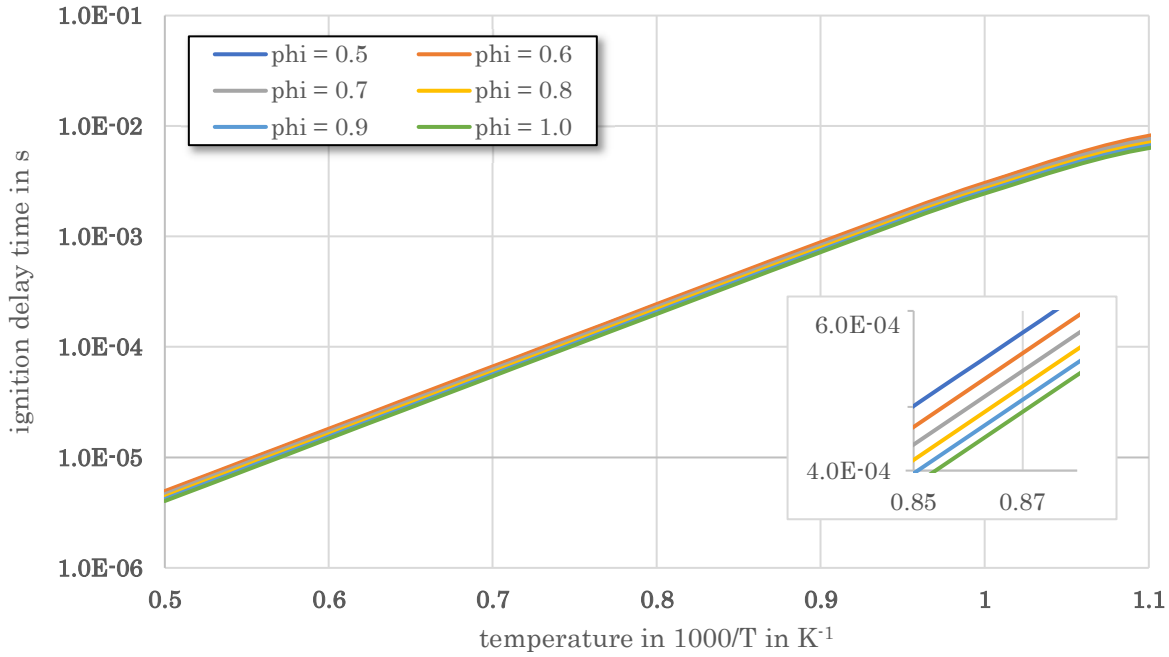

Figure A. 5: change in ignition delay time over equivalence ratio (pressure: 0.5 MPa)